

Dynamic Substructuring for Efficient Vibrational Studies in Buildings



Valentijn S. van den Bosch

MSc. Thesis

Dynamic Substructuring for Efficient Vibrational Studies in Buildings

by

VALENTIJN SAMUËL VAN DEN BOSCH

For the degree of Master of Science in Civil Engineering
at Delft University of Technology

To be defended in public on February 13th, 2019

Student number: 4008146
Thesis committee: Prof. dr. A. V. Metrikine, Structural Mechanics
Dr. ir. K.N. van Dalen, Structural Mechanics
Dr. ir. D. de Klerk, Precision & Microsystems Engineering
Dr. ir. M.V. van der Seijs, VIBES.technology
Ir. M.J.G. Hermens, Royal Haskoning DHV

Faculty of Civil Engineering and Geosciences • Delft University of Technology



Copyright © 2019 by Valentijn S. van den Bosch
All rights reserved.

Abstract

As a reaction to urban densification, light weight building is an attractive concept for optimally utilizing the capacity of the existing built environment. A common issue paired with light weight construction is the need to engage in vibrational design, in order to minimize hindrance due to human activities such as walking, that cause vibrations in buildings. The Finite Element Method (FEM) is a crucial tool for accurately predicting structural behaviour in such a context. The typical problem with FEM considering large, complex or detailed structures, is that analyses may demand intolerably large computational effort to perform design studies.

As a solution, a component-wise approach called Component Mode Synthesis (CMS) is proposed. CMS technique involves separating a construction into substructures, after which Model Order Reduction (MOR) is performed on each substructure individually. With this, the substructures are efficiently described by a limited amount of Degrees of Freedom (DoF), after which they are assembled by means of Dynamic Substructuring (DS) techniques. Considering the large amounts of substructure DoF to be coupled to other assembly parts (typically containing 1%-10% of the total amount), an additional measure is required for analyses to be viable: a reliable interface reduction should be performed to deal with the number of unreduced interface DoF that still exist.

This research investigates interface reduction by means of Orthogonal Polynomial Series, creating an a priori determined, generic reduction basis which closely resembles the true vibration modes along substructure interfaces. Its performance is investigated with several conceptual case studies, conducting reduced order analysis in Matlab and comparing the results with a full order solution. Alterations are explored, including different polynomial bases (Legendre and Fourier), flexible couplings and viscoelasticity at either coupled substructure boundaries or bodies.

The relevance of complex modes in viscoelastic structures with lightly varying damping and stiffness is examined, as well as accuracy of approximations of complex modes, with the prospect of enabling arbitrary frequency dependent material properties to be represented in an efficient manner. This involves approximation of complex modes, obtained by superposition of undamped modes, for which a strategy is developed to optimize considered inclusion of undamped modes.

Ultimately, a representative building is modelled in order to relate test results of OPS interface reduction to an applicable context, and to prove the overall effectiveness of the enhanced CMS strategy for large light weight building models.

OPS interface reduction using Legendre series has shown to be a reliable and efficient technique depending on the frequency range considered. Its general error trends are mostly insignificant or manageable and flexible/viscoelastic boundary couplings do not deflate this. Disproportional viscoelasticity in substructure bodies, with respect to their mass and stiffness matrices, are not necessarily benefited by the use of complex vibration modes when its dynamic modulus varies lightly over frequency. Though the potential which is beyond this scope, yet remains undetermined, the presented approximation technique for complex modes also comes with additional limitations besides the amount of damping. With regards to the applicative value of CMS, the analyses of the light weight building model prove that OPS interface reduction enables significant improvement of computational efficiency, yet yielding accurate results, as a valuable solution for modern-day problems.

Preface

For some reason, during the course of my studies, I had always feared the final part of becoming an engineer: writing a Master thesis. Whenever I expressed my anxiety about commencing my research, people often reacted surprised. As they said, a thesis would be a great opportunity to continue in what I like most, one where all I had priorly studied for becomes real, one where I really find out what kind of engineer I would become. And they were right, but so was my gut feeling. It had been a tough climb indeed, but would it have taught me the same if it weren't? Thesis research made me passionate about dynamics, the endless possibilities in how to approach engineering problems and getting to understand a part of science in fine detail. It helped me explore my capabilities and pitfalls, both professionally and personally, for which I am thankful.

First of all, I would like to thank Maarten van der Seijs who has provided me of weekly supervision during this research, through VIBES.technology. Maarten always gave me exactly the pointers I needed, so that I could explore the world of Dynamic Substructuring by myself, but knowing where to look. Also I really appreciated his critical, yet motivational way of mentoring. Next, I would to thank Maurice Hermens for hosting the occasional visits at the Royal Haskoning DHV office and thinking along from the practical point of view. Once we were meeting, I felt like we could brainstorm endlessly on the topic. Also, would I like to thank Karel van Dalen and Andrei Metrikine for keeping me sharp and providing with useful feedback during our meetings. Though Dennis de Klerk had only joined the team in the last stage of this research, he often managed to grant me great motivational boosts whenever he was around. I am grateful for his enthusiasm and his willingness to get involved. Furthermore, I would like to thank the VIBES.technology team for their open and supportive attitude, granting me a pleasant work environment during the many Fridays.

Besides professional assistance, I have also received a lot of personal comforting which definitely lightened the burden. I am thankful to my family for their supportive attitude. Especially my mother Joyce has meant a lot to me. Often concerned about my well-being, she would do anything within her powers to get me through. Finally, I would like to express my gratitude towards my friends who reminded me that life can still be good throughout, my fellow students for enabling me to laugh about the tough fate we shared.

Valentijn van den Bosch
February 2019

Contents

1	Introduction	1
1.1	Research context	1
1.2	Research goals	2
1.3	Research outline	4
1.4	Author’s contributions	5
I	Theory	7
2	Substructure coupling	9
2.1	Interface conditions	10
2.2	Assembly	11
2.2.1	Primal assembly	12
2.2.2	Dual assembly	12
2.3	Substructuring on a reduced basis	12
2.4	Non-conforming interfaces	13
2.5	Additional interface physics	14
2.5.1	Stiffness and damping	14
2.5.2	Inertia	15
3	Component Mode Synthesis	17
3.1	Vibration modes	17
3.1.1	Free interface modes	18
3.1.2	Fixed interface modes	18
3.1.3	Rigid body modes	18
3.2	Static modes	18
3.2.1	Constraint modes	18
3.2.2	Attachment modes	19
3.2.3	Residual attachment modes	20
3.3	Fixed interface methods	20
3.3.1	Guyan method	21
3.3.2	Craig-Bampton method	21
3.4	Free interface methods	21
3.4.1	MacNeal’s method	21
3.4.2	Rubin’s method	22
4	Interface reduction	23
4.1	Interface rigidification	23
4.2	Modal interface reduction	24
4.3	Wave-Based Substructuring	24

4.4	Orthogonal Polynomial Series	25
4.4.1	Legendre polynomials	25
4.4.2	Fourier series	26
5	Damping and viscoelasticity in Component Mode Synthesis	29
5.1	Proportional damping	29
5.2	Frequency dependent damping	30
5.2.1	Kelvin-Voigt model	31
5.2.2	Maxwell model	32
5.2.3	Standard Linear Solid model	32
5.2.4	Generalized Maxwell model	33
5.2.5	Advanced models	33
5.3	Complex eigenmodes	34
5.3.1	The polynomial eigenvalue problem	34
5.3.2	Rayleigh's approximative method	34
5.3.3	Reduction of Rayleigh's method	36
5.4	Application in CMS	39
5.4.1	Modified Craig-Bampton method	39
5.4.2	Ding's method	39
6	Error evaluation	41
II	Verification	43
7	Testing procedure	45
7.1	Finite Element Modelling	46
7.2	Component reduction	46
7.3	Assembly	49
7.4	Spectral analysis	50
7.5	Post-processing and comparison	50
8	Principal test cases and results	51
8.1	Undamped, rigidly connected plates	52
8.1.1	Results	53
8.2	Proportionally damped, rigidly connected plates	55
8.2.1	Results	55
8.3	Proportionally damped, flexibly connected plates	57
8.3.1	Results	59
8.4	Proportionally damped, viscoelastically connected plates	61
8.4.1	Results	63
8.5	Proportionally viscoelastic, rigidly connected plates	63
8.5.1	Results	64
8.6	Disproportional viscoelastic, rigidly connected plates	64
8.6.1	Results	65
9	Building case and results	69
9.1	Model design	69
9.2	Results	72
9.2.1	Load to interfaces, frequency response	73
9.2.2	Load to points of interest, frequency response	75
9.2.3	Load to points of interest, time history response	77

10 Conclusions and recommendations	81
10.1 Conclusions	81
10.2 Recommendations	83

Nomenclature

Greek symbols

β	Reliability index	ϕ	Vibration mode shape
δ	Boundary damping matrix	Ψ	Set of static deformation shapes
η	Modal coordinates	ψ	Static deformation shape
κ	Boundary stiffness matrix	ω	Circular frequency
λ	Lagrange multipliers	σ	Stress or standard deviation
μ	Boundary mass matrix	ε	Strain
Φ	Set of vibration mode shapes	ξ	Viscosity

Roman symbols

A	Boundary localization matrix	p	Generalized force / moments
B	Signed Boolean matrix	q	Generalized coordinates
C	Damping matrix	R	Reduction matrix
f	External forces / moments	u	Displacements
G_r	Residual flexibility matrix	Y	Dynamic flexibility matrix
G	Kernel function matrix	Z	Dynamic stiffness matrix
g	Interface forces / moments	E	Elastic modulus
I	Identity matrix	G	Kernel function
K	Stiffness matrix	s	Laplace variable
L	Boolean localization matrix	t	Time
M	Mass matrix		

Sub- and superscripts

\star^*	Complex conjugate of \star	\star^+	Pseudo-inverse of \star
-----------	------------------------------	-----------	---------------------------

\star_γ	Pertaining to interface DoF	\star_i	Pertaining to interior DoF
\star_b	Pertaining to boundary DoF	\star_{ret}	Pertaining to retained modes/eigenfrequencies
\star_c	Pertaining to constraint DoF		

Abbreviations

CB	Craig-Bampton	MAE	Mean Absolute Error
CMS	Component Mode Synthesis	MCB	Modified Craig-Bampton
DoF	Degree(s) of Freedom	MCK	Mass- Damping- Stiffness-
DS	Dynamic Substructuring	MNAE	Mean Normalized Absolute Error
EPDM	Ethylene Propylene Diene Monomer	MNRE	Mean Normalized Relative Error
FEM	Finite Element Method	MOR	Model Order Reduction
FFT	Fast Fourier Transform	MRE	Mean Relative Error
FRAC	Frequency Response Assurance Criterion	NCAW	Normalized Central Accumulated Weight
FRF	Frequency Response Function(s)	OPS	Orthogonal Polynomial Series
IF	Interface	RMSE	Root Mean Square Error
IFFT	Inverse Fast Fourier Transform	SLS	Standard Linear Solid
MAC	Modal Assurance Criterion	WBS	Wave-Based Substructuring

Chapter 1

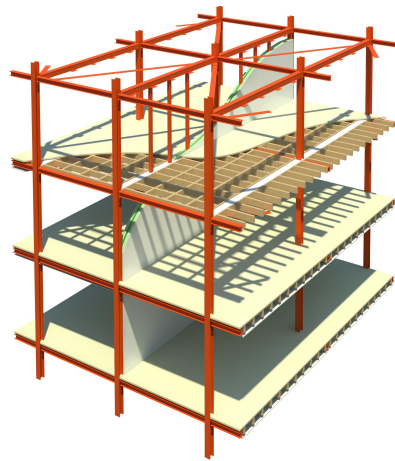
Introduction

1.1 Research context

As society modernizes, new design trends emerge within the built environment. Architects and engineers are eager to extend the limits of technique, in many cases leading to expressive and complex designs. Though such developments are sometimes associated with competition of corporate status, the evolution of building technique often arises as an answer to societal needs. As environmental awareness is growing, sustainability becomes an increasingly valued theme in many industries, including construction. The surging demand for housing in urban areas necessitates high-rise solutions in order to extend the housing capacity. While demolition of functioning existing structures may seem an obvious, but unsustainable measure, Royal Haskoning DHV proposes a strategy to expand the urban capacity, without compromising its existing state: a lightweight building concept is employed to enable construction onto and through existing buildings (see figure 1.1), optimizing utilization of their structural capacities [1]. This comes with an additional problem: usually lightweight buildings are significantly more sensitive for most vibrations they are exposed to, compared to traditional buildings. This may cause discomfort for its users, often up to an unacceptable level. This is not a problem that is treated with a one-fits-all solution and requires conceptual analyses to qualitatively investigate effectiveness of proposed measures. [2].



(a) A modular lightweight building



(b) Modular structural lay-out

Figure 1.1: Renders of the Karel Doorman Rotterdam (by Royal Haskoning DHV)

The Finite Element Method (FEM) is an indispensable tool for such structural analysis. This method assembles structures through many simpler, mechanically comprehensible elements. It competently offers approximative solutions for structures too complex for engineers to obtain analytically. With the increasing size and complexity, two problems arise. Though FEM enables engineers to efficiently outsource a large portion of their work to computers, models are reaching sizes up to the point that computational time becomes a bottleneck for economically justified engineering.

This thesis proposes to engage in studies like this by means of Dynamic Substructuring (DS), a useful tool in analysis of structural dynamics, both in the experimental as the numerical field [3]. DS covers an approach enabling one to analyse structures component-wise, offering possibilities to focus on problems locally. Currently, DS application is mostly seen in industries for spacecraft, wind turbines [4, 5] or automotive [6, 7, 8, 9]. Though DS is definitely applicable in civil engineering, occurrences of its use are limited. A specific type of DS that is attractive to deal with large models is Component Mode Synthesis (CMS). CMS is a technique where modal analysis is performed separately at the structural components, or substructures, retaining only a limited amount of modes as means of Model Order Reduction (MOR). Afterwards DS technique is used to assemble the components into e.g. a complete building. This technique is especially efficient if an assembly exists of repeated components, i.e. modules, as their reduced order properties only need to be obtained once. The effectiveness of the MOR itself though, depends in the first place on interior reduction, the technique used for dealing with DoF that remain uncoupled to other components. Many classical methods are still reliantly used [10, 11], as well as many advanced methods are recently being developed using hybrid approaches [12, 13], iterative improvements [14], addressing viscoelasticity [15, 16, 17] or non-linear problems [18, 19]. Secondly, when dealing with large amounts of Degrees of Freedom (DoF) at interfaces connecting components, interface reduction is of great relevance for gaining computational efficiency. Though also in this area many techniques are being developed, addressing rigidification [20], Interface Displacement Modes (see section 4.2) [21, 22, 23] and various other principles [24, 25], their applicabilities or effectiveness are limited.

This research attempts to develop an effective a interface reduction method in order to make CMS an attractive tool in vibrational analysis of buildings and many other fields. In buildings, many connections between modules can be regarded as being line- or surface shaped, and can often not be simplified to a point. This implies that reduction of building models has relatively low benefit, unless interfaces are effectively reduced. The interface reduction method proposed in this thesis, is referred to as Orthogonal Polynomial Series (OPS) reduction. This method exploits the resemblance of an a priori chosen set of basis functions with typical interface mode shapes. Only a limited set of these basis functions is sufficient to cover the majority of ongoing interface dynamics, thus reducing the number of DoF required to do so. A first suggestions of using basis functions is done in [24], and during this research also its practical potential has been explored in [26].

Considering the role of connections between structural parts in the dynamics of an assembly [27], practical feasibility of viscoelastic modelling is investigated as well in this research, supported by existing methods [15, 16]. This involves the use of complex vibration modes, which are obtainable exactly for some viscoelastic models, but are bound to approximations for more specifically formulated models [28, 29, 30, 31]. Also, as FEM models are increasingly reduced, the share of eigenvalue analysis (used to establish reduction bases) to the remaining computational time increases, whereas approximative methods also offer opportunity to further computational efficiency, provided that sufficient accuracy is secured.

1.2 Research goals

As becomes clear in section 1.1, vibrational studies in buildings could be benefited, among other by CMS due to its ability to treat design flaws with a local approach, rather than unnecessarily involving the full modelled environment in all analysis steps. To enable such analyses to be performed efficiently, yet accurately, it is essential for a reliable interface reduction method to be available. Also, when dealing with uncommon circumstances such as viscoelasticity, their effects should be studied and treated if necessary. Thus for adding value, both from a

conceptual as a practical perspective, this research focuses on the following three aspects:

- 1 Development of a reliable interface reduction method
- 2 Assessment of the potential effects of viscoelasticity in CMS and the ability to cope with them
- 3 Creation and evaluation of practical value of CMS for buildings

Reliable interface reduction

When considering development of a reliable interface method, a solution is sought in the suggestion in [24] to use a priori chosen basis functions, or in this case more specifically: orthogonal polynomial series which are further elaborated in section 4.4. Though a reliable method could be a wide term, but is narrowed down to the following aspects:

- 1.1 Qualitative and quantitative coverage of dynamic behaviour
- 1.2 Convergence of results with expansion of the reduction basis
- 1.3 Tracing of error trends and assessing of their relevance and potential solutions
- 1.4 Comprising the above aspects with a reasonably small reduction basis

As will become clear later in this thesis, the aforementioned aspects are indistinct without a context. Therefore a simple conceptual case is used to obtain indicative results.

Effects of viscoelasticity

Anticipating on design measures using materials such as rubbers, or construction joints providing additional damping, in order to control structural vibrations, it is desirable to include their effects as accurately as possible in CMS analysis. For this reason their effects on CMS are assessed within realistic bounds, pursuing the following:

- 2.1 Viscoelastic effects within substructures and between their boundaries
- 2.2 Relevance and effects of adapted CMS technique (using complex vibration modes)
- 2.3 Reliability, efficiency and accuracy of complex vibration mode approximation

Included are basic viscoelastic models represented by parallel spring/dampers, but also a more extensive description using a Generalized Maxwell model (see section 5.2.4), representing EPDM rubber behaviour. The latter is bound to approximations when utilizing complex modes. Either the viscoelastic properties are fitted to a workable function description, or solving the corresponding eigenproblem is performed by approximation. As the latter offers opportunity to reduce the computational time in this analysis part as well, its viability is explored.

Practical value of CMS

Naturally, given the practical context priorly suggested, the relevance of this research would be invigorated with proof under realistic conditions. Application for vibrations in lightweight buildings due to human footsteps is therefore investigated. Results are evaluated, provided aforementioned context, aiming for the following:

- 3.1 Qualitative and quantitative coverage of dynamic behaviour at substructure interfaces
- 3.2 Qualitative and quantitative coverage of dynamic behaviour at points of interest
- 3.3 Accuracy of physical responses due to realistic loading
- 3.4 Comprising the above aspects gaining a significant increase of computational efficiency

A generic lightweight building is modelled and analysed using FEM. Error trends are compared to observations in the conceptual test case. Tendencies are brought into relation with design variations in order to determine universal validity.

1.3 Research outline

The remainder of this thesis consists of two parts, the first part addressing most theory used, beyond a set level of prior knowledge regarding dynamics, FEM and applied mathematics. Also, the essential theory is accompanied with some extent of broadening concepts, as to illustrate the current state-of-art within the field.

The second part presents the validation process with respect to described research goals. A systematic approach is visualised, as well as the test cases involved. Their results are presented and discussed, ultimately leading to conclusions and recommendations.

More specifically, the parts are divided into chapters, each addressing the following topics:

Part I: Theory:

- **Chapter 2** introduces the main concept of Dynamic Substructuring, along with some relevant specifics. This chapter is mainly based on [6] and [4].
- **Chapter 3** describes the basic concept of Component Mode Synthesis, together with some widely used classical (interior) reduction methods and their 'ingredients'. This chapter is mainly based on [4] and [5].
- **Chapter 4** provides various interface reduction methods, including Orthogonal Polynomial Series reduction, elucidating common advantages and disadvantages of certain concepts.
- **Chapter 5** focusses on viscoelasticity, elaborating on various applied rheological models and their frequency dependent properties. Also two CMS techniques which are designed for viscoelasticity are described, providing two methods of obtaining complex eigenmodes (required for the CMS techniques).
- **Chapter 6** describes some general error and error indicating definitions, together with unaccustomed definitions which are suitable in this research.

Part II: Validation:

- **Chapter 7** features a gathering of the theoretical concept of part I, which is cast into procedural guidelines for practical use, illustrated by block schemes. As these procedures match the approach of this research, it also serves to provide transparency in the steps taken.
- **Chapter 8** presents the conceptual case and its variants, used for principle validation. These cases feature several substructure connection types, being rigid, flexible and viscoelastic. Also viscoelasticity within substructure bodies is treated.
- **Chapter 9** presents a generic practical case of a modular designed building, providing realistic conditions for relevant application. Results are presented and discussed in a similar fashion as in chapter 9, though verging towards practical interests.
- **Chapter 10** reflects on the research goals and uses the findings of chapter 8 and 9 to reach conclusions, after which recommendations for possible succeeding research are done.

1.4 Author's contributions

The following developments in the field of CMS are proposed as means of extending its current state of knowledge:

- Demonstration of implementation and robustness of OPS interface reduction under various circumstances of substructure coupling. Chapter 8
- An algorithm for optimizing efficiency of complex mode approximation through superposition of undamped normal modes for a set limit of accuracy loss. Section 5.3.3
- Additional physical bounds for reliability of complex mode approximation through superposition of undamped normal modes. Section 8.6
- Proof of practical feasibility and benefits of OPS interface reduction for vibrational analysis in light weight buildings. Chapter 9

Part I
Theory

Chapter 2

Substructure coupling

Dynamic Substructuring is a technique that approaches dynamical analysis of mechanical systems component-wise, as to determine behaviour of an assembled system by means of coupling of these components, also called substructures. This may involve experimental models and numerical models, or even a combination of both. Local problems are identified more easily and meanwhile the divided analysis allows for reducing the computational load of large models. Also components can be interchanged, such that design changes only require reanalysis of the substructure in concern.

This chapter hosts the necessary theoretical tools for coupling these substructures, in order to find their dynamic behaviour as an assembly. To do so, a discretized mechanical model of each substructure is required, may it be obtained from FEM or experiments. Once the dynamic behaviour of separate substructures is determined, either in a full or reduced domain (elaborated in chapter 3), their interactive behaviour can be found by means of the coupling procedure. This chapter first treats substructure coupling in the simplest formulation in a full frequency domain following [6]. Afterwards, the theory is generalized such that reduction bases can be included. Also cases where interfaces are non-conforming or are prone to additional physics are described.

Figure 2.1 illustrates a general example of two substructures to be coupled. Since the coupling procedure mainly involves operations with respect to interface DoF, a distinction is made between interior DoF $\mathbf{u}_i^{(s)}$ and boundary DoF $\mathbf{u}_b^{(s)}$. Preparing for the coupling, coordinates \mathbf{u} , interface forces \mathbf{g} and external forces \mathbf{f} of both substructures are concatenated into global vectors:

$$\mathbf{u} \triangleq \begin{bmatrix} \mathbf{u}_i^A \\ \mathbf{u}_b^A \\ \mathbf{u}_i^B \\ \mathbf{u}_b^B \end{bmatrix}; \quad \mathbf{g} \triangleq \begin{bmatrix} \mathbf{0} \\ \mathbf{g}_b^A \\ \mathbf{0} \\ \mathbf{g}_b^B \end{bmatrix}; \quad \mathbf{f} \triangleq \begin{bmatrix} \mathbf{f}_i^A \\ \mathbf{f}_b^A \\ \mathbf{f}_i^B \\ \mathbf{f}_b^B \end{bmatrix}; \quad (2.1)$$

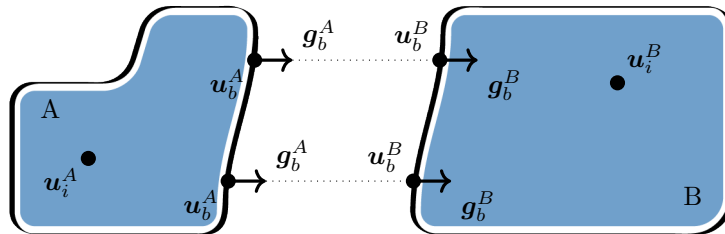


Figure 2.1: Two substructures A and B, to be coupled at their common boundaries

2.1 Interface conditions

The key to successful coupling is to define and enforce interface conditions correctly. There are two types of interface conditions: kinematic and dynamic conditions. Assuming substructures A and B to be rigidly connected, compatibility is described by:

$$\mathbf{u}_b^A - \mathbf{u}_b^B = \mathbf{0} \quad (2.2)$$

or:

$$\mathbf{B}\mathbf{u} = \mathbf{0} \text{ with } \mathbf{B} \triangleq [\mathbf{0} \quad -\mathbf{I} \quad \mathbf{0} \quad \mathbf{I}] \quad (2.3)$$

\mathbf{B} is referred to as the signed Boolean matrix and contains as many rows as there are matching pairs of DoF. Note that eq 2.3 assumes the interface displacement vectors to be in matching order.

Knowing that a matching pair of DoF essentially leads to multiple DoF containing the same information, the displacement field can either be expressed with this redundant information (dually), or be generalized into to a one set of actual independent DoF (primally). When considering the displacement field in a primal sense, the dually formulated displacement field \mathbf{u} as in equation 2.1 can be defined through generalized coordinates \mathbf{q} and the corresponding Boolean localisation matrix \mathbf{L} :

$$\mathbf{u} = \mathbf{L}\mathbf{q} \text{ such that } \begin{cases} \mathbf{u}_i^A = \mathbf{q}_1 \\ \mathbf{u}_b^A = \mathbf{q}_2 \\ \mathbf{u}_i^B = \mathbf{q}_3 \\ \mathbf{u}_b^B = \mathbf{q}_2 \end{cases} \text{ and } \mathbf{L} \triangleq \begin{bmatrix} \mathbf{I} & \mathbf{0} & \mathbf{0} \\ \mathbf{0} & \mathbf{0} & \mathbf{I} \\ \mathbf{0} & \mathbf{I} & \mathbf{0} \\ \mathbf{0} & \mathbf{0} & \mathbf{I} \end{bmatrix} \quad (2.4)$$

Matrix \mathbf{L} will prove itself useful in the primal assembly (section 2.2.1) and can either be described directly or through computation. As equation 2.4 describes solely unique DoF, it holds for any vector \mathbf{q} , such that substitution into equation 2.3 proves \mathbf{L} to be the nullspace of \mathbf{B} :

$$\mathbf{B}\mathbf{L}\mathbf{q} = \mathbf{0} \quad \forall \mathbf{q} \Rightarrow \mathbf{L} = \text{null}(\mathbf{B}) \quad (2.5)$$

Similarly, \mathbf{B} can be found through \mathbf{L} :

$$\mathbf{B}^T = \text{null}(\mathbf{L}^T) \quad (2.6)$$

Now that kinematic conditions are stated, the dynamic conditions remain. In the most common case, the mass of the interface is assumed to be 0 (not to be confused with modelled mass accumulated at an interface). Due to this, simple force equilibrium holds between both sides of the interface:

$$\mathbf{g}_b^A + \mathbf{g}_b^B = \mathbf{0} \text{ or } \begin{cases} \mathbf{g}_b^A = \boldsymbol{\lambda} \\ \mathbf{g}_b^B = -\boldsymbol{\lambda} \end{cases} \quad (2.7)$$

In the second notation $\boldsymbol{\lambda}$ is the set of Lagrange multipliers that represents the intensity of the interface forces. Describing the force equilibrium condition over the whole system, again \mathbf{B} and \mathbf{L} can be used:

$$\mathbf{L}^T \mathbf{g} = \mathbf{0} \text{ or } \mathbf{g} = -\mathbf{B}^T \boldsymbol{\lambda} \quad (2.8)$$

Dirichlet boundary conditions

Besides interface conditions, one can also process Dirichlet boundary conditions in the same manner. Considering the set of DoF which are to be constrained, \mathbf{u}_c :

$$\mathbf{u}_c = \mathbf{0} \quad (2.9)$$

thus:

$$\mathbf{B}_c \mathbf{u}_c = \mathbf{0} \text{ for } \mathbf{B}_c = \mathbf{I} \quad (2.10)$$

To prepare for assembly, a further distinction is made between constraint DoF and the priorly partitioned interior- and boundary DoF, redefining \mathbf{u} , \mathbf{g} and \mathbf{f} :

$$\mathbf{u} \triangleq \begin{bmatrix} \mathbf{u}_i^A \\ \mathbf{u}_b^A \\ \mathbf{u}_c^A \\ \mathbf{u}_i^B \\ \mathbf{u}_b^B \\ \mathbf{u}_c^B \end{bmatrix}; \quad \mathbf{g} \triangleq \begin{bmatrix} \mathbf{0} \\ \mathbf{g}_b^A \\ \mathbf{g}_c^A \\ \mathbf{0} \\ \mathbf{g}_b^B \\ \mathbf{g}_c^B \end{bmatrix}; \quad \mathbf{f} \triangleq \begin{bmatrix} \mathbf{f}_i^A \\ \mathbf{f}_b^A \\ \mathbf{f}_c^A \\ \mathbf{f}_i^B \\ \mathbf{f}_b^B \\ \mathbf{f}_c^B \end{bmatrix}; \quad (2.11)$$

In order to retain validity of equation 2.3, equation 2.10 is recast to global coordinates and added, such that \mathbf{B} is redefined as:

$$\mathbf{B} \triangleq \begin{bmatrix} \mathbf{0} & -\mathbf{I} & \mathbf{0} & \mathbf{0} & \mathbf{I} & \mathbf{0} \\ \mathbf{0} & \mathbf{0} & \mathbf{I} & \mathbf{0} & \mathbf{0} & \mathbf{0} \\ \mathbf{0} & \mathbf{0} & \mathbf{0} & \mathbf{0} & \mathbf{0} & \mathbf{I} \end{bmatrix} \quad (2.12)$$

Augmenting equation 2.9 to 2.4, matrix \mathbf{L} is also redefined:

$$\mathbf{L} \triangleq \begin{bmatrix} \mathbf{I} & \mathbf{0} & \mathbf{0} \\ \mathbf{0} & \mathbf{0} & \mathbf{I} \\ \mathbf{0} & \mathbf{0} & \mathbf{0} \\ \mathbf{0} & \mathbf{I} & \mathbf{0} \\ \mathbf{0} & \mathbf{0} & \mathbf{I} \\ \mathbf{0} & \mathbf{0} & \mathbf{0} \end{bmatrix} \quad (2.13)$$

Apart from partitioning of the dynamic stiffness/flexibility matrix, assembly does not demand further specific adjustments. Therefore, from here on, descriptions assume substructure coupling without Dirichlet boundary condition enforcement.

2.2 Assembly

The next step is to prepare the equations of motion, such that the interface conditions can be enforced. One can either use the dynamic stiffness \mathbf{Z} or dynamic flexibility description \mathbf{Y} , depending on the type of assembly to be applied:

$$\mathbf{Z} \triangleq \begin{bmatrix} \mathbf{Z}_{ii}^A & \mathbf{Z}_{ib}^A & \mathbf{0} & \mathbf{0} \\ \mathbf{Z}_{bi}^A & \mathbf{Z}_{bb}^A & \mathbf{0} & \mathbf{0} \\ \mathbf{0} & \mathbf{0} & \mathbf{Z}_{ii}^B & \mathbf{Z}_{ib}^B \\ \mathbf{0} & \mathbf{0} & \mathbf{Z}_{bi}^B & \mathbf{Z}_{bb}^B \end{bmatrix}; \quad \mathbf{Y} \triangleq \begin{bmatrix} \mathbf{Y}_{ii}^A & \mathbf{Y}_{ib}^A & \mathbf{0} & \mathbf{0} \\ \mathbf{Y}_{bi}^A & \mathbf{Y}_{bb}^A & \mathbf{0} & \mathbf{0} \\ \mathbf{0} & \mathbf{0} & \mathbf{Y}_{ii}^B & \mathbf{Y}_{ib}^B \\ \mathbf{0} & \mathbf{0} & \mathbf{Y}_{bi}^B & \mathbf{Y}_{bb}^B \end{bmatrix} \quad (2.14)$$

Correspondingly the equations of motion are:

$$\mathbf{Z}\mathbf{u} = \mathbf{f} + \mathbf{g} \quad (2.15a)$$

$$\mathbf{u} = \mathbf{Y}(\mathbf{f} + \mathbf{g}) \quad (2.15b)$$

2.2.1 Primal assembly

The primal assembly is based on dynamic stiffness formulation and is eventually described in generalized coordinates \mathbf{q} . Substitution of equation 2.4 in equation 2.15a and pre-multiplication by \mathbf{L}^T results in:

$$\mathbf{L}^T \mathbf{Z} \mathbf{L} \mathbf{q} = \mathbf{L}^T \mathbf{f} + \mathbf{L}^T \mathbf{g} \quad (2.16)$$

Substitution of equation 2.8 into equation 2.16, results in a coupled and determined system in a generalized coordinate system:

$$\hat{\mathbf{Z}} \mathbf{q} = \mathbf{p} \text{ with } \hat{\mathbf{Z}} \triangleq \mathbf{L}^T \mathbf{Z} \mathbf{L} \text{ and } \mathbf{p} = \mathbf{L}^T \mathbf{f} \quad (2.17)$$

Similarly, the system has a primal flexibility matrix $\hat{\mathbf{Y}}$, which can be found through inversion of primal stiffness $\hat{\mathbf{Z}}$. Also, as \mathbf{L} is basically a transformation matrix, it can be used to retrieve the dual formulation without losing the coupling between substructures.

2.2.2 Dual assembly

Contrary to the primal assembly, the dual assembly uses the flexibility notation of the equations of motion. Equation 2.8 is substituted in 2.15b.

$$\mathbf{u} = \mathbf{Y}(\mathbf{f} - \mathbf{B}^T \boldsymbol{\lambda}) \quad (2.18)$$

Pre-multiplication by \mathbf{B} and taking equation 2.3 into account, this results in:

$$\mathbf{B} \mathbf{Y}(\mathbf{f} - \mathbf{B}^T \boldsymbol{\lambda}) = \mathbf{0} \quad (2.19)$$

Simple matrix operations result in the solution for $\boldsymbol{\lambda}$:

$$\boldsymbol{\lambda} = (\mathbf{B} \mathbf{Y} \mathbf{B}^T)^{-1} \mathbf{B} \mathbf{Y} \mathbf{f} \quad (2.20)$$

Returning this result for $\boldsymbol{\lambda}$ to equation 2.18 finds a clear relation between \mathbf{u} and \mathbf{f} , through dually coupled flexibility matrix $\tilde{\mathbf{Y}}$:

$$\mathbf{u} = \tilde{\mathbf{Y}} \mathbf{f} \text{ where } \tilde{\mathbf{Y}} \triangleq [\mathbf{I} - \mathbf{Y} \mathbf{B}^T (\mathbf{B} \mathbf{Y} \mathbf{B}^T)^{-1} \mathbf{B}] \mathbf{Y} \quad (2.21)$$

Either results of equations 2.17 and 2.21 thus yield coupled expressions of the regarded structure, eliminating the unknown boundary forces from the equation through tactfully submitting its corresponding conditions.

2.3 Substructuring on a reduced basis

In order to gain computational efficiency, one may choose to work with a reduced basis. To prevent a great loss of accuracy, this is usually done in a modal coordinate system. This strategy is referred to as Component Mode Synthesis and features wide variety of bases, of which Guyan, Rubin and Craig-Bampton are ones of the most famous. Construction of some reliable reduction bases will be elaborated in chapter 3.

The principle of working with a reduced basis is similar as transformation between primal and dual formulation, as described previously. The physical coordinates are related to generalized coordinates $\boldsymbol{\eta}$, through an $n \times m$ reduction matrix \mathbf{R} , for which $n \geq m$. In the case that $n = m$, transformation is applied without reduction.

$$\mathbf{u} = \mathbf{R} \boldsymbol{\eta} \quad (2.22)$$

Substituting equation 2.22 in the equations of motion 2.15a and premultiplying with \mathbf{R}^T results in:

$$\mathbf{R}^T \mathbf{Z} \mathbf{R} \boldsymbol{\eta} = \mathbf{R}^T (\mathbf{f} + \mathbf{g}) \text{ or } \mathbf{Z}_m \boldsymbol{\eta} = \mathbf{f}_m + \mathbf{g}_m \quad (2.23)$$

Providing that $\boldsymbol{\eta} = \mathbf{R}^+ \mathbf{u}$, $\mathbf{f}_m = \mathbf{R}^T \mathbf{f}$ and $\mathbf{g}_m = \mathbf{R}^T \mathbf{g}$, the reduced flexibility matrix \mathbf{Y}_m can also be found:

$$\mathbf{Y}_m = \mathbf{R}^+ \mathbf{Y} (\mathbf{R}^T)^+ \text{ such that } \boldsymbol{\eta} = \mathbf{Y}_m (\mathbf{f}_m + \mathbf{g}_m) \quad (2.24)$$

Equations 2.23 and 2.24 can be directly submitted to the assembly procedure. Note that interface conditions also need a description in the reduced domain. It can be easily found that:

$$\mathbf{B}_m = \mathbf{B} \mathbf{R} \quad (2.25)$$

and

$$\mathbf{L}_m = \mathbf{R}^+ \mathbf{L} \quad (2.26)$$

In general \mathbf{B}_m and \mathbf{L}_m are not Boolean due to the transformation. As mentioned for \mathbf{B} and \mathbf{L} , also \mathbf{B}_m and \mathbf{L}_m can form each others' null spaces.

Equivalently to equations 2.17 and 2.21, a coupled system is obtained in the reduced domain, either through primal coordinates $\boldsymbol{\eta}_{primal}$:

$$\hat{\mathbf{Z}}_m \boldsymbol{\eta}_{primal} = \mathbf{p}_m \text{ with } \hat{\mathbf{Z}}_m \triangleq \mathbf{L}_m^T \mathbf{Z}_m \mathbf{L}_m \text{ and } \mathbf{p}_m = \mathbf{L}_m^T \mathbf{f}_m \quad (2.27)$$

or dually:

$$\boldsymbol{\eta} = \tilde{\mathbf{Y}}_m \mathbf{f}_m \text{ where } \tilde{\mathbf{Y}}_m \triangleq [\mathbf{I} - \mathbf{Y}_m \mathbf{B}_m^T (\mathbf{B}_m \mathbf{Y}_m \mathbf{B}_m^T)^{-1} \mathbf{B}_m] \mathbf{Y}_m \quad (2.28)$$

Solutions in the physical domain are retrieved through transformation again using \mathbf{R} . Primal coordinates can be transformed to dual by choice, either in the reduced domain using \mathbf{L}_m , or in the physical domain with \mathbf{L} .

2.4 Non-conforming interfaces

In practice, it may not always be the case that an interface is described with the same physical DoFs on each substructure. Considering FEM, this would for example be the case if the meshes of to be coupled substructures do not match (see figure 2.2).

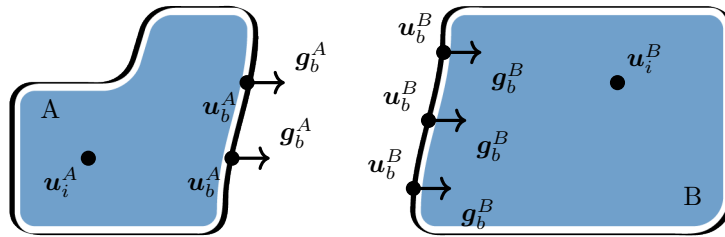


Figure 2.2: Two substructures with non-conforming DoFs

The simplest way to achieve conformance in the physical domain, is using so called node collocation. The DoF of both sides are related to the set of interface DoF \mathbf{u}_γ through a matrix \mathbf{D} , such that for all s substructures:

$$\mathbf{u}_b^{(s)} = \mathbf{D}_b^{(s)} \mathbf{u}_\gamma \quad (2.29)$$

The most common way to define \mathbf{D}_b is by relating coordinates through element shape functions. Though \mathbf{u}_γ can be arbitrarily chosen, it is most practical to choose master- and slave substructures, where for the master substructure defines \mathbf{u}_γ . The physical interpretation of this procedure is illustrated in figure 2.3.

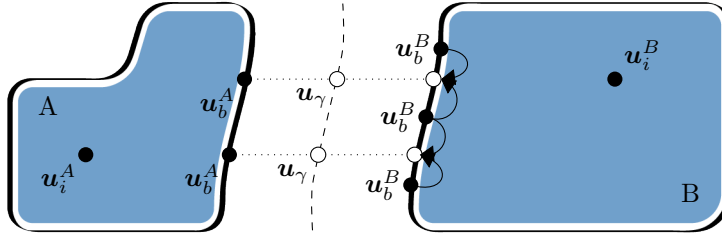


Figure 2.3: Original coordinates are collocated at substructure B, so to match substructure A

In order to minimize the error, one can also solve the issue with least squares compatibility. The approach is elaborated in [32].

Another option is to define compatibility in the reduced domain. As often, motion of the interface is described in mode shapes that do not include motion in the interior DoF, compatibility is also accomplished by forcing the modal amplitudes to be equal on both sides of the interface. This requires both sides of the interface to be described with the same set of modes though. Since the focus of this thesis is set on such an interface description, this method (illustrated in figure 2.4) will be the most obvious option.

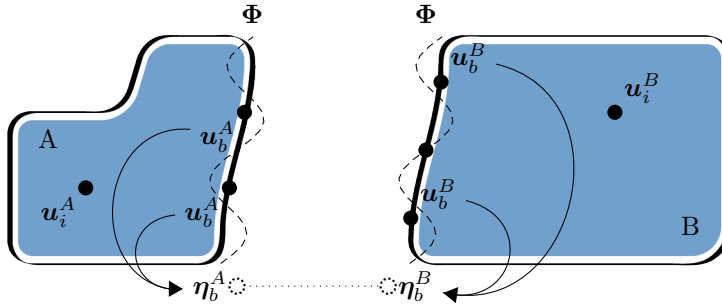


Figure 2.4: Compatibility is obtained through transformation to a modal domain

2.5 Additional interface physics

Instead of equalizing the displacement field of both sides of the interface, it is also possible to add additional stiffness, damping or mass between the both substructures. Voormeeren's derivation can be easily rewritten suiting the substructuring formulation according to this chapter [4].

2.5.1 Stiffness and damping

Considering stiffness and damping, physically it becomes obvious that the interface DoF of different substructures do not longer coincide. Therefore, it is not possible to assemble the substructures in primal coordinates. One has the choice however, to make use of either dynamic stiffness or flexibility formulation. Instead of equation 2.3, the interface displacements are related through:

$$\Delta \mathbf{u}_b = \mathbf{u}_b^A - \mathbf{u}_b^B = \mathbf{B}_b \mathbf{u}_b \quad (2.30)$$

where:

$$\mathbf{u}_b = \begin{bmatrix} \mathbf{u}_b^A \\ \mathbf{u}_b^B \end{bmatrix} \text{ and } \mathbf{B}_b = [\mathbf{I} \quad -\mathbf{I}] \quad (2.31)$$

Note that every entry in $\Delta \mathbf{u}_b$ contains a relation between one DoF of each substructure and thus this vector has a length equal to the amount of relations defined through local Boolean matrix \mathbf{B}_b . The same principal holds for the velocity at the interface:

$$\Delta \dot{\mathbf{u}}_b = \mathbf{B}_b \dot{\mathbf{u}}_b \quad (2.32)$$

The intensity of the interface forces, can now be described in terms of additional stiffness and damping.

$$\boldsymbol{\lambda} = \boldsymbol{\kappa}_{bb} \mathbf{B}_b \mathbf{u}_b + \boldsymbol{\delta}_{bb} \mathbf{B}_b \dot{\mathbf{u}}_b \quad (2.33)$$

Here $\boldsymbol{\kappa}_{bb}$ and $\boldsymbol{\delta}_{bb}$ respectively, are the boundary stiffness and boundary damping matrices. They are generally diagonal matrices where the j^{th} diagonal entry contains the stiffness or damping between the two DoF related through the j^{th} row of \mathbf{B}_b . Substitution of equation 2.33 in 2.8 results in the following expression for the interface forces:

$$\mathbf{g}_b = -\mathbf{B}_b^T \boldsymbol{\kappa}_{bb} \mathbf{B}_b \mathbf{u}_b - \mathbf{B}_b^T \boldsymbol{\delta}_{bb} \mathbf{B}_b \dot{\mathbf{u}}_b \quad (2.34)$$

Since the problem is considered in the frequency domain, the velocity is expressed as $\dot{\mathbf{u}}_b = i\omega \mathbf{u}_b$. Substitution of equation 2.34 into either 2.15a or 2.15b and rearranging the results in flexibly/damped coupling as illustrated by figure 2.5:

$$(\mathbf{Z} + \mathbf{B}^T \boldsymbol{\kappa}_{bb} \mathbf{B} + i\omega \mathbf{B}^T \boldsymbol{\delta}_{bb} \mathbf{B}) \mathbf{u} = \mathbf{f} \quad (2.35)$$

and:

$$\mathbf{u} = (\mathbf{I} + \mathbf{Y} \mathbf{B}^T \boldsymbol{\kappa}_{bb} \mathbf{B} + i\omega \mathbf{Y} \mathbf{B}^T \boldsymbol{\delta}_{bb} \mathbf{B})^{-1} \mathbf{Y} \mathbf{f} \quad (2.36)$$

Because of the altered meaning of the assembly formulation, it is practically not convenient to assemble rigid and flexible interface connections with the same assembly operation. One may also assume a rigid interface connection to be very stiff instead, though this could affect the conditioning of the stiffness matrix. This would rule out the option to define the DoF in the primal formulation.

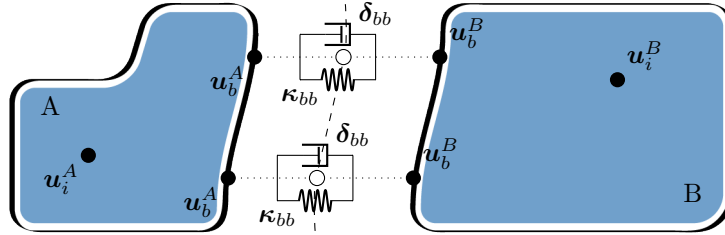


Figure 2.5: Two substructures connected through spring-dashpot elements

2.5.2 Inertia

Another option is to allocate additional mass to a coupling, as in figure 2.6. In this case, one is bound to use the primal formulation. Due to the inertia at the interface, force equilibrium no longer holds. The difference in interface forces is described as:

$$\Delta \mathbf{g}_b = \mathbf{L}^T \mathbf{g}_b \quad (2.37)$$

Considering Newton's second law with the added inertia $\boldsymbol{\mu}_{bb}$ taken into account, the following is obtained:

$$\boldsymbol{\mu}_{bb} \ddot{\mathbf{u}}_b = -\Delta \mathbf{g}_b = -\mathbf{L}^T \mathbf{g}_b \quad (2.38)$$

Similar as for the velocity, the acceleration in the frequency domain can be described as $\ddot{\mathbf{u}}_b = -\omega^2 \mathbf{u}_b$.

Returning to equation 2.15a and pre-multiplying it by \mathbf{L}^T , equation 2.38 is substituted to eliminate the interface forces. Transforming dual to primal coordinates, the equation of motion results in:

$$(\mathbf{L}^T \mathbf{Z} \mathbf{L} + \mu_{bb} \omega^2) \mathbf{q} = \mathbf{p} \quad (2.39)$$

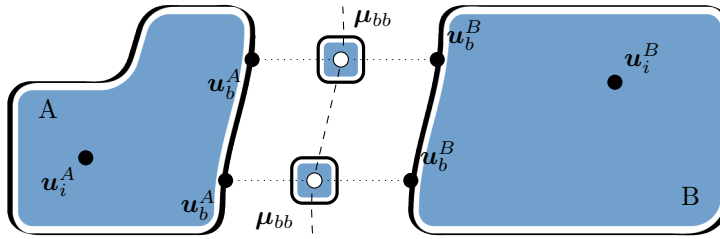


Figure 2.6: Inertia is added at the interface between two substructures A and B

Chapter 3

Component Mode Synthesis

The dynamic substructuring method where Model Order Reduction (MOR) and component-wise analysis are combined, is known as Component Mode Synthesis (CMS). Motions of individual substructures are described with a set of mode shapes. With a proper choice for which modes to use, one can truncate many modes of low significance such that the retained modes cover the most dominant behaviour of the substructure. This results in a large improvement in computational efficiency at the slight cost of accuracy.

Two types of CMS methods can be distinguished: free interface, and fixed interface methods. The main difference, as the names suggest, is in the choice of using eigenmodes of a constrained or unconstrained situation. Though for computational analysis, both reduction types are feasible, in experimental analysis this is not always the case. Fixed interface modes can not always be determined and the same holds for the static enrichment of the reduction basis.

As suggested, a reduction basis separates a static and a dynamic contribution to the motion:

$$\mathbf{u} = \mathbf{u}_{stat} + \mathbf{u}_{dyn} \quad (3.1)$$

Since both parts are represented by a modal set, this can generally be denoted as:

$$\mathbf{u} = \mathbf{\Psi}\boldsymbol{\eta}_{stat} + \mathbf{\Phi}\boldsymbol{\eta}_{dyn} \text{ or } \mathbf{u} = \mathbf{R}\boldsymbol{\eta} \quad (3.2)$$

The actual content of static mode set $\mathbf{\Psi}$ and dynamic mode set $\mathbf{\Phi}$ varies per method. This chapter first covers the possible mode types used in CMS methods, where after some classical reduction techniques are elaborated. An extensive description can also be found in [4].

For some reduction methods, mostly fixed interface methods, interior and boundary DoF are distinguished, which is also important for deriving modal bases. Prior definition of Dirichlet boundary conditions is lucrative for computing a better interior reduction basis with better fitting fixed interface modes. A partitioned set of equations is formulated as:

$$\begin{bmatrix} \mathbf{M}_{ii} & \mathbf{M}_{ib} \\ \mathbf{M}_{bi} & \mathbf{M}_{bb} \end{bmatrix} \begin{bmatrix} \ddot{\mathbf{u}}_i \\ \ddot{\mathbf{u}}_b \end{bmatrix} + \begin{bmatrix} \mathbf{K}_{ii} & \mathbf{K}_{ib} \\ \mathbf{K}_{bi} & \mathbf{K}_{bb} \end{bmatrix} \begin{bmatrix} \mathbf{u}_i \\ \mathbf{u}_b \end{bmatrix} = \begin{bmatrix} \mathbf{f}_i \\ \mathbf{f}_b \end{bmatrix} + \begin{bmatrix} \mathbf{0} \\ \mathbf{g}_b \end{bmatrix} \quad (3.3)$$

3.1 Vibration modes

The dynamic part of the displacement is represented by vibration modes. Truncation of insignificant vibration modes is a key operation to order reduction.

3.1.1 Free interface modes

Free interface modes represent the possible deformation shapes of a system when it is enabled to vibrate freely. Unlike fixed interface modes, they are determined assuming a fully unconstrained interface. Due to this assumption, a full set of free interface modes suffices to describe the motion of the system despite any actual constraints at the interface. The eigenfrequencies are obtained by solving the following eigenvalue problem:

$$(\mathbf{K} - \omega^2 \mathbf{M})\mathbf{u} = \mathbf{0} \quad (3.4)$$

Or including the j th eigenmode $\phi_{f,j}$ directly in the equation:

$$(\mathbf{K} - \omega_{f,j}^2 \mathbf{M})\phi_{f,j} = \mathbf{0} \quad (3.5)$$

The resulting eigenvectors are collected in set Φ_f , which is then truncated before applied in the reduction basis.

3.1.2 Fixed interface modes

Similar to free interface modes, the fixed interface modes are eigenmodes of the system, but assuming the boundary DoF to be fully constrained. The latter is done by omitting all entries related to boundary DoF from the system of equations, since all boundary DoF are taken to be 0. This reduces the eigenvalue problem to a similar equation as for free interface modes, but solely with the interior partition:

$$(\mathbf{K}_{ii} - \omega_{i,j}^2 \mathbf{M}_{ii})\phi_{i,j} = \mathbf{0} \quad (3.6)$$

Note that the actual motion at the boundary is not described at all by fixed interface modes and therefore require a separate formulation, which can be done in their original domain or through their own modal transformation. The latter is a key procedure in the context of thesis and will be elaborated in chapter 4.

3.1.3 Rigid body modes

Rigid body modes can both be considered a vibration mode as a type of static mode. They allow a system to be displaced as a whole, either translational or rotational. No deformation occurs in rigid body motion and thus their modes fulfil the following restriction:

$$\mathbf{K}\Phi_r = \mathbf{0} \quad (3.7)$$

If a system is under- or unconstrained, rigid body modes arise naturally from the eigenmode analysis. They can also be found by solving equation 3.7 through finding the nullspace of the stiffness matrix. Another option is to obtain the rigid body modes geometrically. This procedure is described in [4].

3.2 Static modes

The reduced basis of vibration modes is enriched by a set of static modes. An important property of these modes is that they allow for correct interface compatibility enforcement. While constraint modes are used to complement fixed interface vibration modes, (residual) attachment modes enrich the static basis for free interface vibration modes. They are described in the following subsections.

3.2.1 Constraint modes

The constraint mode is a type of mode used in fixed interface methods. It represents the static deformation of the interior DoF due to unit displacements of the constrained boundary DoF. Its expression follows from the partitioned equations of motion with reference to the interior properties at 0 frequency and no additional forces:

$$\mathbf{K}_{ii}\mathbf{u}_i + \mathbf{K}_{ib}\mathbf{u}_b = \mathbf{0} \quad (3.8)$$

Rearranging equation 3.8 leads to a direct relation between \mathbf{u}_i and \mathbf{u}_b :

$$\mathbf{u}_i = -\mathbf{K}_{ii}^{-1}\mathbf{K}_{ib}\mathbf{u}_b = \mathbf{\Psi}_c\mathbf{u}_b \quad (3.9)$$

The resulting matrix $-\mathbf{K}_{ii}^{-1}\mathbf{K}_{ib}$ or $\mathbf{\Psi}_c$ is referred to as the static condensation matrix and contains the constraint modes in its columns.

The constraint modes can also be evaluated at a different frequency ω_s . This frequency should be taken in the quasi-static range in order to form a reliable basis. Since these modes do not represent the truly static situation any more, they are referred to as quasi-static or pseudo-static constraint modes.

The final expression changes slightly compared to equation 3.9:

$$\hat{\mathbf{u}}_i \approx -\mathbf{Z}_{ii}^{-1}(\omega_s)\mathbf{Z}_{ib}(\omega_s)\hat{\mathbf{u}}_b = \hat{\mathbf{\Psi}}_c\hat{\mathbf{u}}_b \quad (3.10)$$

where the accent $\hat{\ast}$ denotes the quasi-static situation, instead of the static one.

3.2.2 Attachment modes

For free interface methods, it is more common to use attachment modes. They represent the static deformations of a structure as a result of separate unit forces at the free interface. The problem is expressed in terms of the full displacement field \mathbf{u} and the interface connection forces \mathbf{g}_b :

$$\begin{bmatrix} \mathbf{K} & -\mathbf{A}^T \\ -\mathbf{A} & \mathbf{0} \end{bmatrix} \begin{bmatrix} \mathbf{u} \\ \mathbf{g}_b \end{bmatrix} = \begin{bmatrix} \mathbf{f} \\ \mathbf{0} \end{bmatrix} \quad (3.11)$$

\mathbf{A} is a Boolean matrix that filters boundary DoF, such that interface connection forcing is only considered at interfaces. Also it is used to enforce compatibility during the assembly. Similar as for constraint modes, external forcing is assumed to be absent. The displacement field at the static frequency then reads:

$$\mathbf{u} = \mathbf{K}^+\mathbf{A}^T\mathbf{g}_b = \mathbf{\Psi}_a\mathbf{g}_b \quad (3.12)$$

In the case where a system has sufficient constraints in order to exclude any rigid body modes, the flexibility matrix \mathbf{K}^+ would ideally be the true inverse of the stiffness matrix. Though if a system allows rigid body displacement, \mathbf{K}^{-1} does not exist and the computation of the attachment modes becomes more complicated. Since the stiffness matrix cannot be inverted, an approximation of its inverse is made under constrained conditions. To optimize the estimation, the temporary constraints should be chosen such that their reaction forces are at a minimum.

Partitioning the temporarily constrained system for constrained DoF \mathbf{u}_c and unconstrained DoF \mathbf{u}_u , the system of equations reads:

$$\begin{bmatrix} \mathbf{K}_{cc} & \mathbf{K}_{cu} \\ \mathbf{K}_{uc} & \mathbf{K}_{uu} \end{bmatrix} \begin{bmatrix} \mathbf{0} \\ \mathbf{u}_u \end{bmatrix} = \begin{bmatrix} \mathbf{f}_c \\ \mathbf{A}_u^T \end{bmatrix} \quad (3.13)$$

Using the constraints to eliminate all entries related to the constraints, the unconstrained partition can be inverted, where after it can be expanded to its original size with 0-entries:

$$\mathbf{K}^+ = \begin{bmatrix} \mathbf{0} & \mathbf{0} \\ \mathbf{0} & \mathbf{K}_{uu}^{-1} \end{bmatrix} = \begin{bmatrix} \mathbf{0} & \mathbf{0} \\ \mathbf{0} & \mathbf{G}_{uu} \end{bmatrix} = \mathbf{G}_c \quad (3.14)$$

where \mathbf{G}_c is referred to as the constrained flexibility matrix.

In order for equation 3.12 to be solvable, a projection of \mathbf{A}^T is used instead, such that the equilibrating interface forces are orthogonal to the system's rigid body modes:

$$\mathbf{A}_{eq}^T = \mathbf{P}\mathbf{A}^T \quad (3.15)$$

where projection matrix \mathbf{P} is defined as:

$$\mathbf{P} = \mathbf{I} - \mathbf{M}\Phi_r\Phi_r^T \quad (3.16)$$

After these operations, equation 3.12 is rewritten to:

$$\tilde{\Psi}_a = \mathbf{G}_c\mathbf{A}_{eq}^T \quad (3.17)$$

The last step is to orthogonalize the attachment modes with respect to the rigid body modes by premultiplication with \mathbf{P}^T , resulting in:

$$\Psi_a = \mathbf{P}^T\mathbf{G}_c\mathbf{P}\mathbf{A}^T \quad (3.18)$$

Similar as for constraint modes, it is an option to take into account the quasi-static behaviour at a central frequency ω_s , such that:

$$\hat{\mathbf{u}} = \mathbf{Z}^+(\omega_s)\mathbf{A}^T\mathbf{g}_b = \hat{\Psi}_a\mathbf{g}_b \quad (3.19)$$

Application of attachment modes is more likely to occur in experimental methods than in numerical methods. Their computation can be extensive while attachment modes can be easily obtained experimentally. Instead, numerical methods may use residual attachment modes which carry more beneficial properties than the original attachment modes.

3.2.3 Residual attachment modes

The residual attachment modes adapt to the modal selection of the free interface vibration modes. The flexibility matrix can be built using spectral expansion of all n free interfaces modes:

$$\mathbf{G}_f = \sum_{j=n_r+1}^n \frac{\phi_j\phi_j^T}{\omega_j^2} \quad (3.20)$$

Note that the n_r rigid body modes are synthesized differently and are not taken into account. Since it is undesirable for attachment modes to overlap with already exploited free interface modes, a residual flexibility matrix is constructed omitting the contribution of the m retained free interface modes:

$$\mathbf{G}_r = \mathbf{G}_f - \sum_{j=n_r+1}^m \frac{\phi_j\phi_j^T}{\omega_j^2} \quad (3.21)$$

Similar as for the regular attachment modes, the modal basis is obtained by selecting columns corresponding with boundary DoF excitation:

$$\Psi_r = \mathbf{G}_r\mathbf{A}^T \quad (3.22)$$

3.3 Fixed interface methods

With knowledge of the described mode types, now a reduction basis can be created with the help of these modes. Fixed interface methods are commonly described by static constraint modes as in the Guyan method, and as the name suggests, extended by fixed interface vibration modes, such as in the Craig-Bampton method.

3.3.1 Guyan method

Reduction according to the Guyan method can be considered the simplest reduction type as it solely uses static constraint modes. Since the reduction basis is this limited, the amount of DoF is reduced tremendously for structures with a large number of interior DoF. The reduction comes at a cost of poor dynamic description, thus results are usually only reliable in the lower part of the quasi-static range. Implementation leads to the following system of equations:

$$\begin{bmatrix} \mathbf{u}_i \\ \mathbf{u}_b \end{bmatrix} \approx \begin{bmatrix} \Psi_c \\ \mathbf{I} \end{bmatrix} \mathbf{u}_b = \mathbf{R}_G \boldsymbol{\eta}_G \quad (3.23)$$

3.3.2 Craig-Bampton method

To overcome the main drawback of the Guyan method, the limited range applicability, the Craig-Bampton method expands the Guyan method with the use of fixed interface vibration modes. The system of equations will look as following:

$$\begin{bmatrix} \mathbf{u}_i \\ \mathbf{u}_b \end{bmatrix} \approx \begin{bmatrix} \Phi_i & \Psi_c \\ \mathbf{0} & \mathbf{I} \end{bmatrix} \begin{bmatrix} \boldsymbol{\eta}_i \\ \mathbf{u}_b \end{bmatrix} = \mathbf{R}_{CB} \boldsymbol{\eta}_{CB} \quad (3.24)$$

Introducing a new type of interior DoF $\boldsymbol{\eta}_i$, the amount of modes retained becomes the choice of the user. As a rule of thumb, one retains all the modes with a frequency up to twice the frequency range of interest in order to gain reliable results.

3.4 Free interface methods

In free interface methods, attachment modes and rigid body modes gain a key role, together with free interface vibration modes. Two classical methods are presented, being MacNeal's method and Rubin's method.

3.4.1 MacNeal's method

MacNeal's method, which is very similar to Rubin's method, forms its reduction basis on free interface vibration modes (including rigid body modes), and residual attachment modes. The displacement field is thus approximated by:

$$\mathbf{u} \approx \Psi_r \mathbf{g}_b + \Phi_r \boldsymbol{\eta}_r + \Phi_f \boldsymbol{\eta}_f \quad (3.25)$$

Expressing the original and generalized DoF through reduction matrix \mathbf{R}_{M_1} , the system of equations becomes:

$$\mathbf{u} = \begin{bmatrix} \Phi_r & \mathbf{0} & \mathbf{0} \\ \mathbf{0} & \Phi_f & \mathbf{0} \\ \mathbf{0} & \mathbf{0} & \Psi_r \end{bmatrix} \begin{bmatrix} \boldsymbol{\eta}_r \\ \boldsymbol{\eta}_f \\ \mathbf{g}_b \end{bmatrix} = \mathbf{R}_{M_1} \boldsymbol{\eta}_{M_1} \quad (3.26)$$

Transformation of the original equations of motion to the reduced domain leads to:

$$\begin{bmatrix} \mathbf{I} & \mathbf{0} & \mathbf{0} \\ \mathbf{0} & \mathbf{I} & \mathbf{0} \\ \mathbf{0} & \mathbf{0} & M_{r,bb} \end{bmatrix} \begin{bmatrix} \ddot{\boldsymbol{\eta}}_r \\ \ddot{\boldsymbol{\eta}}_f \\ \ddot{\mathbf{g}}_b \end{bmatrix} + \begin{bmatrix} \mathbf{0} & \mathbf{0} & \mathbf{0} \\ \mathbf{0} & \Omega_f^2 & \mathbf{0} \\ \mathbf{0} & \mathbf{0} & G_{r,bb} \end{bmatrix} \begin{bmatrix} \boldsymbol{\eta}_r \\ \boldsymbol{\eta}_f \\ \mathbf{g}_b \end{bmatrix} = \begin{bmatrix} \Phi_r^T \\ \Phi_f^T \\ \Psi_r^T \end{bmatrix} \mathbf{f} + \begin{bmatrix} \Phi_r^T \\ \Phi_f^T \\ \Psi_r^T \end{bmatrix} \mathbf{g} \quad (3.27)$$

with:

$$G_{r,bb} = \Psi_r^T \mathbf{K} \Psi_r = \mathbf{A} G_r \mathbf{A}^T \text{ and } M_{r,bb} = \Psi_r^T \mathbf{M} \Psi_r$$

Due to the use of attachment modes, the generalized set of DoF is no longer associated to solely displacement DoF, as the set contains \mathbf{g}_b , the interface connection forces. In order to prepare the system of equations for

assembly, it is desirable to express \mathbf{g}_b in terms of (generalized) displacements. Premultiplying equation 3.25 with matrix \mathbf{A} leads to direct selection of interface related quantities:

$$\mathbf{u}_b = \mathbf{A}\mathbf{u} = \mathbf{A}(\Psi_r \mathbf{g}_b + \Phi_r \boldsymbol{\eta}_r + \Phi_f \boldsymbol{\eta}_f) = \mathbf{G}_{r,bb} \mathbf{g}_b + \Phi_{r|b} \boldsymbol{\eta}_r + \Phi_{f|b} \boldsymbol{\eta}_f \quad (3.28)$$

As can be followed through the applied transformation/selection, the subscript $|_b$ denotes the trace on the boundary DoF. Another transformation matrix arises:

$$\begin{bmatrix} \boldsymbol{\eta}_r \\ \boldsymbol{\eta}_f \\ \mathbf{g}_b \end{bmatrix} = \begin{bmatrix} \mathbf{I} & \mathbf{0} & \mathbf{0} \\ \mathbf{0} & \mathbf{I} & \mathbf{0} \\ -\mathbf{K}_{r,bb} \Phi_{r|b} & -\mathbf{K}_{r,bb} \Phi_{f|b} & \mathbf{K}_{r,bb} \end{bmatrix} \begin{bmatrix} \boldsymbol{\eta}_r \\ \boldsymbol{\eta}_f \\ \mathbf{u}_b \end{bmatrix} \text{ or } \boldsymbol{\eta}_{M_1} = \mathbf{R}_{M_2} \boldsymbol{\eta}_{M_2} \quad (3.29)$$

Here $\mathbf{K}_{r,bb}$ is the boundary residual stiffness matrix, which is obtained by inversion of the boundary residual flexibility matrix $\mathbf{G}_{r,bb}$. Up to this step MacNeal's and Rubin's method are the same. Following MacNeal, the residual mass $\mathbf{M}_{r,bb}$ is neglected. Further processing under this assumption, the reduced equations of motion become:

$$\begin{bmatrix} \Phi_r^T \bar{\mathbf{K}}_r \Phi_r & \Phi_r^T \bar{\mathbf{K}}_r \Phi_f & -\Phi_{r|b}^T \mathbf{K}_{r,bb} \\ \Phi_f^T \bar{\mathbf{K}}_r \Phi_r & \Omega_f^2 + \Phi_f^T \bar{\mathbf{K}}_r \Phi_f & -\Phi_{f|b}^T \mathbf{K}_{r,bb} \\ -\mathbf{K}_{r,bb} \Phi_{r|b} & -\mathbf{K}_{r,bb} \Phi_{f|b} & \mathbf{K}_{r,bb} \end{bmatrix} \begin{bmatrix} \boldsymbol{\eta}_r \\ \boldsymbol{\eta}_f \\ \mathbf{u}_b \end{bmatrix} = \begin{bmatrix} \tilde{\mathbf{f}}_r \\ \tilde{\mathbf{f}}_f \\ \tilde{\mathbf{f}}_b \end{bmatrix} + \begin{bmatrix} \mathbf{0} \\ \mathbf{0} \\ \mathbf{g}_b \end{bmatrix} + \dots \quad (3.30)$$

where:

$$\begin{aligned} \bar{\mathbf{K}}_r &= \mathbf{A}^T \mathbf{K}_{r,bb} \mathbf{A} \\ \tilde{\mathbf{f}}_r &= (\Phi_r^T - \Phi_{r|b}^T \mathbf{K}_{r,bb} \Psi_r^T) \mathbf{f} \\ \tilde{\mathbf{f}}_f &= (\Phi_f^T - \Phi_{f|b}^T \mathbf{K}_{r,bb} \Psi_r^T) \mathbf{f} \\ \tilde{\mathbf{f}}_b &= \mathbf{K}_{r,bb} \Psi_r^T \mathbf{f} \end{aligned} \quad (3.31)$$

3.4.2 Rubin's method

As mentioned before, up to equation 3.29, Rubin's method is exactly the same as McNeal's. Unlike McNeal's method, Rubin treats the mass matrix consistently. The reduced equations result in:

$$\begin{bmatrix} \mathbf{I} + \Phi_r^T \bar{\mathbf{M}}_r \Phi_r & \Phi_r^T \bar{\mathbf{M}}_r \Phi_f & -\Phi_{r|b}^T \bar{\mathbf{M}}_r \\ \Phi_f^T \bar{\mathbf{M}}_r \Phi_r & \mathbf{I} + \Phi_f^T \bar{\mathbf{M}}_r \Phi_f & -\Phi_{f|b}^T \bar{\mathbf{M}}_r \\ -\bar{\mathbf{M}}_r \Phi_{r|b} & -\bar{\mathbf{M}}_r \Phi_{f|b} & \mathbf{M}_{r,bb} \end{bmatrix} \begin{bmatrix} \ddot{\boldsymbol{\eta}}_r \\ \ddot{\boldsymbol{\eta}}_f \\ \ddot{\mathbf{u}}_b \end{bmatrix} + \dots \quad (3.32)$$

$$\begin{bmatrix} \Phi_r^T \bar{\mathbf{K}}_r \Phi_r & \Phi_r^T \bar{\mathbf{K}}_r \Phi_f & -\Phi_{r|b}^T \mathbf{K}_{r,bb} \\ \Phi_f^T \bar{\mathbf{K}}_r \Phi_r & \Omega_f^2 + \Phi_f^T \bar{\mathbf{K}}_r \Phi_f & -\Phi_{f|b}^T \mathbf{K}_{r,bb} \\ -\mathbf{K}_{r,bb} \Phi_{r|b} & -\mathbf{K}_{r,bb} \Phi_{f|b} & \mathbf{K}_{r,bb} \end{bmatrix} \begin{bmatrix} \boldsymbol{\eta}_r \\ \boldsymbol{\eta}_f \\ \mathbf{u}_b \end{bmatrix} = \begin{bmatrix} \tilde{\mathbf{f}}_r \\ \tilde{\mathbf{f}}_f \\ \tilde{\mathbf{f}}_b \end{bmatrix} + \begin{bmatrix} \mathbf{0} \\ \mathbf{0} \\ \mathbf{g}_b \end{bmatrix}$$

where:

$$\bar{\mathbf{M}}_r = \mathbf{A}^T \mathbf{K}_{r,bb} \mathbf{M}_{r,bb} \mathbf{K}_{r,bb} \mathbf{A} \quad (3.33)$$

Chapter 4

Interface reduction

Depending on the structures analysed, the ratio between interior DoF and boundary DoF may vary widely. Contrary to the automotive industry, where many connections can be simplified as a point interface, civil engineering structures are often connected over a considerable width or surface area. In the latter case, the interior reductions described in chapter 3 is less effective in terms of amount of DoF it reduces, as a relatively large portion of boundary DoF remains unreduced.

In order to reach a reduced model size for substructures with many boundary DoF, various techniques exist to apply a second reduction, now only aimed at the boundary. Interface reduction is similar to interior reduction from a procedural aspect, but different considerations have to be taken into account. Interface behaviour usually is significantly more dependent of dynamic properties of adjacent substructures compared to motion of interior DoF. Besides, improper choices for an interface reduction basis can cause weakened interface compatibility.

Several methods are elaborated in this chapter, each characterizing a certain approach.

4.1 Interface rigidification

The simplest type of interface reduction is referred to as interface rigidification. As the term suggests, this reduction allows an interface to behave only rigidly. In other words, all flexible motions are removed from its modal basis.

Its restrictions and advantages are similar as for Guyan's interior reduction. Retaining only rigid body modes guarantees a limitation of boundary DoF to the six possible rigid motion directions. Also in this case the reduction comes at the cost of accuracy in a relatively high frequency range.

Though interface rigidification can be considered a very rough approach, it can be justified under certain circumstances. When an interface is much stiffer than its adjacent substructures, the vibration modes of the interface that are now neglected will not be excited through the more flexible structural parts. Especially when the behaviour of the more flexible parts is of greater interest, results will hardly be affected as the flexible parts will not respond significantly to the vibrations of higher frequencies.

When it comes to formulating a reduction basis, the procedure is similar as for interior reduction. Transformation assumes interior DoF to be generalized, whether or not this is actually the case:

$$\begin{bmatrix} \boldsymbol{\eta}_i \\ \boldsymbol{u}_b \end{bmatrix} \approx \begin{bmatrix} \boldsymbol{I} & \mathbf{0} \\ \mathbf{0} & \boldsymbol{\Phi}_{r,b} \end{bmatrix} \begin{bmatrix} \boldsymbol{\eta}_i \\ \boldsymbol{\eta}_{r,b} \end{bmatrix} \quad (4.1)$$

where $\boldsymbol{\Phi}_{r,b}$ contains the rigid body modes of the boundary partition of DoF.

In experimental dynamics, a typical application of this principle can be seen in the virtual point transformation [33]. Measurements on multiple physical points or reduced to rigid body motion in one virtual coupling point. Due to this limited description, interface compatibility is not defined as it may be in more extensive interface reductions. Though this principle has been shown to be applicable for point connections, it has recently been shown that enriching such a basis with basic flexible modes can still improve results significantly [34]. This approach is comparable with the use of a polynomial basis and is also applicable for line or surface interfaces.

4.2 Modal interface reduction

When rigid body modes are insufficient to describe an interface, the modal basis can be expanded with vibration modes. These modes are obtained similarly as fixed interface vibration modes and are referred to as interface displacement modes. Instead of fixing the boundary DoF, now the interior DoF are assumed to be fixed, resulting in a reduced eigenvalue problem:

$$(\tilde{\mathbf{K}}_{bb} - \omega_{\gamma,j}^2 \tilde{\mathbf{M}}_{bb}) \phi_{\gamma,j} = \mathbf{0} \quad (4.2)$$

Note that the mass- and stiffness matrices are considered to be generalized, as depending on the applied interior reduction they may not be the same as the original matrices.

Truncation of the modes obtained results in a reduction basis of familiar form: where Φ_γ is the set of retained interface displacement modes.

$$\begin{bmatrix} \eta_i \\ \mathbf{u}_b \end{bmatrix} \approx \begin{bmatrix} \mathbf{I} & \mathbf{0} \\ \mathbf{0} & \Phi_\gamma \end{bmatrix} \begin{bmatrix} \eta_i \\ \eta_\gamma \end{bmatrix} \quad (4.3)$$

A problem now arises: in general, after truncation, the interface displacement modes computed at boundaries of different substructures will not be the same. Because modes considered at one side at the interface can not always be covered by modes on the other side of the interface, compatibility is weakened.

In order to keep full compatibility it is optional to use the reduction basis of the substructure that is expected to be the most dominant. Again, this principle may work well for substructures with large differences in stiffness. When stiffnesses are of comparable magnitude, often neither found sets will be able to accurately describe the actual interface behaviour.

Besides, the latter option carries the disadvantage of having a dependent reductions basis, in the sense that a reduced order substructure has to be recomputed for different assemblies. Thus, the reduced substructure no longer qualifies as a superelement, which would require the substructure reduction basis to be independent of its further assembly.

4.3 Wave-Based Substructuring

As for the previously described methods, it appears to be hard to efficiently describe interface dynamics without prior knowledge of possible substructures to connect to it. To ensure an accurate interface reduction basis, Wave-Based Substructuring (WBS) has been developed [22]. Interface motions are described by basis functions referred to as 'waves'. These waves are obtained through a global modal analysis of the structure with its real constraints. As the waves ultimately only relate to boundary DoF, the boundary partition of the global waves suffices for a solid basis. Obviously from the abundance of modes with relation to the number of boundary DoF, the partitioned eigenmodes contain redundant information and are thus necessarily linearly dependent at this point. Evidently, this set of modes is truncated to a number (much) smaller than the amount of physical boundary DoF. This does not ensure linear independence, however. Thus to do so, the retained modal set is orthonormalized using a Singular Value Decomposition.

Though WBS proves itself to be a very accurate method, it clearly comes with restrictions. As for the fully compatible approach of modal interface reduction presented earlier, the reduction basis of substructures is dependent of their adjacent parts. Therefore components again do not carry the benefits of superelements. A bottleneck of WBS is the fact that it requires a global analysis. For large models, this alone can be computationally costly, implying a practical restriction in interchanging components for conceptual analyses. Especially with models containing a large number of components, this problem can possibly be alleviated by considering only components of significant influence to compute the wave basis with.

4.4 Orthogonal Polynomial Series

The method promising to mitigate most issues that are encountered with the previously described reduction types, is by use of Orthogonal Polynomial Series (OPS). With this concept, a default series of functions is calculated up to a reliable order and then projected at the concerning interface. This approach embraces all kinds of functions, though its effectiveness is clearly dependent on the ability to approximate the actual interface modes with the functions of choice. The same holds for orthogonality: the method does not exclude linear dependent functions, but orthogonality is desirable to comprise a solution range as large as possible within the amount of DoF retained.

Evaluating the problems impairing other reduction types with respect to OPS, the method has many advantages. Since an interface is described with the same projection on all connected substructure boundaries, full compatibility is easily obtained. This suggestions implies a prior choice of the polynomial order and seems dependent on properties of the parts to which a substructure is to be connected. The latter is true, though with the knowledge that stiffer substructures are dominant over the interface behaviour, the extent to which connected substructure can increase high frequency motion at the interface is limited. By expanding OPS from terms that fit well with low frequent modes to terms that are more suitable for modes with higher frequency, the maximum error using a polynomial basis converges after an order which can be estimated.

4.4.1 Legendre polynomials

A suggested option is the use of Legendre polynomials [24]. The Legendre polynomial terms are by definition orthogonal on the interval $x = [-1, 1]$ and it's shapes appear to be sensible with respect to possible interface motion.

The Legendre function sought for, are solutions of Legendre's differential equation:

$$\frac{d}{dx} \left((1-x^2) \frac{d}{dx} P_n(x) \right) + n(n+1)P_n(x) = 0 \quad (4.4)$$

where n is an integer.

Though the solutions for equation 4.4 can be expressed clearly for chosen integers, the general expression of the solution is practically described recursively:

$$P_{n+1} = \frac{(2n+1)xP_n(x) - nP_{n-1}(x)}{n+1} \quad (4.5)$$

With equation 4.5, the polynomial basis for the interface reduction can easily be expanded up to a satisfactory order, granted the solutions for $n = 0$ and $n = 1$:

$$\begin{cases} P_0(x) = 1 \\ P_1(x) = x \end{cases} \quad (4.6)$$

Some of the lower order terms are plotted in figure 4.1a. It can be recognized that the solutions for $n = 0$ and $n = 1$ are an exact representation of respectively a translational and a rotational rigid body mode. Increasing the order, the solutions appear to be more wave shaped, higher frequent with higher order.

4.4.2 Fourier series

A well known trigonometric polynomial series is the Fourier series. It is mostly used as a tool for approximating a functions with a finite number of sinusoidal terms. Also Fourier series is the basis of the Fourier transform and can be interpreted as its discretized ingredients. With prior knowledge that a limited set of Fourier functions is well able to approximate many functions, the series may as well be a suitable candidate to describe interface motion. A general formulation of Fourier series up to the k^{th} order is given as:

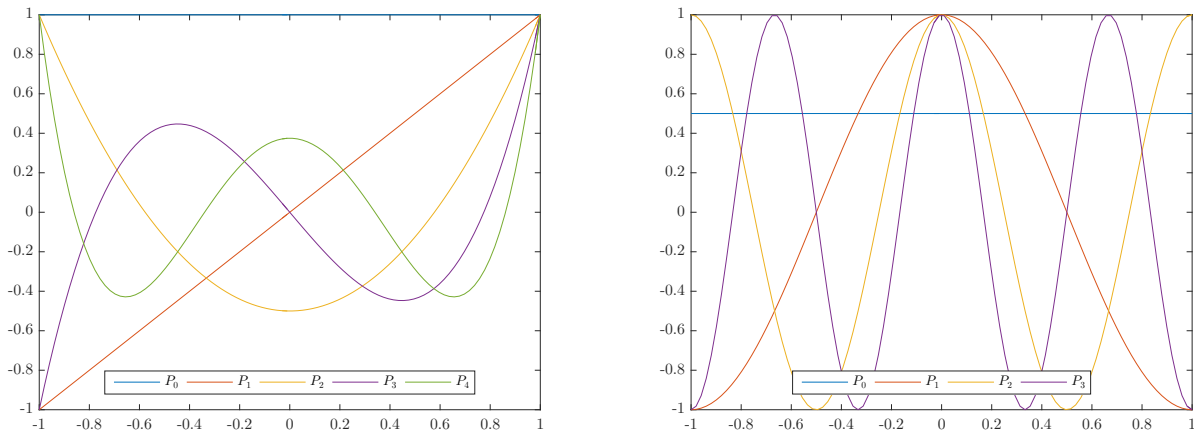
$$P(x) = \frac{a_0}{2} + \sum_{n=1}^k [a_n \cos(nx) + b_n \sin(nx)] \quad (4.7)$$

or denoting every order separately for any non zero integer n :

$$P_n(x) = a_n \cos(nx) + b_n \sin(nx) \quad (4.8)$$

The coefficients a_n and b_n are the amplitudes of each sinusoidal basic term and is dependent on the function that the series should approximate. Note that unlike Legendre polynomials, the Fourier series use either two real terms, or one complex term for every frequency because basic sinusoidal functions are described by both an amplitude and a phase angle. This fact should be taken into account when the order of a Fourier series is compared to the order of a Legendre polynomial.

Similar as Legendre polynomials, the individual terms of the Fourier series are all orthogonal at a certain range. Due to the infinitely repetitive property of sinusoidal functions, there exist infinitely many ranges where orthogonality is obtained. As the lowest non-zero frequency ($n = 1$) terms govern the size of the repetitive pattern, any range of x with a round multiple of 2π suffices. An obvious default range would be $x = [-\pi, \pi]$.



(a) Legendre solutions for $n = 0, 1, 2, 3, 4$

(b) Fourier terms for $n = 0, 1, 2, 3$ with $a_n = 1, b_n = 0$

Figure 4.1: Two types of Orthogonal Polynomial Series

Figure 4.1b shows the lowest order cosine terms of a default Fourier series. As well as for the Legendre polynomials, the 0^{th} order Fourier term is a constant, thus directly representing translational rigid body motion. Rotational rigid body motion on the contrary, is not covered by a single Fourier term. Instead a linear function

which described this motion, is approximated with sinusoidal terms, which may govern the required number of Fourier terms for relatively stiff parts. In some cases it is therefore advisable to include a linear function directly in the interface reduction basis. Though orthogonality is impaired by this measure, it can be beneficial for the accuracy of the results.

Chapter 5

Damping and viscoelasticity in Component Mode Synthesis

Often in civil engineering, little information is available about damping properties of structures. Assumptions are made, usually such that they add no complications to the existing analysis procedures. For some applications, rough assumptions regarding damping may affect analysis results significantly. Therefore it would be desirable to process more realistic damping models in CMS or FEM in general. The classical CMS formulations do generally not account for damping. Depending on the type of damping acting on a structure, additional measures can be taken to take the effects into account.

In some cases the cause of damping lies externally, may it be a viscous medium or a rough surface inducing dry friction. Damping is also prompted internally to some extent, due to intermolecular friction. In dynamic systems, this occurrence tends to interact with elastic material properties as well: it is spoken of viscoelasticity.

The aim of this chapter is to distinguish several damping/viscoelastic models and how they are taken into account in CMS practice. This involves the use of complex vibration modes, for which an approximative method is presented. Two specifically designed reduction bases are introduced, of which one uses fixed interface vibration modes while the other is characterized by the free interface alternatives.

Two damping categories are treated, not necessarily exclusive to each other:

- **Proportional damping:** the damping matrix is a linear combination of the mass- and stiffness matrix. The generalized damping matrix is therefore diagonalizable which means the system of equations can easily be decoupled in a modal analysis.
- **Frequency dependent damping:** some materials may show 'fading memory' behaviour. This means that it's damping (and possibly stiffness) properties are dependent on motion in the past, where the most recent motion usually has the most influence. When this property is considered in the frequency domain, the time dependence is transformed to frequency dependence. The system of equations does not become non-linear with this property.

5.1 Proportional damping

One of the most famous and widely used damping models in civil engineering is the proportional model, first addressed by Rayleigh [35]. The damping model is constructed of a linear combination of the mass- and stiffness matrix:

$$C = \alpha_1 M + \alpha_2 K \quad (5.1)$$

where α_1 and α_2 are weighing constants which relate to the damping ratio ζ as follows:

$$\zeta(\omega) = \frac{1}{2} \left(\frac{\alpha_1}{\omega} + \alpha_2 \omega \right) \quad (5.2)$$

There is no physical reasoning behind this choice of model, but rather a mathematical one. Performing a regular modal analysis on an undamped MDoF structure, an uncoupled system of equations is simply obtained by transformation to modal coordinates:

$$\Phi^T M \Phi \ddot{\eta} + \Phi^T K \Phi \eta = \Phi^T f \quad (5.3)$$

or:

$$I \ddot{\eta} + \Omega^2 \eta = \Phi^T f \quad (5.4)$$

where Ω^2 is a diagonal matrix containing the eigenvalues of the system.

Since it is clear, that M and K become diagonal in the modal domain, this implies the same for the damping matrix C as defined in equation 5.3. Because C is a linear combination of M and K , the modal damping matrix is also a linear combination of the modal mass and stiffness matrices. The modal damping matrix is therefore diagonal and thus a Rayleigh damped system contains the advantageous property of being uncoupled after modal transformation. Due to the assembly, in CMS this orthogonality property cannot be exploited in this manner.

Now including the damping matrix into the equations of motion yields:

$$I \ddot{\eta} + 2\Omega \zeta + \Omega^2 \eta = \Phi^T f \quad (5.5)$$

where ζ is a diagonal matrix containing the modal damping ratio's, such that:

$$\Phi^T C \Phi = 2\Omega \zeta \quad (5.6)$$

Solving the eigenvalue problem of a Rayleigh damped system, one will find approximately the same eigenmodes as for the undamped system. Therefore the system can be analysed with the basic procedures described in chapter 3.

Using an arbitrary reduction matrix R and assuming no exceptional case, the reduced system of equations will be simply expanded to:

$$R^T M R \ddot{\eta} + R^T C R \dot{\eta} + R^T K R \eta = R^T f + R^T g \quad (5.7)$$

In the frequency domain formulation, nothing changes but the content of the dynamic stiffness or flexibility matrix, where damping terms should now be taken into account.

5.2 Frequency dependent damping

When considering a frequency dependent damping model, the dynamics can be approached more in a physical sense. Many viscoelastic materials show frequency dependent behaviour. This section elaborates on various insightful viscoelastic material models finding their relation with load frequencies.

Typical in viscoelastic materials is that they both have properties of elasticity as viscosity. This results in asynchronous behaviour of stress and strain, leading to a time dependent constitutive relation. In order to understand the relation between a viscoelastic material model and the equations of motion of a system including this model, the simplest case of viscoelasticity is considered: the Kelvin-Voigt model.

5.2.1 Kelvin-Voigt model

Though the Kelvin-Voigt model does not lead to a frequency dependent damping matrix, it is a typical and illustrative model for viscoelastic behaviour. As can be seen in figure 5.1, the Kelvin-Voigt model is nothing else but a parallel combination of a spring and a dashpot with linear coefficients, expressed respectively through elastic modulus E and viscosity ξ (not to be confused with damping ratio ζ). This allows a demonstration using the classical SDoF mass-spring-dashpot system. The stress is expressed as a function of strain:

$$\sigma(t) = E\varepsilon(t) + \xi \frac{d\varepsilon(t)}{dt} \quad (5.8)$$

Now assuming the system to be strain controlled by sinusoidal motion, the strain is expressed as follows:

$$\varepsilon(t) = \bar{\varepsilon} e^{i\omega t} \quad (5.9)$$

where $\bar{\varepsilon}$ denotes the amplitude of the strain function. Substituting this strain function into the stress function results in:

$$\sigma(t) = \bar{\varepsilon} * e^{i\omega t} (E + i\omega\xi) \quad (5.10)$$

or:

$$\sigma(t) = (E + i\omega\xi)\varepsilon(t) = E^*(\omega)\varepsilon(t) \quad (5.11)$$

The stress and strain are now related through a complex, frequency dependent term referred to as the dynamic modulus $E^*(\omega)$ of which the real part is the storage modulus E' , and the imaginary part is the loss modulus E'' . The ratio between the storage modulus and the loss modulus describes the phase difference between the sinusoidal stress and strain and is commonly described through loss angle δ :

$$\tan \delta = \frac{E''}{E'} \quad (5.12)$$

Projecting the resulting element properties in the general context of an arbitrary SDoF mass-spring system, the equation of motion is now formulated using the dynamic modulus:

$$m\ddot{u}(t) + (E + i\omega\xi)u(t) = f(t) \quad (5.13)$$

Transformation to the frequency domain leads to the familiar equation:

$$(-m\omega^2 + i\omega\xi + E)U(\omega) = F(\omega) \quad (5.14)$$

where U and F respectively represent the Fourier transform of the displacement u and the force f .

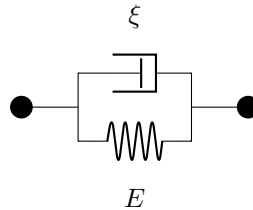


Figure 5.1: Schematization of the Kelvin-Voigt model

5.2.2 Maxwell model

The Maxwell model is represented by a combination of a spring and dashpot in series. Since the stress in the spring and the dashpot are equal and the total strain is the sum of the strain in both the spring and the dashpot, the following constitutive relation is obtained:

$$E \frac{d\varepsilon(t)}{dt} = \frac{\sigma(t)}{dt} + \frac{E}{\xi} \sigma(t) \quad (5.15)$$

The motion is again assumed sinusoidal, but now through prescribing the stress:

$$\sigma(t) = \bar{\sigma} * e^{i\omega t} \quad (5.16)$$

Substituting the assumed motion in the constitutive equation and describing the stress in terms of its own derivative:

$$\frac{d\varepsilon(t)}{dt} = \left(\frac{1}{E} - \frac{i}{\omega\xi} \right) \frac{d\sigma(t)}{dt} \quad (5.17)$$

From this equation it becomes clear that stress and strain are again linearly related over time. Thus with the assumption of sinusoidal loading, stress and strain are equally related as their derivatives. The dynamic modulus is found:

$$E^*(\omega) = \frac{1}{1/E - i/(\omega\xi)} \quad (5.18)$$

Stating the corresponding equation of motion and transforming to the frequency domain, it becomes clear that the combined stiffness and damping no longer relates linearly to the excitation frequency:

$$\left(-m\omega^2 + \frac{1}{1/E - i/(\omega\xi)} \right) U(\omega) = F(\omega) \quad (5.19)$$

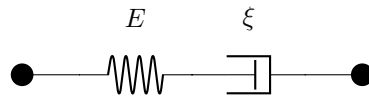


Figure 5.2: Schematization of the Maxwell model

5.2.3 Standard Linear Solid model

The Standard Linear Solid model (SLS) contains both principles of the Kelvin-Voigt model and the Maxwell model by combining a parallel and series assembled elements as in figure 5.3. In similar fashion as for the previous models, the dynamic modulus can be derived, leading to:

$$E^*(\omega) = E_0 + \frac{i\omega E_1}{i\omega + \frac{E_1}{\xi}} \quad (5.20)$$

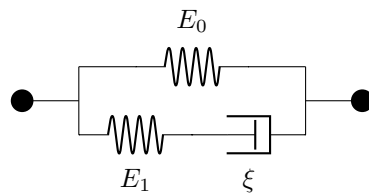


Figure 5.3: Schematization of the Standard Linear Solid model

5.2.4 Generalized Maxwell model

The principle of the SLS model can be extended by adding any combination of Maxwell elements in the parallel assemblage as in figure 5.4, resulting in a model known as the General Maxwell model or Maxwell-Wiechert model. Omitting the elaboration, the dynamic modulus is found to be:

$$E^*(\omega) = E_0 + \sum_j \frac{i\omega E_j}{i\omega + \frac{E_j}{\xi}} \quad (5.21)$$

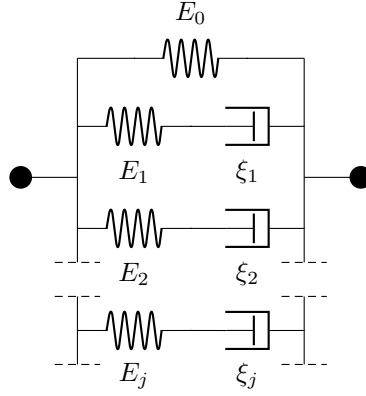


Figure 5.4: Schematization of the Generalized Maxwell model

5.2.5 Advanced models

Though the SLS and generalized Maxwell models may result in decent approximations for some cases, many more models exist for specific applications. For example the GHM model is useful for simulating transient behaviour, Lesieutre and Mingori take anelastic displacements into account, while Adhikari proposes a model aiming for identification of viscous and non-viscous damping:

Golla-Hughes-McTavish (GHM):

$$G_k(s) = \sum_{k=1}^m G_{\infty} a_k \frac{s + 2\hat{\xi}_k \hat{\omega}_k}{s^2 + 2\hat{\xi}_k \hat{\omega}_k s + \hat{\omega}_k^2}$$

Lesieutre and Mingori:

$$G_k(s) = 1 + \sum_{k=1}^m \frac{\Delta_k s}{s + \beta_k}$$

Adhikari:

$$G_k(s) = c \frac{1 - e^{-st_0}}{st_0}$$

The kernel functions G_k are denoted in the Laplace domain such that:

$$sG(s) + sC + K = E'(s) + E''(s) \quad (5.22)$$

About the Laplace transform...

Though closely related to the Fourier transform, in viscoelastic systems it is more common to work with the Laplace transform. The Laplace transformation is considered to be a more general form of the Fourier transform due to its ability to describe time dependent functions in terms of exponentially increasing or decaying oscillatory terms.

The Laplace transform comes with the restriction that negative time cannot be accounted for, which actually proves to be advantageous in a viscoelastic system. Consider the analytical expressions for the Fourier transform $\mathcal{F}(\omega)$ and the Laplace transform $\mathcal{L}(s)$ of an arbitrary function $h(t)$:

$$\mathcal{F}(\omega) = \frac{1}{\sqrt{2\pi}} \int_{-\infty}^{\infty} h(t)e^{-i\omega t} dt \quad (5.23)$$

$$\mathcal{L}(s) = \frac{1}{\sqrt{2\pi}} \int_0^{\infty} h(t)e^{-st} dt \quad (5.24)$$

A common example of the response of a viscoelastic system in the time domain is a decaying oscillatory function:

$$h(t) = e^{at} \quad (5.25)$$

where a is a complex valued constant with a negative real part.

Now considering transformation of equation 5.25 through both 5.23 and 5.24, one will find the integral in the Fourier transform to be non-converging, while it does converge for the Laplace transform. As the response function decays over time, does it also grow exponentially when $t \rightarrow \infty$, causing the Fourier transform not to exist. Thus bounding time to be non-negative proves to be useful, as in engineering practice one is rarely interested in a response for $t \rightarrow \infty$, hence one may simply choose any point in time to start describing a response and consider it to be non-negative, allowing the Laplace transform to result in a satisfactory solution.

5.3 Complex eigenmodes

Now that proportionality is not a general property any more, eigenmodes may contain significant imaginary parts which should be taken into account for either fixed or free interface methods. Depending on the input of the problem, the complex eigenmodes can be found either exactly or approximately.

5.3.1 The polynomial eigenvalue problem

If the frequency dependence of the damping is known and can be expressed as a polynomial, the eigenvalues can be regularly found through finding the roots r in the polynomial eigenvalue equation, i.e.:

$$(Mr^2 + \mathbf{K} + C_1r + C_2r^2 \dots C_n r^n)\bar{\phi} = \mathbf{0} \quad (5.26)$$

where all frequency dependent terms are separated according to their order of dependence.

5.3.2 Rayleigh's approximative method

The eigenvalue problem cannot always be stated in the form of equation 5.26 though. This may be due to the type of frequency dependence or due to numerical input. In this case, an alternative for computation of eigenmodes is through Rayleigh's method, which is approximative [35]. Woodhouse presents a slightly different

theoretical path, resulting in the same final equations as Rayleigh's approach [31]. A theoretical elaboration according to Woodhouse is followed here, starting with the eigenvalue problem for which every n^{th} damped eigenmode $\bar{\phi}_n$ are sought:

$$-\omega_n^2 \mathbf{M} \bar{\phi}_n + i\omega_n \mathbf{C} \bar{\phi}_n + \mathbf{K} \bar{\phi}_n = 0 \quad (5.27)$$

This method assumes the damped eigenmodes to be a linear combination of all (N) undamped eigenmodes:

$$\bar{\phi}_n = \sum_{j=1}^N \alpha_j \phi_j \text{ where } \alpha_n = 1, |\alpha_j| \ll 1 (j \neq n) \quad (5.28)$$

First the proposed solution of equation 5.28 is substituted into equation 5.27 and premultiplying by the k^{th} undamped eigenmode ϕ_k^T results in:

$$\phi_k^T (-\bar{\omega}_n^2 \mathbf{M} + i\bar{\omega}_n \mathbf{C} + \mathbf{K}) \sum_{j=1}^N \alpha_j \phi_j = 0 \quad (5.29)$$

Regardless of any values for α_j , orthogonality of the undamped modes simplifies the terms related to \mathbf{M} and \mathbf{K} , such that:

$$-\bar{\omega}_n^2 \alpha_k + i\bar{\omega}_n \sum_j C'_{kj} \alpha_j + \omega_k^2 \alpha_k = 0 \quad (5.30)$$

where

$$C'_{kj} \triangleq \phi_k^T \mathbf{C} \phi_j \quad (5.31)$$

Assuming the case where $k = n$ (thus $\alpha_k = 1$) and neglecting second order terms regarding α_j where $j \neq k$, the remaining equation yields:

$$\omega_n^2 - \bar{\omega}_n^2 + i\bar{\omega}_n C'_{nn} \approx 0 \quad (5.32)$$

such that

$$\bar{\omega}_n \approx \pm \omega_n + iC'_{nn}/2 \quad (5.33)$$

Returning to equation 5.30, for the case where $k \neq n$, again neglecting second order terms, an expression for the remaining α_k is found:

$$\alpha_k \approx \frac{i\omega_n C'_{kn}}{(\omega_n^2 - \omega_k^2)} \quad (5.34)$$

such that a complete first order approximation for the the undamped eigenmodes exist:

$$\bar{\phi}_n \approx \phi_n + i \sum_{k \neq n} \frac{\omega_n C'_{kn}}{(\omega_n^2 - \omega_k^2)} \phi_k \quad (5.35)$$

Frequency dependent properties do not interfere with this theory. The constant matrix \mathbf{C} can simply be replaced with any kernel function $\mathbf{G}(\omega)$, as long as its influence can be considered small. Generalizing the theory accordingly, leads to the following expressions for damped frequencies and eigenmodes:

$$\alpha_k \approx \frac{i\omega_n G'_{kn}(\omega_n)}{(\omega_n^2 - \omega_k^2)} \quad (5.36)$$

and

$$\bar{\phi}_n \approx \phi_n + i \sum_{k \neq n} \frac{\omega_n G'_{kn}(\omega_n)}{(\omega_n^2 - \omega_k^2)} \phi_k \quad (5.37)$$

Often in viscoelastic systems, besides the number of damped eigenmodes and their conjugates, one or more non-viscous modes arise. These require an extensive procedure to obtain [28, 36] but are usually of limited influence. In CMS it would be an obvious choice to truncate these modes and therefore in general they are not computed at all.

Since Woodhouse' method is approximate and is only accurate for small damping, the circumstances should be verified. A measure for damping is the Q-factor, which should not drop below a value of 10 for this theory to be applicable. For small damping the Q-factor can be computed per mode as:

$$Q \approx \frac{\Re(\bar{\omega}_k)}{2\Im(\bar{\omega}_k)} \quad (5.38)$$

5.3.3 Reduction of Rayleigh's method

In order to save computational time, only a selection of undamped modes are used in the construction of the complex modes. Sensibly, at least all modes up to the highest desired eigenfrequency are included. Thereafter, a truncation has to be made based on the accumulated weight of the inclusion of undamped modes, in a complex mode. Obviously, the inclusion weights are system specific and depend on frequency dependent properties. Equation 5.36 allows for distinguishing the system specific term and a general relation. The latter can be used to base inclusion indications and criteria on. Thus, approaching the system as if continuous, neglecting system specific variations, the modal inclusion weights for construction of the n_{th} mode, can be expressed as:

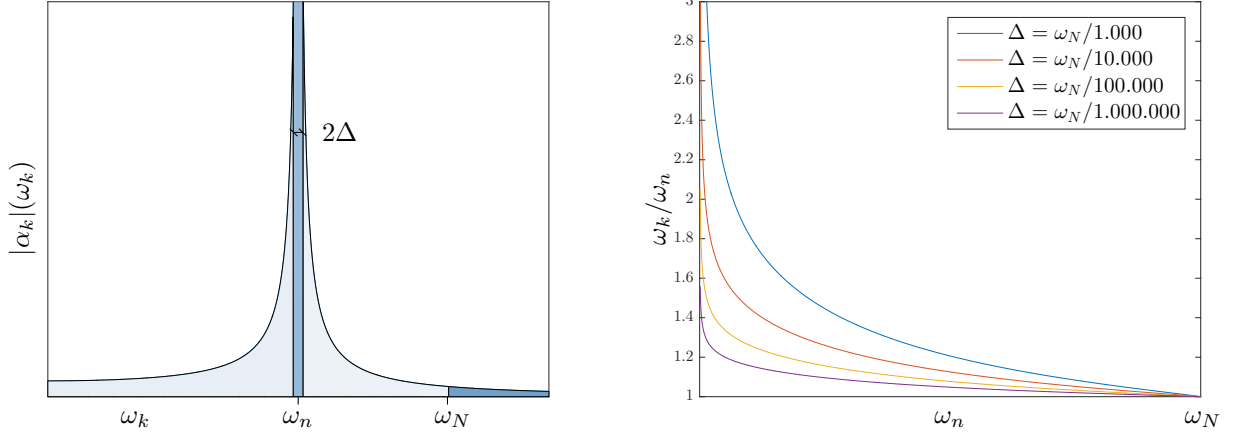
$$\frac{\alpha_k(\omega_k)}{G'_{kn}} \approx \frac{\omega_n}{\omega_n^2 - \omega_k^2} \quad (5.39)$$

By integration, a description for accumulated weight can be derived, considering only absolute values:

$$\frac{\alpha_{k,acc}}{G'_{kn}} \approx \int \left| \frac{\omega_n}{\omega_n^2 - \omega_k^2} \right| d\omega_k = \frac{\ln |\omega_k - \omega_n| - \ln |\omega_k + \omega_n|}{2} \quad (5.40)$$

The problem with this integral is that it does not converge due to its asymptotic property at ω_n and which lies between the essential bounds for any practical options. Besides, it is impossible to consider an infinitely ongoing frequency range to determine the accumulated weight of all possible eigenmodes. Fortunately, these issues can easily be resolved with the fact that in practice, one is dealing with a finite system with highest eigenfrequency ω_N and where α_n is distinguished determined separately (namely to be $\alpha_n = 1$). Working towards discretization, the asymptote is literally cut out, with an offset referred to as Δ , and a top bound at ω_N , as illustrated in figure 5.5. The total accumulated weight can now be expressed as:

$$\frac{\alpha_{N,acc}}{G'_{kn}} \approx \int_0^{\omega_n - \Delta} \frac{\omega_n}{\omega_n^2 - \omega_k^2} d\omega_k - \int_{\omega_n + \Delta}^{\omega_N} \frac{\omega_n}{\omega_n^2 - \omega_k^2} d\omega_k \quad (5.41)$$



(a) Inclusion weight α_k of the k_{th} undamped mode for the n_{th} complex mode (b) Inclusion ratio ω_k/ω_n with various Δ for a relative inclusion weight $p = 0.9$

Figure 5.5: Analytical bases for inclusion weight and inclusion ratio

Using the principals processed in equation 5.41, equation 5.40 can be used to describe the accumulated weight at ω_k as a part of the total, denoted by p . Provided the assumption that system specific factorization is distributed uniformly, or $G'_{ij} = G'_{pq}$ with $i \neq j$ and $p \neq q$, a system independent expression is found:

$$p \triangleq \frac{\alpha_{k,acc}}{\alpha_{N,acc}} \approx \frac{\ln\left(\frac{(2\omega_n - \Delta)(2\omega_n + \Delta)(\omega_k - \omega_n)}{\Delta^2(\omega_k + \omega_n)}\right)}{\ln\left(\frac{(2\omega_n - \Delta)(2\omega_n + \Delta)(\omega_N - \omega_n)}{\Delta^2(\omega_N + \omega_n)}\right)} \quad (5.42)$$

Rearrangement of equation 5.42 enables one to find a value for ω_k where a relative accumulated weight of p is satisfied:

$$\omega_k \approx -\omega_n \frac{\chi + 1}{\chi - 1} \quad (5.43)$$

where:

$$\chi \triangleq (2\omega_n - \Delta)^{p-1} (2\omega_n + \Delta)^{p-1} (\omega_N + \omega_n)^{-p} (\omega_N - \omega_n)^p \Delta^{2-2p} \quad (5.44)$$

As can be seen in figure 5.5, the estimated order of magnitude for Δ and ω_N have significant influence on the accuracy of the approximated inclusion ratio. Without any prior analysis it is difficult to make a proper guess for either values. One is able to make an initial estimation based on the modelled material properties and the amount of DoF involved, but especially in models with unevenly distributed eigenfrequencies, one is prone to make poor estimations.

Instead it is advisable to determine Δ and ω_N based on an essential set of eigenfrequencies, namely all eigenfrequencies up to the frequency of the mode of interest (ω_n) and the one after (ω_{n+1}). Also being the highest of eigenfrequencies, ω_N can be calculated efficiently using power iteration based methods [37]. Now Δ simply follows from adjacent eigenfrequencies of ω_n :

$$\Delta \approx \frac{\omega_{n+1} - \omega_{n-1}}{2} \quad (5.45)$$

With the involved frequencies known, one may choose to distinguish Δ for the left and right side, leading to a more complicated but also more accurate expression for χ in the range $[\omega_2; \omega_{N-1}]$:

$$\chi \approx (\omega_n + \omega_{n-1})^{p-1} (\omega_n + \omega_{n+1})^{p-1} (\omega_N + \omega_n)^{-p} (\omega_N - \omega_n)^p (\omega_n - \omega_{n-1})^{1-p} (\omega_n - \omega_{n+1})^{1-p} \quad (5.46)$$

Though equation 5.43 provides a fair indication of the modal frequencies required, it cannot guarantee the desired inclusion ratio since not all effects of system specific properties are taken into account. Thus for certainty, a criterion is required which includes probabilistic bounds. For the sake of practical consistency, uncertainty should be described as general as possible. The normalized central accumulated weight (NCAW) ($\alpha_{n-1,acc}/\alpha_{N,acc}$, defined through equation 5.40 and 5.41) is such a term and is independent of the desired inclusion rate. Following the same principles as seen previously, it can be defined as:

$$\frac{\alpha_{n-1,acc}}{\alpha_{N,acc}} \approx \frac{\ln\left(\frac{\omega_n + \omega_{n-1}}{\omega_n - \omega_{n-1}}\right)}{\ln\left(\frac{(\omega_n + \omega_{n-1})(\omega_{n+1} + \omega_n)(\omega_N - \omega_n)}{(\omega_n - \omega_{n-1})(\omega_{n+1} - \omega_n)(\omega_N + \omega_n)}\right)} \quad (5.47)$$

Under the condition that sufficiently many samples are provided, a normal distribution is justly assumed using Student's theory. A criterion can now be formulated to guarantee weight inclusion p for the n_{th} mode, including contribution up to the K_{th} undamped mode, with a probability corresponding with reliability index β :

$$\frac{\sum_{k=1}^{n-1} \alpha_k}{\sum_{k=n+1}^K \alpha_k} \leq \frac{p}{p - \frac{\alpha_{n-1,acc}}{\alpha_{N,acc}} + \beta\sigma} \quad (5.48)$$

where σ is the variance of the NCAW, which can be computed for a single model:

$$\sigma = \sqrt{\frac{1}{N-3} \sum_{n=2}^{N-1} \left(\frac{\sum_{k=1}^{n-1} \alpha_k}{\sum_{k \neq n}^N \alpha_k} - \frac{\alpha_{n-1,acc}}{\alpha_{N,acc}} \right)^2} \quad (5.49)$$

where implied dependency is omitted ($\alpha_k = \alpha_k(n)$).

Of course in practice, it would be pointless to statistically examine a model with its own full data set. Instead, a model should be examined with NCAW variance based on a set of benchmark models, ideally categorized if certain model properties appear to be dominant.

Probability of similarities between a benchmarked model and the model to be analysed, is not influenced by the amount of samples a benchmark model provides. Thus treating every sample equally in order to find the variance of the NCAW will bias the result. Rather, the samples are weighted to prevent this bias. Assuming the set of benchmark models to be random variants within its category, the variance of the NCAW can be computed as:

$$\sigma \approx \sqrt{\sum_{m=1}^M \sum_{n=2}^{N-1} \frac{1}{N-2} \left(\frac{\sum_{k=1}^{n-1} \alpha_k}{\sum_{k \neq n}^N \alpha_k} - \frac{\alpha_{(n-1),acc}}{\alpha_{N,acc}} \right)^2} \quad (5.50)$$

where m denotes the model index up to M . Again implied dependencies are omitted ($\alpha_k = \alpha_k(n, m)$, $\alpha_{n,acc} = \alpha_n(m)$), $N = N(m)$.

Because of large variances, it may occur that the mode used to validate (using equation 5.48) is bad representation for its neighbouring modes, leading to either a poor or unnecessarily high inclusion rates, implying

respectively under-performance or increased computational time. To overcome such issues, a multiple validation modes criterion can be used, where the highest mode (\mathcal{N}) to be validated would 'on average' fulfil the prescribed inclusion rate:

$$\sum_{n=1}^{\mathcal{N}} \frac{\sum_{k=1}^{n-1} \alpha_k}{\sum_{k=n+1}^K \alpha_k} \frac{p + b(n, \mathcal{N}) + \beta \frac{\sigma}{\sqrt{\mathcal{N}}} - \frac{\alpha_{n-1, acc}}{\alpha_{\mathcal{N}, acc}}}{\mathcal{N}(p + b(n, \mathcal{N}))} \leq 1 \quad (5.51)$$

Here $b(n, \mathcal{N})$ is a function correcting for the fact that when a relative accumulated weight of p is expected for mode \mathcal{N} , for all lower modes the relative accumulated weight are expected to be higher than p :

$$b(n, \mathcal{N}) \triangleq \frac{h(n, K)}{h(n, \mathcal{N})} - \frac{h(\mathcal{N}, K)}{h(\mathcal{N}, \mathcal{N})} \quad (5.52)$$

with:

$$h(n, k) = \ln \left(\frac{(\omega_n + \omega_{n-1})(\omega_{n+1} + \omega_n)(\omega_k - \omega_n)}{(\omega_n - \omega_{n-1})(\omega_{n+1} - \omega_n)(\omega_k + \omega_n)} \right) \quad (5.53)$$

5.4 Application in CMS

Similar as in chapter 3, a reduction basis is obtained before coupling substructures. Specifically for inclusion of viscoelastic parts, two more methods are presented, where complex modes have a key role.

5.4.1 Modified Craig-Bampton method

In [15], a modification of the Craig-Bampton method is presented, such that the reduction basis takes the influence of any small linear damping into account. This method proposes a basis existing of damped fixed interface vibration modes and quasi-static constraint modes. Computing the damped fixed interface vibration modes as suggested in 5.26 or 5.37 and obtaining the quasi-static constraint modes following subsection 3.2.1 (though inertial terms can be neglected), a reduction basis similar to the classical Craig-Bampton basis is found:

$$\begin{bmatrix} \mathbf{u}_i \\ \mathbf{u}_b \end{bmatrix} \approx \begin{bmatrix} \Re(\bar{\Phi}_i) & \Im(\bar{\Phi}_i) & \hat{\Psi}_c \\ \mathbf{0} & \mathbf{0} & \mathbf{I} \end{bmatrix} \begin{bmatrix} \bar{\eta}_i^{re} \\ \bar{\eta}_i^{im} \\ \mathbf{u}_b \end{bmatrix} = \mathbf{R}_{MCB} \boldsymbol{\eta}_{MCB} \quad (5.54)$$

Kuether suggests to include the imaginary parts of the modes separately to restrict solutions in the physical domain to be purely real. This doubles the size of the reduction basis, but adds versatility as viscoelastic forces are included and more options for truncation are provided. In the frequency domain though, this is not required and the latter action remains optional.

Though in [15] a modal interface reduction is proposed, the Modified Craig-Bampton also allows use of OPS interface reduction as described in section 4.4. Shown by Kuether that the imaginary parts of the interface modes are of negligible influence, no adjustments have to be made in the interface reduction.

5.4.2 Ding's method

For dealing with linear damped systems, Ding presents an alternative to the Modified Craig-Bampton with a free interface method [16]. Similar as for Rubin's and MacNeal's method, a reduction basis is constructed with free interface vibrations modes, enriched with residual attachment modes. As one may suspect, again the vibration modes are computed under damped circumstances and therefore become complex in general.

Also obtaining the residual attachment modes requires a different approach than suggested in subsection 3.2.3. Working through the Laplace domain, the dynamic response can be expressed as [38]:

$$\mathbf{u}(s) = \sum_{j=1}^m \frac{\phi_j^T \phi_j}{\theta_j(s - \lambda_j)} \mathbf{f}(s) \quad (5.55)$$

where

$$\theta_j \triangleq \phi_j^T \left(2\lambda_j \mathbf{M} + \mathbf{G}(\lambda_j) + \lambda_j \frac{\partial \mathbf{G}(s)}{\partial s} \Big|_{s=\lambda_j} \right) \phi_j \quad (5.56)$$

Equation 5.55 is then rewritten to matrix form:

$$\mathbf{u}(s) = -\Phi \Theta^{-1} (\Lambda - s\mathbf{I})^{-1} \Phi^T \mathbf{f}(s) \quad (5.57)$$

where

$$\Lambda \triangleq \text{diag}[\lambda_1, \lambda_2, \dots, \lambda_m], \Theta \triangleq \text{diag}[\theta_1, \theta_2, \dots, \theta_m]$$

Through further workout of equation 5.57 following [16], the residual flexibility matrix is expressed in terms of the retained vibration modes, evaluated halfway maximum frequency of interest, ω_s :

$$\mathbf{G}_r = (\mathbf{K} + i\omega_s \mathbf{G}(i\omega_s) - \omega_s^2 \mathbf{M})^{-1} + \Phi_{ret} \Theta_{ret}^{-1} (\Lambda_{ret} - i\omega_s \mathbf{I})^{-1} \Phi_{ret}^T \quad (5.58)$$

Note that in [16], the residual flexibility matrix is taken to be the full set of residual attachment modes. Of course, since the purpose is to comprise as much relevant information in modes corresponding with boundary DoF, the resulting set of modes is again filtered with using a localization matrix:

$$\Psi_d \triangleq \mathbf{G}_r \mathbf{A}^T \quad (5.59)$$

Again ω_s is a supportive frequency parameter, which in this case is advised to be valued as the centre of the frequency range of interest.

Having obtained all modes for the reduction basis, the first transformational equation can be written, here not only the DoF partitioned but also the inserted modes, as this will be useful later:

$$\begin{bmatrix} \mathbf{u}_i \\ \mathbf{u}_b \end{bmatrix} = \begin{bmatrix} \Phi_{f|i} & \Psi_{d|i} \\ \Phi_{f|b} & \Psi_{d|b} \end{bmatrix} \begin{bmatrix} \eta_f \\ \mathbf{g}_b \end{bmatrix} \quad (5.60)$$

Considering equilibrium of interface forces at a global level, the interface forces can be eliminated through an additional two transformation matrices:

$$\begin{bmatrix} \eta_f^A \\ \mathbf{g}_b^A \\ \eta_f^B \\ \mathbf{g}_b^B \end{bmatrix} = \begin{bmatrix} \mathbf{I} & \mathbf{0} & \mathbf{0} \\ \mathbf{0} & \mathbf{0} & \mathbf{I} \\ \mathbf{0} & \mathbf{I} & \mathbf{0} \\ \mathbf{0} & \mathbf{0} & -\mathbf{I} \end{bmatrix} \begin{bmatrix} \eta_f^A \\ \eta_f^B \\ \mathbf{g}_b^A \end{bmatrix} = \begin{bmatrix} \mathbf{I} & \mathbf{0} & \mathbf{0} \\ \mathbf{0} & \mathbf{0} & \mathbf{I} \\ \mathbf{0} & \mathbf{I} & \mathbf{0} \\ \mathbf{0} & \mathbf{0} & -\mathbf{I} \end{bmatrix} \begin{bmatrix} \mathbf{I} \\ \mathbf{L}_d^{-1} \mathbf{L}_f \end{bmatrix} \begin{bmatrix} \eta_f^A \\ \eta_f^B \end{bmatrix} = \mathbf{T}_1 \mathbf{T}_2 \begin{bmatrix} \eta_f^A \\ \eta_f^B \end{bmatrix} \quad (5.61)$$

where

$$\mathbf{L}_d \triangleq \Psi_{d|b}^A + \Psi_{d|b}^B, \mathbf{L}_f \triangleq -\Phi_{f|b}^A \Phi_{f|b}^B, \mathbf{T}_1 \triangleq \begin{bmatrix} \mathbf{I} & \mathbf{0} & \mathbf{0} \\ \mathbf{0} & \mathbf{0} & \mathbf{I} \\ \mathbf{0} & \mathbf{I} & \mathbf{0} \\ \mathbf{0} & \mathbf{0} & -\mathbf{I} \end{bmatrix}, \mathbf{T}_2 \triangleq \begin{bmatrix} \mathbf{I} \\ \mathbf{L}_d^{-1} \mathbf{L}_f \end{bmatrix}$$

The procedure as described here can be expanded to take into account more than 2 substructures sharing an interface. Also additional interface stiffness or damping as in subsection 2.5.1 will require alteration of the method. Since boundary DoF are completely eliminated in the reduced system, no additional interface reduction has to be applied. It would be optional though to transform interface forces to interface displacements and apply OPS reduction afterwards.

Chapter 6

Error evaluation

In order to evaluate results found, the reduced order models are compared with their full order alternatives. To gain insight in differences, several error quantifications are briefly introduced in this chapter, each covering different aspects of the nature of differences.

Model Assurance Criterion

Though the Model Assurance Criterion (MAC) has limited use in this research, it is widely used and forms the base of many other criteria such as the Frequency Response Assurance Criterion. The MAC is a correlation measurements between modes. Especially in experimental dynamics, MAC is useful to verify consistency between modes measured, or modes obtained from a model [39]. Ranging from 0 to 1, the MAC between the j_{th} and the k_{th} mode is defined as:

$$MAC(\phi_j, \phi_k) \triangleq \frac{|\phi_j^T \phi_k^*|^2}{\phi_j^T \phi_j^* \phi_k^T \phi_k^*} \quad (6.1)$$

Frequency Response Assurance Criterion

Similar as the MAC, the Frequency Response Assurance Criterion (FRAC) evaluates correlation between FRF over a chosen frequency range. This can be used to quantify of resemblance between FRF of a reduced model compared to FRF of a full or exact model, or even experimental results. Due to FRAC being based on minimization of squared error between vector spaces, the criterion is very insensitive to small values while being over-sensitive for large ones. Taking this fact into account, and carefully bounding the frequency range of interest, FRAC is an effective tool for verifying the qualitative behaviour of a structure, rather than quantitative. In other words, high FRAC values indicate high usability of reduced order model in conceptual studies, but not necessarily for normative calculations. The FRAC between the examined FRF Y_j and its reference solution Y_k is computed as:

$$FRAC(Y_j, Y_k) \triangleq \frac{|Y_j^T Y_k^*|^2}{Y_j^T Y_j^* Y_k^T Y_k^*} \quad (6.2)$$

Root Mean Square Error

The two perhaps most common error quantifications are the Root Mean Square Error (RMSE) and the Mean Absolute Error. Similar as for the MAC, RMSE emphasizes large errors rather than small ones. This may be of use for tests where outliers are particularly unacceptable. One may notice that the RMSE corresponds with standard deviation with respect to the references values, thus being suitable for further statistical processing. The general formulation of the RMSE with n sample values is as follows:

$$RMSE \triangleq \sqrt{\frac{1}{n} \sum_{j=1}^n (y_j - \hat{y}_j)^2} \quad (6.3)$$

where y_j contains the measurements to be compared with assumed true values \hat{y}_j .

Mean Absolute Error

If the aforementioned aspects do not apply, the Mean Absolute Error may be of better use. It is a straightforward measurement where errors weigh equally, thus suitable for cases where errors have proportional impact on the quality of an analysis. Using the same notation as for the RMSE, the MAE is formulated as:

$$MAE \triangleq \frac{1}{n} \sum_{j=1}^n |y_j - \hat{y}_j| \quad (6.4)$$

Relative and Normalized Errors

In many contexts neither RMSE and MAE will provide insight without a frame of reference. The absolute error can be taken relative to the true values, normalized to a meaningful quantity or a combination of both. Let the Mean Relative Error (MRE) be defined as:

$$MRE \triangleq \frac{1}{n} \sum_{j=1}^n \frac{|y_j - \hat{y}_j|}{|\hat{y}_j|} \quad (6.5)$$

Let the Mean Normalized Relative Error (MNRE) be the error normalized to the sum of the absolute error and the absolute reference value, such that the result always ranges between 0 and 1:

$$MNRE \triangleq \frac{1}{n} \sum_{j=1}^n \frac{|y_j - \hat{y}_j|}{|\hat{y}_j| + |y_j - \hat{y}_j|} \quad (6.6)$$

Let the Mean Normalized Absolute Error be (MNAE):

$$MNAE \triangleq \frac{1}{n} \sum_{j=1}^n \frac{|y_j - \hat{y}_j|}{|\bar{y}|} \quad (6.7)$$

where \bar{y} is a fixed reference value such as the maximum measured error or an upper error bound.

Part II

Verification

Chapter 7

Testing procedure

In order to validate the value of presented theories, a series of tests is carried out. Reduced order analyses are performed along full order alternatives, which provide the optimal reference solutions. Finite element models have been constructed using the Abaqus software package, one that allows for many manual modelling options.

For this research a tool has been developed in Matlab allowing for reduced order analysis and the procedures prior to it: reduction and assembly. Lastly, analysis results are processed into any desired output options using several Matlab routines, also specifically developed for this research.

This chapter elaborates on the testing process and aims to clarify on how the theory is shaped into a practical framework in order to enable a consistent procedure. The main workflow is presented in figure 7.1.

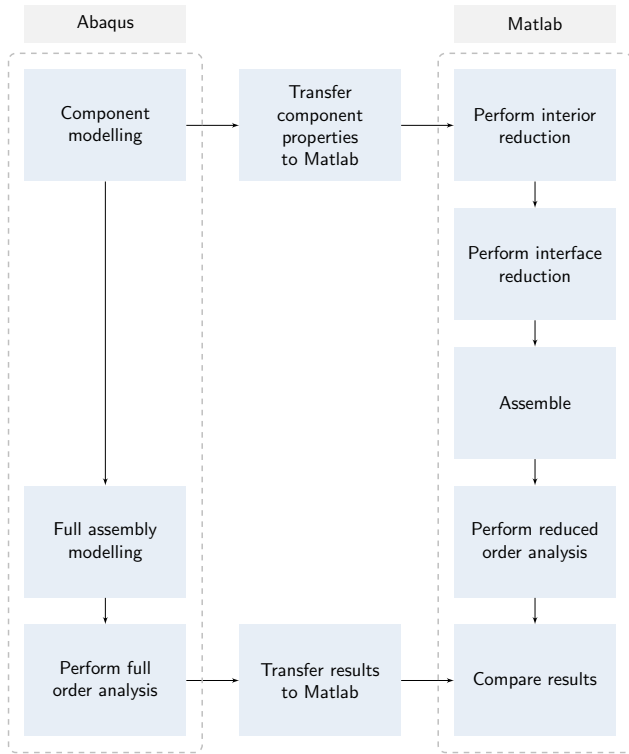


Figure 7.1: Research workflow

7.1 Finite Element Modelling

Components are modelled both individually, as well as in an assembled state with the use of Abaqus. While the fully assembled model can be put directly into analysis, the component models are prepared for use in Matlab. Abaqus provides stiffness, damping and mass matrices, accompanied with nodal and element information (coordinates and numbering). Most other input options, such as interface/boundary conditions, reduction base parameters and damping, are submitted manually in the Matlab tool, enabling the user to experiment with options flexibly and fast. For commercial use, most input options can easily be transferred from data files as well, enabling the user to do most of the modelling in a graphical, user-friendly environment (see figure 7.2). Obviously, interfaces require prior definition for fixed interface reduction methods.

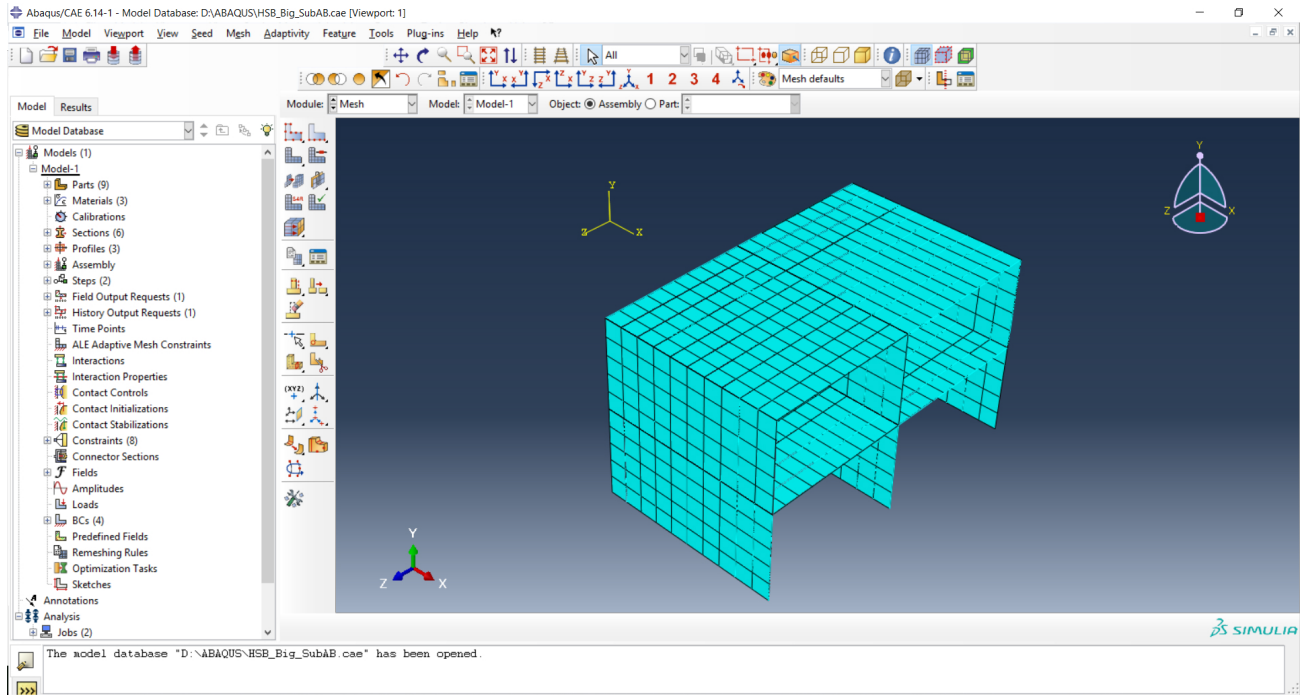


Figure 7.2: A building component in the Abaqus modelling environment

Damping models can both be provided through Abaqus, or manually in Matlab. For frequency dependent damping matrices, it is important to be consistent in the frequency range discretization in Abaqus and Matlab, or to correct for differences using interpolation. Figure 7.3 provides an overview of how the Matlab component model is obtained.

7.2 Component reduction

Having obtained all component model data in Matlab format, the tool allows for reduction methods to be applied. Essential for reduction is either partitioning or labelling of DoF according to the principle of equation 3.3. Since the tool features separate processing of Dirichlet boundary conditions, the DoF facing such condition enforcement are categorized in a third partition, preparing them for elimination. Note that in the case that multiple substructure interfaces are being coupled, proper processing requires subpartitioning/sublabelling of interface DoF to ensure that each interface gains a reduction basis independent of each other. Besides, it allows for interfaces to easily be coupled to the correct substructures.

Based on the priorly defined modal truncation number or frequency, the necessary eigenmodes are computed.

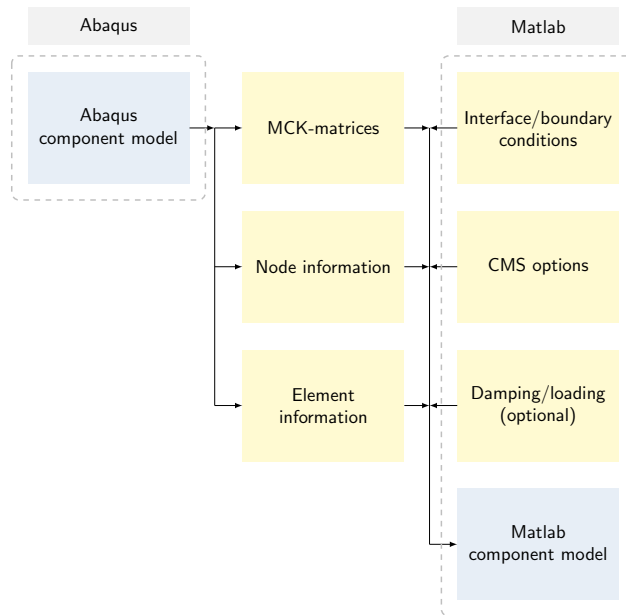


Figure 7.3: Creating the Matlab component model

For Modified Craig-Bampton or Ding reduction (section 5.4) the procedure described in section 5.3 is followed. After having computed the (quasi-) static set of modes pertaining to the corresponding reduction method, the interior reduction matrix is cast.

OPS projection

Next, the OPS interface reduction is prepared. The original polynomial series are projected onto the interfaces using linear mapping through the coordinates. To prevent coupling to occur 'inside out' (see figure 7.4), matching control points are defined at each substructure.

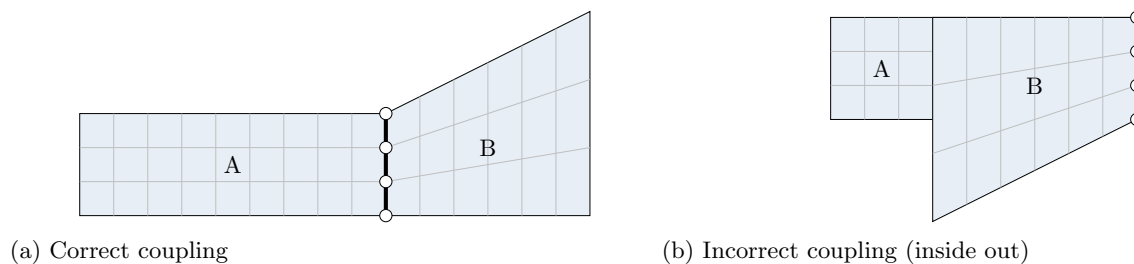


Figure 7.4: Examples of correct and incorrect coupling of two substructures

In case of curved interfaces, one can either project the polynomial series onto a straight 'virtual line' linearly, or also using increased order polynomials (thus both the interface geometry as motion are described using polynomial series). In general, the latter also comes down to a virtual interface shape, instead of a physical one, but the projection is optimized through making a least squares fit. A more physical resembling interface should not be assumed to result in a more accurate interface reduction basis. The performance with increased order mapping requires additional research, which is not covered in this thesis.

On linear mapping...

Linear mapping can be performed by predetermining coordinate relations between the edge nodes of the boundary in consideration and the edges of the function domain of the OPS used. Due to redundant information, a linear polynomial can be suggested as a function of any physical coordinate. Thus for a modelling space spanning in x and y directions, the natural coordinates ξ (of the OPS functions) can be assumed as:

$$\xi = c_1 + c_2\mathbf{x} \text{ or } \xi = c_3 + c_4\mathbf{y} \quad (7.1)$$

where $c_1 \dots c_4$ are constants to be solved.

The choice of which physical coordinate variable is arbitrary as long as the considered boundary is not orthogonal to its axis. Thus a boundary that is parallel to the x -axis cannot be mapped using its y -coordinates and vice versa.

Given the x -coordinates of both boundary edges, $x_{edge,1}$ and $x_{edge,2}$, and their corresponding natural coordinates, $\xi_{edge,1} = -1$ and $\xi_{edge,2} = 1$, a linear system of equation can be established to solve for c_1 and c_2 :

$$\begin{bmatrix} 1 & x_{edge,1} \\ 1 & x_{edge,2} \end{bmatrix} \begin{bmatrix} c_1 \\ c_2 \end{bmatrix} = \begin{bmatrix} -1 \\ 1 \end{bmatrix} \quad (7.2)$$

Thus by obtaining the c_1 and c_2 from equation 7.2, the natural coordinates of all boundary nodes can be found using 7.1, enabling for evaluating their corresponding OPS function values.

Relating translation to rotation

Having mapped the Legendre or Fourier series, their mapped descriptions are inserted in the interface reduction matrix. The relations between different translational directions of motion are usually not easily estimated a priori, thus different directions are described by a separate basis. Rotational motion on the contrary, can be associated with translational motion at interfaces that are insensitive to shear deformation. Rotation is therefore easily integrated with the corresponding translational direction using the derivative with respect to it. The modal description of a straight interface in x -direction, with 3 directions of translational DoF (x, y, z) and 3 directions of rotational DoF ($\theta_x, \theta_y, \theta_z$) would become:

$$\begin{bmatrix} \mathbf{u}_b^{(x)} \\ \mathbf{u}_b^{(y)} \\ \mathbf{u}_b^{(z)} \\ \mathbf{u}_b^{(\theta_x)} \\ \mathbf{u}_b^{(\theta_y)} \\ \mathbf{u}_b^{(\theta_z)} \end{bmatrix} = \begin{bmatrix} \mathbf{P}_0 & \mathbf{0} & \mathbf{0} & \mathbf{0} & \dots & \mathbf{P}_n & \mathbf{0} & \mathbf{0} & \mathbf{0} \\ \mathbf{0} & \mathbf{P}_0 & \mathbf{0} & \mathbf{0} & \dots & \mathbf{0} & \mathbf{P}_n & \mathbf{0} & \mathbf{0} \\ \mathbf{0} & \mathbf{0} & \mathbf{P}_0 & \mathbf{0} & \dots & \mathbf{0} & \mathbf{0} & \mathbf{P}_n & \mathbf{0} \\ \mathbf{0} & \mathbf{0} & \mathbf{0} & \mathbf{P}_0 & \dots & \mathbf{0} & \mathbf{0} & \mathbf{0} & \mathbf{P}_n \\ \mathbf{0} & \mathbf{0} & \frac{d\mathbf{P}_0}{dx} & \mathbf{0} & \dots & \mathbf{0} & \mathbf{0} & \frac{d\mathbf{P}_n}{dx} & \mathbf{0} \\ \mathbf{0} & \frac{d\mathbf{P}_0}{dx} & \mathbf{0} & \mathbf{0} & \dots & \mathbf{0} & \frac{d\mathbf{P}_n}{dx} & \mathbf{0} & \mathbf{0} \end{bmatrix} \begin{bmatrix} \eta_0^{(x)} \\ \eta_0^{(y)} \\ \eta_0^{(z)} \\ \eta_0^{(\theta_x)} \\ \vdots \\ \eta_n^{(x)} \\ \eta_n^{(y)} \\ \eta_n^{(z)} \\ \eta_n^{(\theta_x)} \end{bmatrix} \quad (7.3)$$

such that \mathbf{P}_j is a vector containing the polynomial term with the j_{th} order (see section 4.4), that are evaluated at the natural spatial x coordinates of the corresponding nodes. The full shape over the full physical system coordinates is described by its column, and has an amplitude of $\eta_{\mathbf{P}_j}^x$ for x oriented motion etc.

The reduction process is schematically displayed in figure 7.5.

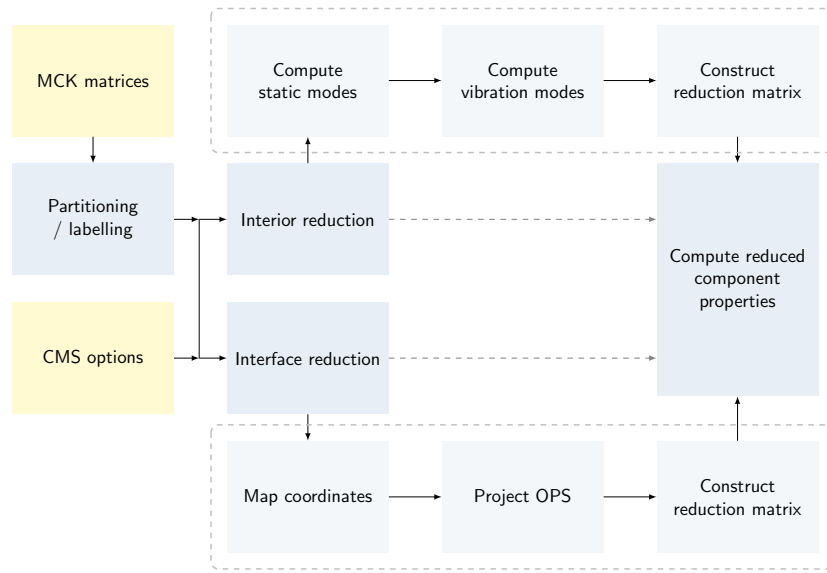


Figure 7.5: Component reduction process

7.3 Assembly

Having obtained the reduced component properties, boundary and interface conditions are prepared following the principles of equations 2.3, 2.10 and 2.30. Note that three different types of Boolean matrices are constructed, one containing conditions pertaining to flexibly connected boundaries (\mathbf{B}_f), one describing rigid connections (\mathbf{B}_r) and one enforcing Dirichlet boundary conditions (\mathbf{B}_c). The latter two are combined and processed through the same primal coupling. Due to the different nature of flexibly connected boundaries, their coupling is performed in a separate procedural step referred to as 'precoupling'. Though the order of the precoupling and regular coupling can be changed, it is convenient to have done all coupling before executing the transition from stiffness to flexibility description. This prevents assemblies without rigid body modes from having to cope with component rigid body modes before the dynamic stiffness can be inverted. An overview of the assembly process is displayed in figure 7.6.

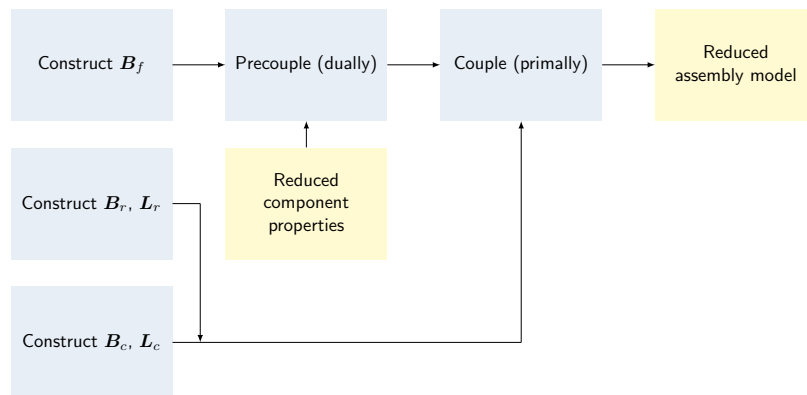


Figure 7.6: Assembly process

7.4 Spectral analysis

When one is solely interested in FRF's, only one step remains, namely returning the reduced solution to physical domain. If one is rather interested in the dynamic response to a load case, some additional steps are followed. When dealing with a load defined in the time domain, a Fast Fourier Transformation is performed. When the frequency domain description of the load is known, the load is transformed to the reduced domain, using the same reduction and localization matrices used for the MCK-matrices. The frequency domain response is simply found by matrix multiplication of the FRF matrices and the reduced load vectors. For a time domain response an Inverse Fast Fourier Transformation is applied to the response vectors. Ultimately, the response is returned from the reduced to the physical domain. The process of finding the desired response with various input and output options is displayed in figure 7.7

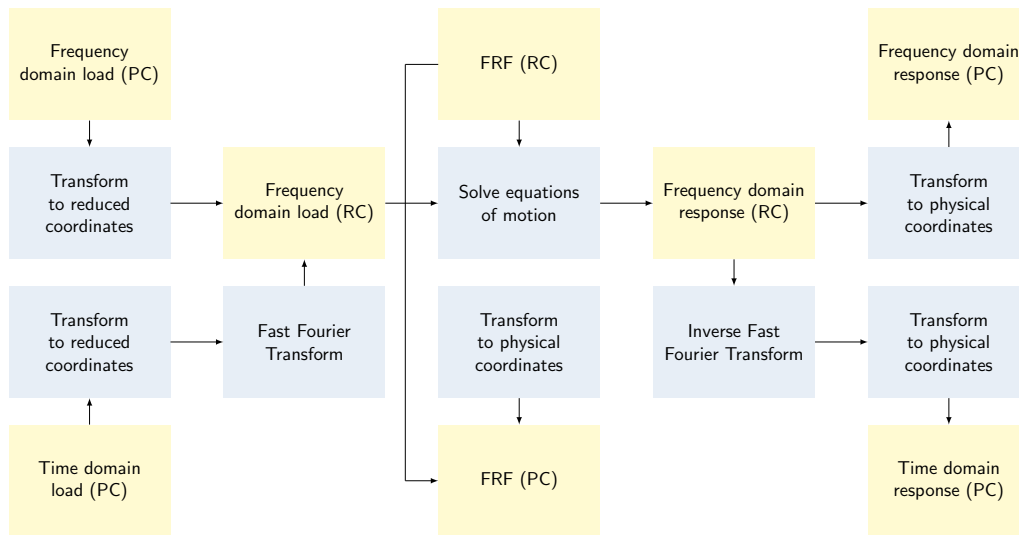


Figure 7.7: Finding a physical response. Abbreviations: Physical Coordinates (PC), Reduced Coordinates (RC)

The full order analysis is performed in Abaqus. The analysis strategy characterized as 'direct dynamic analysis', is similar to the reduced order analysis in Matlab. The principles are the same but more restricted. FRF are computed from the physical system properties. Input is requested in the frequency domain, and as such is the output returned as well. Thus transitions between time and frequency domain are left to the user.

7.5 Post-processing and comparison

Having obtained response data from both full order analysis, as well as their reduced order alternatives, comparison can be made. In this research, comparison is mostly based on FRF, as they clearly show characteristics of the structure. Thus error analysis is also mostly FRF based. Referring back to chapter 6, where error definitions are presented, FRAC values are obtained to support visual FRF comparison in order to secure qualitative performance. For quantitative comparison, MNRE or MNAE values are computed depending on the DoF in consideration. Furthermore, the FRF provide a basis for many other output options, such as interface displacement fields, modal amplitudes or time domain responses.

Chapter 8

Principal test cases and results

This chapter presents a series of basic test cases which serve to investigate the conceptual value of the theories involved. Over the test series, complexity of damping and stiffness properties are increased. The main focus is to research after the effectiveness of OPS interface reduction. Test cases are examined, starting with a case using basic rigid compatibility (using section 2.1), followed by one with flexibly connected substructures (using section 2.5). Hereafter, a Generalized Maxwell model is projected on the interface such that damping and stiffness properties vary over time/frequency.

Also viscoelasticity within substructures is investigated, where overall performance and comparison between standard Craig-Bampton and Modified Craig-Bampton are emphasized.

The base model

As the level of detail of a material model is a sensible engineering consideration, it is also of interest to see the results of the test cases in relation to each. For this reason, one model is chosen as a base case to which the mentioned options can be implemented. The base model consists of two substructures of which both are modelled to be in-plane steel plates using 4-noded plane stress elements. Substructure *A* is a square plate of 1 m by 1 m that is clamped on the left-hand-side. Substructure *B* is a symmetrically tapered plate, with a width of 1 m on the left-hand-side, which is to be connected to substructure *A*, increasing to a width of 2 m at the right-hand-side, after crossing its depth of 1 m. Both plates have a thickness of 2 mm and are meshed evenly along their sides with a 15×15 mesh. Buckling effects are not taken into account, in order for the analysis to remain linear. Element and material properties are summarized in table 8.1.

Element properties	
Element type	4-noded quadrilateral, plane stress
Integration points	2×2
Mass matrix	Lumped
Material & cross-sectional properties	
Young's modulus	210 GPa ²
Density	7840 kg/m ³
Poisson ratio	0.3
Thickness	2 mm

Table 8.1: Element and material properties of the base model

The taper in substructure *B* is chosen to prevent the stiffnesses of both substructures to be too similar. If the latter would be the case, interface modes of the assembled structures will be very similar to interface modes of

the separate substructures. In order to enable generalization of OPS theory, the interface dynamics of the assembly should be explicitly dependent on all substructures involved. Allowing too large differences in substructure stiffnesses will result in one substructure being overly dominant in the behaviour of the assembly, resulting in idealized settings. To prevent testing in either of the idealized cases (too similar or too different stiffnesses), the taper is added to substructure B .

An illustration of the base case is displayed in figure 8.1.

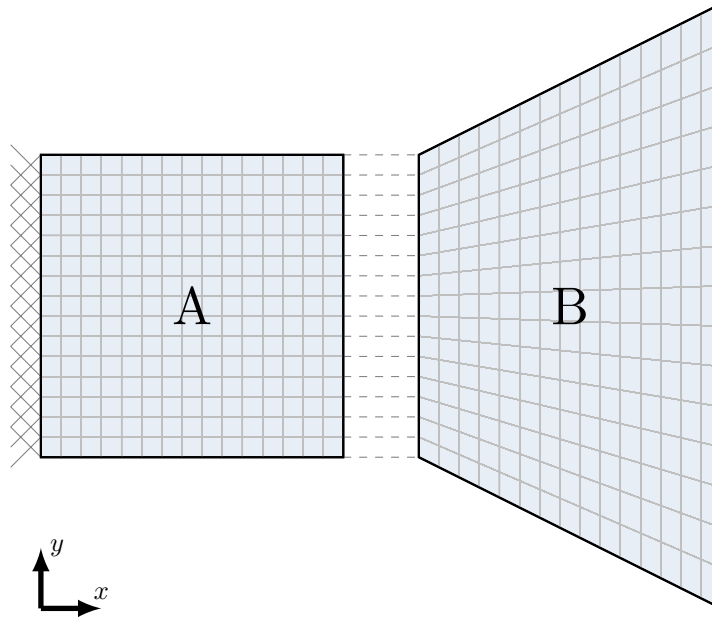


Figure 8.1: The base test case consisting of two plane stress substructures, A and B

The following altered models are created as means of investigating the effects of their characteristics:

- Undamped, rigidly connected plates
- Proportionally damped, rigidly connected plates
- Proportionally damped, flexibly connected plates
- Proportionally damped, viscoelastically connected plates
- Viscoelastic, rigidly connected plates
 - With proportional viscoelastic properties
 - With disproportional viscoelastic properties

8.1 Undamped, rigidly connected plates

In order to gain a general sense for OPS performance, the test case is kept as basic as possible, i.e. the substructures are rigidly connected and no damping is yet considered. First a Craig Bampton interior reduction is performed, retaining 40 fixed interface modes per substructure. This amount covers a vast frequency range in which reliable results are to be expected over the chosen range of interest. To safeguard the validity of the results to be as wide as practically possible, the range of interest is chosen based on the decay in amplitudes of FRF, rather than defining an arbitrary load spectrum. This has resulted in frequency range of 0-3000 Hz. Secondly, an OPS reduction is performed using both Legendre and Fourier series of various orders.

Results analysed are limited to FRF based information from a single load point (chosen to be the upper right corner of substructure B), to all interface DoF. The coupled test case, with reference nodes highlighted, is displayed in figure 8.2.

Numerous goals are attempted to be achieved with the case considered, regarding qualitative and quantitative performance, as well as reliability. With respect to the latter, it is both expected and essential for results to converge over extension of the reduction bases. Convergence is verified visually by plotting FRF for various orders of reduction and is confirmed using MNAE and MaxNAE measurements. Qualitative performance is understood as the amount of resemblance of practical reduced model results compared to its optimal reference. Emphasized is the plotted FRF, which may provide quick insight for conceptual studies. Especially important is that resonance peaks are located correctly and that no ongoing under- or overestimations of FRF values occur. Complementary, a measurement for qualitative performance is sought in FRAC computation. Quantitative performance itself is described through MNAE and MaxNAE measurements, of which the latter also confirms reliability.

An additional goal is obtaining a first indication of relative performance between Legendre and Fourier bases, by comparison.

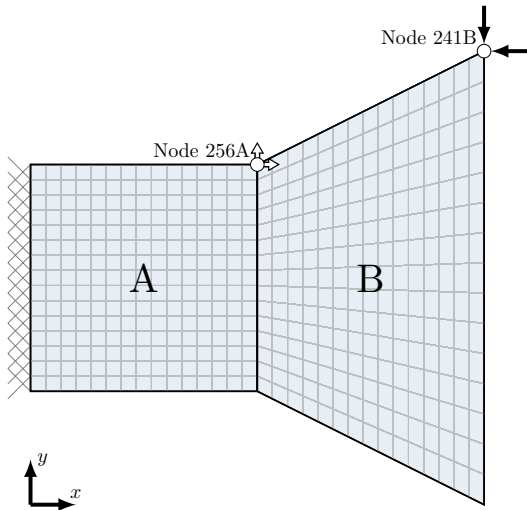


Figure 8.2: Two rigidly connected substructures, A and B

8.1.1 Results

To keep differences in results between OPS orders as visual as possible, a lower order range is chosen for a first analysis step. Figure 8.3 shows an FRF of increasing order reduction bases with reference solutions between the DoF depicted in figure 8.2. An intermediate check by comparing the DS full model with the Abaqus model has been done, but is omitted for overview. Note that a first order Legendre basis is identical to rigidified interface basis as described in section 4.1, thus posing another useful reference solution.

Though only low order Legendre bases are used, differences in the FRF of figure 8.3 are too subtle to grant an ideal overview. On the other hand this is a sign of promising potential. Still, the figure shows rapidly improving qualitative characteristics: with the rigidified interface solution (1 Legendre) some serious misestimates emerge, depicted by misplaced resonance and antiresonance frequencies in the higher frequency range. Consequently, the frequency areas around the mislocated peaks and the correct peaks are affected with significant over- and under-

estimates, posing a threat for even conceptual model analysis. While an additional polynomial term (2 Legendre) already resolves major misestimates, with 3th order Legendre all qualitative flaws appear to be removed.

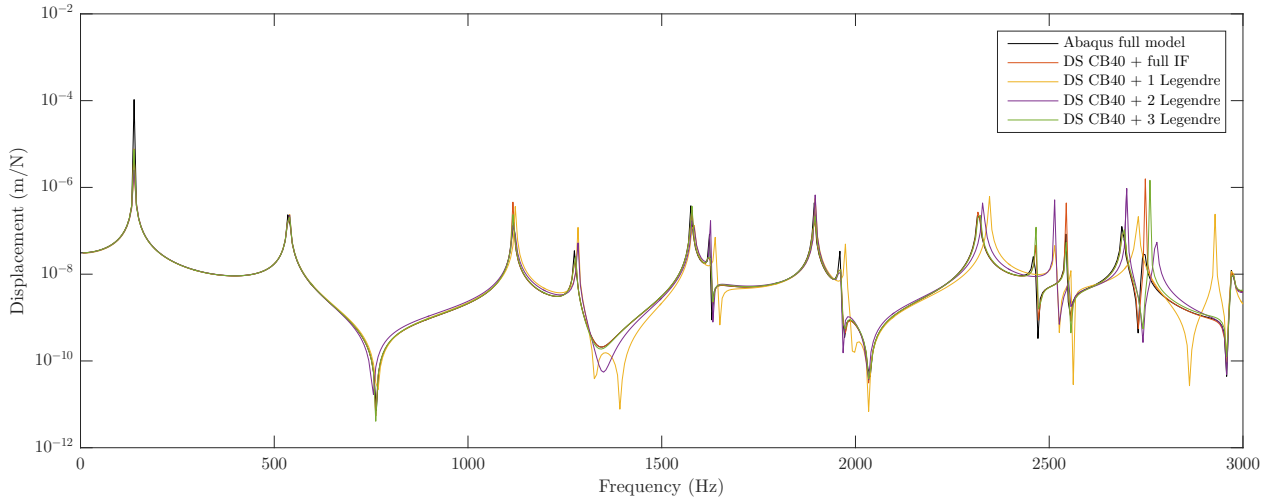
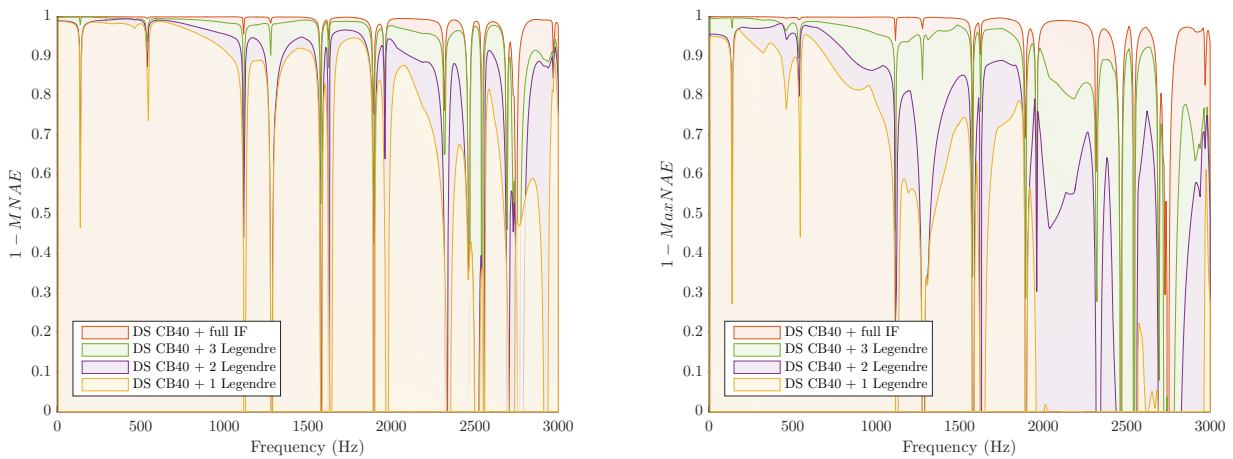


Figure 8.3: FRF node 241B(y) to node 256A(y)

Proceeding to a more quantitative evaluation, errors are computed along the interface and are normalized with the maximum absolute reference displacement at the interface in the corresponding direction. Figure 8.4 confirms convergence, but shows a clear issue around resonance peaks. From an analytical perspective, the peaks should tend to infinity, a property that practically cannot be contained in numerical models. As a result, amplitudes are extremely sensitive to frequency sampling, thus also to small misestimates of resonance frequencies. Due to the importance of accurate resonance information, the results are of limited value. A more realistic option is to add damping to the system, which is covered in the next section. A more extensive evaluation is enabled and elaborated there.



(a) 1– Mean Normalized Absolute Error

(b) 1– Maximum Normalized Absolute Error

Figure 8.4: Error measurement of the test model using various orders of Legendre reduction bases

8.2 Proportionally damped, rigidly connected plates

Since damping is an inevitable phenomenon, it is only sensible to take into account, while resolving the prior issue of overly sensitive frequency area's. In many building analyses, a modal damping model is used for which 5% is a common value. For implementational benefit, a Rayleigh damping model is used, such that a 5% modal damping over the frequency range of interest is approximated. Referring to equation 5.1, the weighing constants have been determined as $\alpha_1 = 60$ and $\alpha_2 = 0.00001$. The model visualization of figure 8.2 remains adequate to represent the damped case.

The actual eigenmode shapes of the full assembly remain unaltered by the proportional damping, to which the accuracy of the Craig-Bampton basis can be expected to be unaffected. An evaluation is done similar as in section 8.1. With the expectation of more justly quantifiable results, the supposed aspects are treated as well, to reach more thorough conclusions. This includes comparison between performance of Legendre and Fourier series.

8.2.1 Results

As expected, figure 8.5 shows clear improvement on estimating resonance frequencies with respect to the undamped case. Results appear to converge, which is confirmed by figure 8.6. Now that errors measurements are meaningful over the whole frequency range, resonance and antiresonance frequencies still appear to be sensitive.

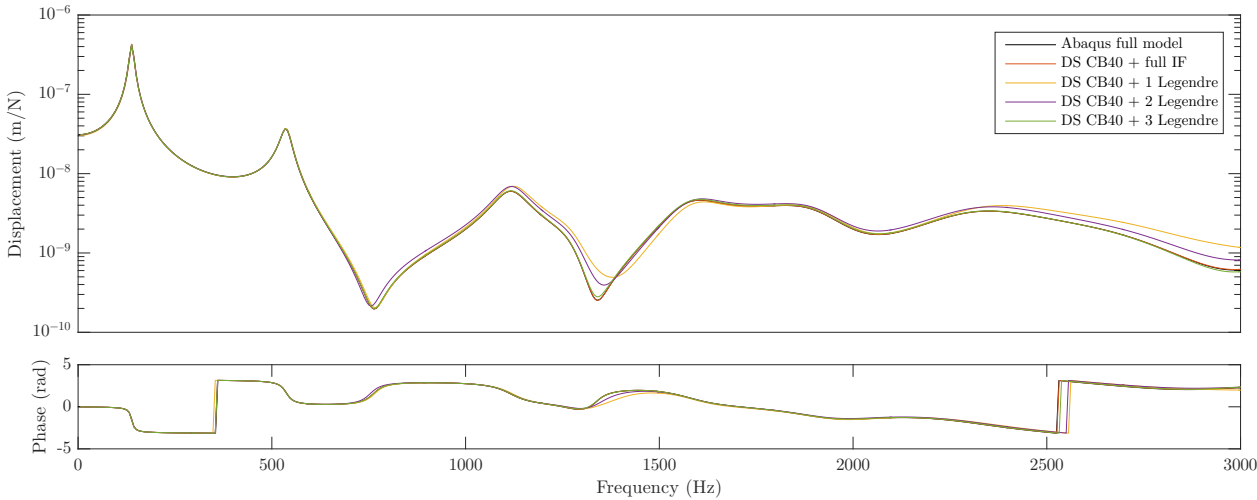
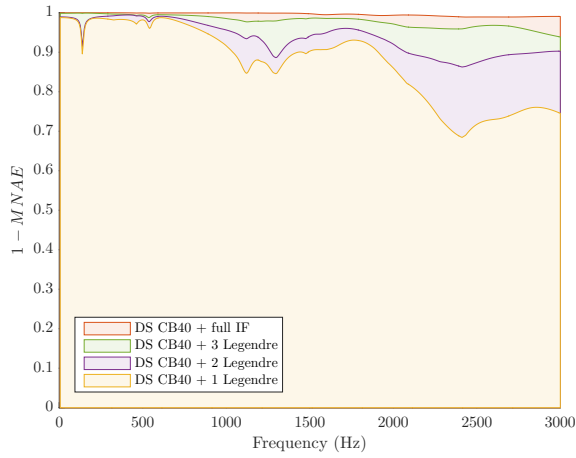


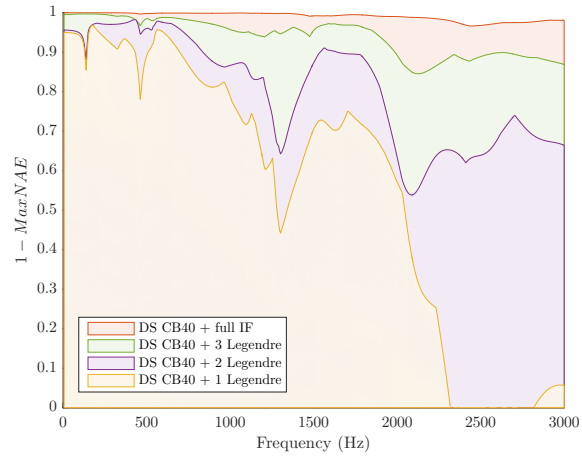
Figure 8.5: FRF node 241B(y) to node 256A(y)

One of the extreme errors is found around the antiresonance frequency of 1300 Hz, which is the largest in x -direction, while the forcing is also x -directed. The interface displacement field at 1300 Hz is displayed in figure 8.7, together with a reference at 1650 Hz, a resonance frequency, showing good results in particular.

Noteworthy is the difference in spatial frequency (addressing harmonic resemblance) along the interface. Generally, the resulting spatial frequencies increase with temporal frequency, though the opposite is observed with the examined displacement fields. Since the interface is only a part of the structure analysed, these appearances are of physical sense. A more visual analogy can be made with a free-free Euler-Bernoulli beam. First consider the displacement field globally. For increasing eigenmode frequencies, each mode gains a local maximum with respect to the previous one. Now consider an infinitesimally small part, exactly halfway of the beam. The presence of local maxima will alternate per increasing mode frequency. Though less obvious, a similar appearance



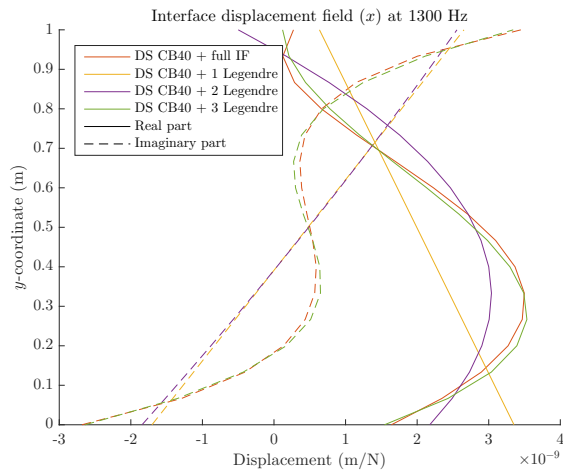
(a) 1– Mean Normalized Absolute Error



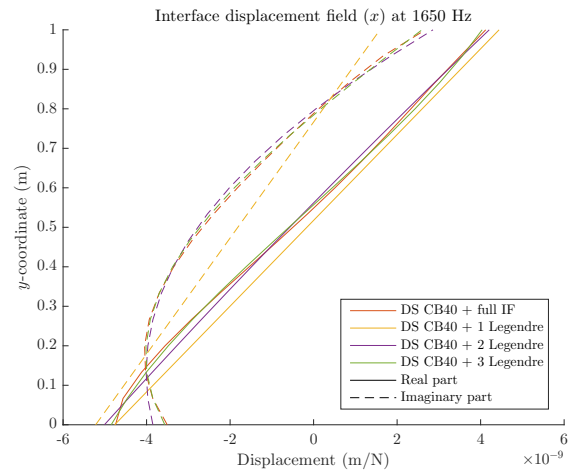
(b) 1– Maximum Normalized Absolute Error

Figure 8.6: Error measurement of the test model using various orders of Legendre reduction bases

occurs with the test case. As a result, the displacement field at 1300 Hz requires a higher order polynomial as for 1650 Hz for an accurate solution, explaining the error peak at 1300 Hz.



(a) Interface displacement field (x) at 1300 Hz



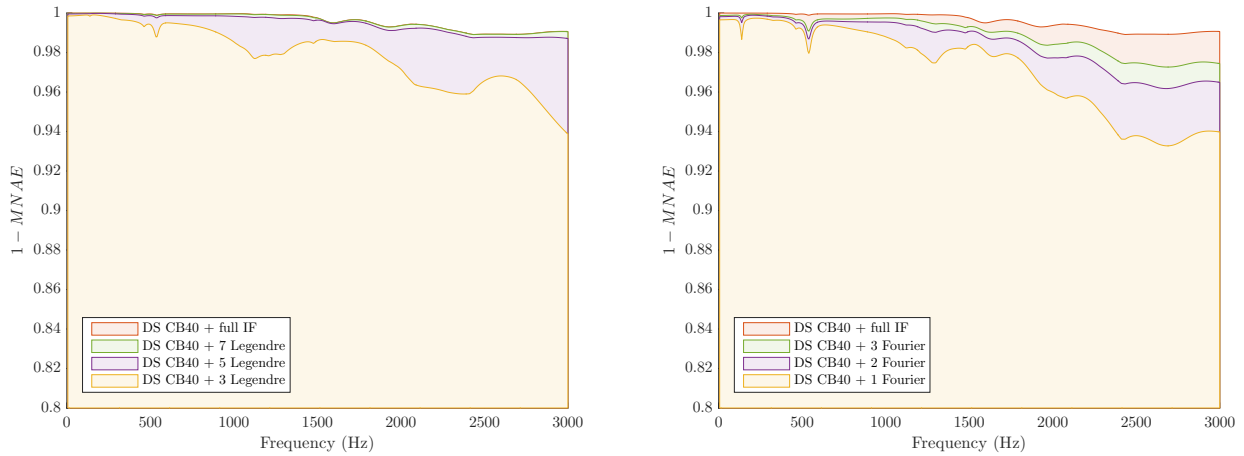
(b) Interface displacement field (x) at 1650 Hz

Figure 8.7: Interface displacement fields

Legendre versus Fourier

A comparison is made between performance of Legendre and Fourier series. As increasing the order of Fourier by one, adds two DoF to the reduced coordinate system instead of one as for Legendre, the comparison is based on amount of DoF, rather than polynomial order. For example, 1st and 2nd order Fourier respectively corresponds with 3th and 5th order Legendre, containing 4 and 6 DoF. Figure 8.8 shows the error measurement (note the scaling) for several orders of Legendre and Fourier series, based on equal amounts of DoF. Though both methods show convergence, Legendre series converge more rapidly. Considering the physical shapes of the displacement fields, for example in figure 8.7, the cause of this difference becomes visible. Referring to figure 4.1, it can be

observed that Fourier series have a cyclic nature, while Legendre series show a diverging appearance towards the edges of the range. Due to the free edges of the interface, the plates tend to behave in this manner, thus rather resembling any Legendre series. Though in this particular case, Legendre series do perform better than Fourier series, no guarantee can be given. Realising that cases are not uncommon where a system interface tends to behave cyclic, Legendre series should not yet be granted a default status. This would for example be the case where the interface edges are either fixed, or connected to each other, such as for a circular section.



(a) 1- Mean Normalized Absolute Error

(b) 1- Mean Normalized Absolute Error

Figure 8.8: Error measurement of the test model using various orders of Legendre and Fourier reduction bases

8.3 Proportionally damped, flexibly connected plates

Not always will a rigid connection between substructures be a valid modelling choice. Especially if connection design is used as a tool to influence the dynamics of an assembly, a flexible connection between substructures is of relevance. The base model is extended with simple Kelvin-Voigt elements (figure 5.1) between boundaries, implemented following the approach described in section 2.5.1.

Again, two extreme scenarios exist which should be avoided. If the stiffness of the connecting elements is chosen to be large, the structure will tend to behave as if it is rigidly connected. If the stiffness is chosen to be small, the structure will tend to behave as if the substructures are not connected at all. The latter scenario does provide a hint on performance of the interface reduction as a function of the stiffness. As for the rigidly connected case, the interface motion is generally dominated by the stiffest substructure, a flexible connection will lead to less dependent motions, which can now only be described dually. In order to obtain results of practical value, the Kelvin-Voigt element parameters are chosen such that neither extreme case is approximated: $E = 1000 \text{ N/m}$ and $\xi = 0.005 \text{ Ns/m}$. Each pair of nodes is coupled by two of these elements, one for x -direction and one for y -direction. Though possible, no cross-couplings are defined. The same global proportional damping model is used as in section 8.2. Figure 8.9 displays the resulting model. The amount of springs and dampers shown is limited for graphical reasons.

Given the fact that on a global scale, no new properties are assigned, OPS performance is only expected to be influenced by the decreasing dependence between substructures. This implies a reduced rate of convergence for the more flexible substructure, as it partially regains its modes of higher frequencies due to the flexible connection.

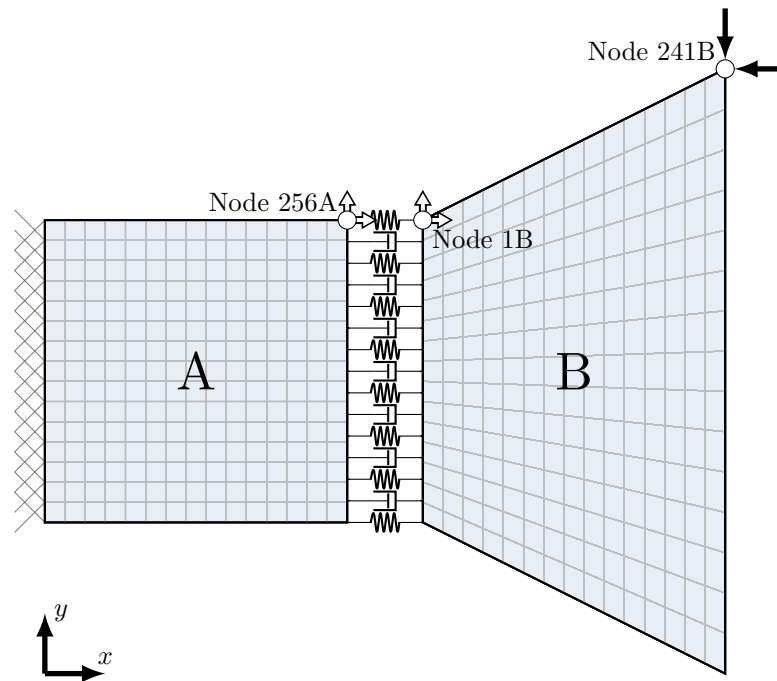


Figure 8.9: The base test case consisting of two plane stress substructures, A and B

On damped connections...

In order to get a grasp on the effects of damped connections, Woodhouse's theory as described in section 5.3.2 can serve as a useful tool in the physical occurrences. Though yielding an approximative theory, its basis of first order inclusions provide a fair indication of dominant tendencies in the underdamped range.

First considering modal damping, damped modal frequencies are generally known to decrease without its corresponding mode shape being altered. In terms of OPS solution space, this implies a similar shift in the error curve, thus overall increasing over frequency.

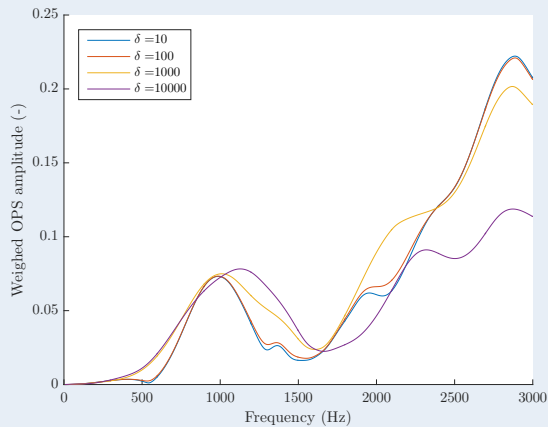
As interface damping is a local phenomenon, its induced damping matrix will never be proportional in a global sense, leading to non-uniform hysteretic effects, altering mode shapes. These effects are characterized by the off-diagonal entries of the modal damping matrix. As the quantities of these entries are system specific, no general presumptions can be done on this basis. Though equation 5.37 and figure 5.5a suggest that alterations of the normal mode mainly involve shapes corresponding with close vibration frequencies, indicating limited potential increase of spatial frequencies within interface displacement modes.

Also, despite non-proportional damping effects, a uniform interface damping model, accompanied with mostly uniform mass and stiffness within and between substructure boundaries, does lead to locally proportional tendency. This property suggests minimal impact in local modes that are mainly active on the interface boundaries.

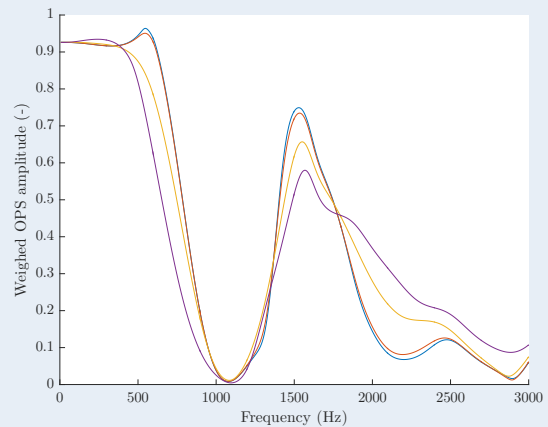
To gain insight in the impact of boundary damping on the shape of the boundary displacement field, the contributions of a lower and a higher order Legendre term are measured for various dashpot constants (δ) of a full boundary solution are displayed in figure 8.10. Due to the low stiffness of the

connecting springs compared to the substructures themselves, the damping is mostly active in the lowest modes (< 100 Hz). While these modes are nearly critically damped at $\delta = 10$ Ns/m, the amplitude weights hardly change with vast overdamping of these lower modes at $\delta = 100$ Ns/m. Now significant differences in amplitude distribution only start when damping becomes so large that it starts to impact vibrations within substructures themselves ($\delta = 1000$ Ns/m), up to the range where the effect of damping is mostly rigidifying ($\delta = 10000$ Ns/m).

Concluding, the transition from only local effects, up to rigidification due to damping is slightly turbulent due to interaction with substructure vibration modes and is thus a factor of uncertainty in a priori error mitigation.



(a): Contribution of the 2nd order Legendre term



(b): Contribution of the 8th order Legendre term

Figure 8.10: Contribution of Legendre terms to the boundary displacement field (x -direction, substr. A)

8.3.1 Results

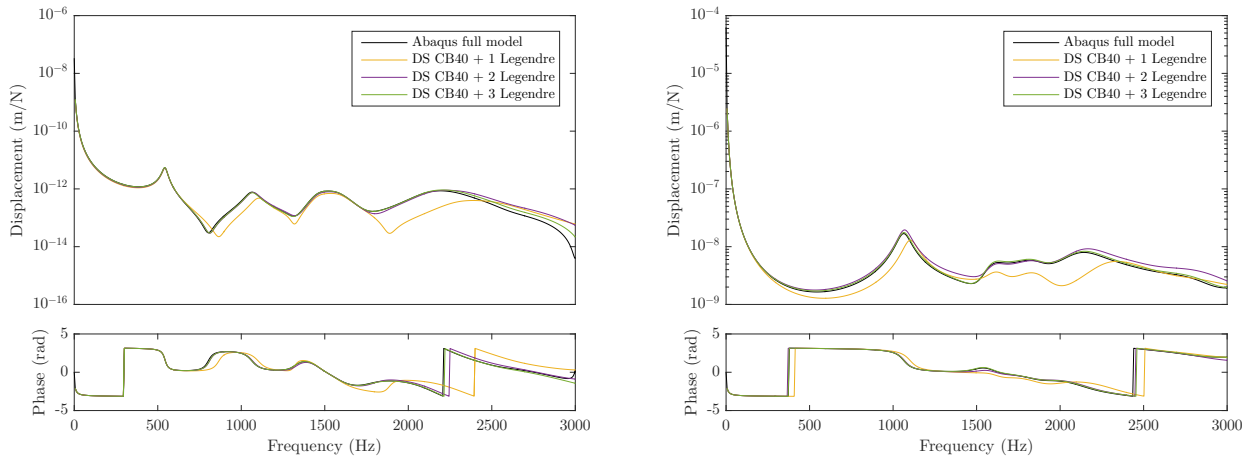
To evaluate on the expectation, relevant comparison mainly involves differences between both coupled substructure boundaries, but also the rigidly connected case described in section 8.2. Though plotted FRF in figure 8.11 still show similarity, mainly regarding resonance and antiresonance frequencies, clearly a significant degree of independence has been reached. The same can be seen comparing to the rigidly connected case in figure 8.5. This is a sign of balanced influence of either substructure which is aimed for.

With respect to the rigidly connected case in figure 8.6, errors have visibly increased, as can be seen in figure 8.12. Though this increase is according to the presumption, its validity cannot be confirmed without meeting its condition: more spatially frequent behaviour with respect to the rigidly connected case.

The coupled boundary displacement fields at 3000 Hz are displayed, together with the solution of the rigidly connected interface, in figure 8.13. Observing the decreased distance between local maxima at both sides with respect to the rigidly connected interface, the presumption of the cause is not only strengthened, its impact is somewhat predictable with knowledge of free interface vibration modes.

Comparing the flexibly connected boundaries among each other, show a significant difference as well. An increased error along substructure A can be explained by distinguishing A to be the receiving substructure,

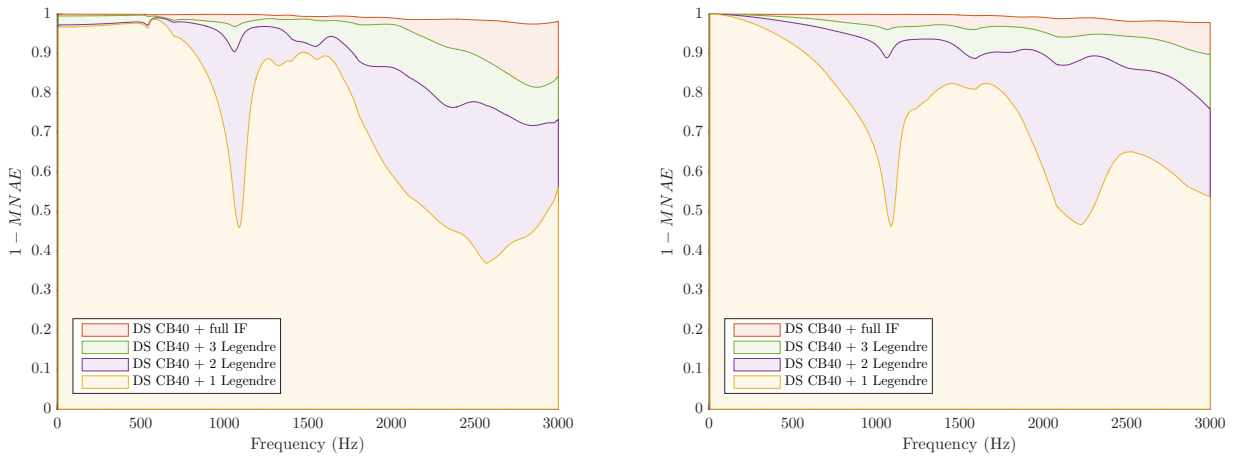
while B being the transmitting one. As the load is firstly transferred to the boundary of B , the load arriving at substructure A already contains an error due to the limited solution space of the boundary at B . With that comes the additional error of the limited solution space at A itself.



(a) FRF node 241B(y) to node 256A(y)

(b) FRF node 241B(y) to node 1B(y)

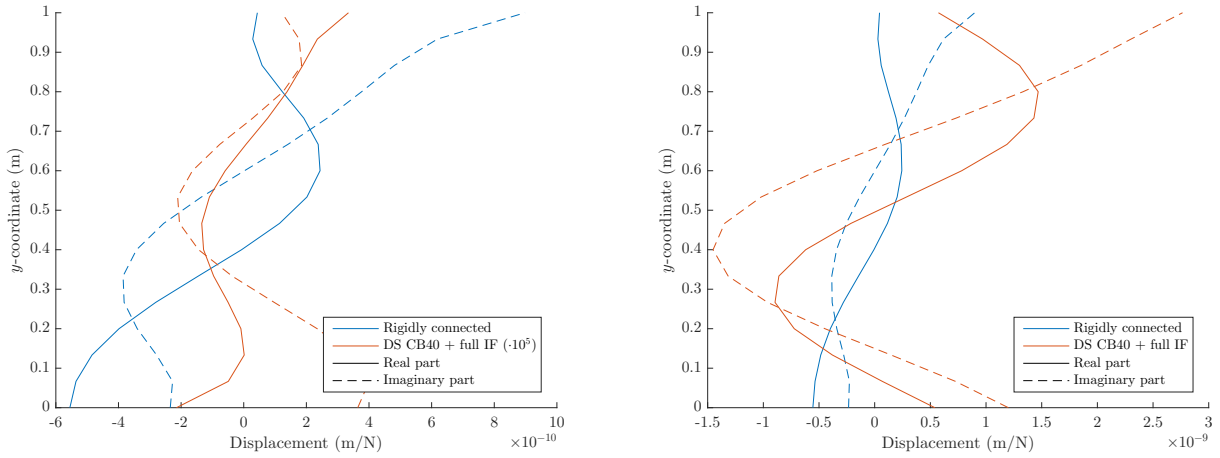
Figure 8.11: FRF to both corresponding coupled nodes



(a) 1 - Mean Normalized Absolute Error (substr. A)

(b) 1 - Mean Normalized Absolute Error (substr. B)

Figure 8.12: Error measurement of the test model along both connected boundaries



(a) Boundary displacement field (x , substr. A) at 3000 Hz (b) Boundary displacement field (x , substr. B) at 3000 Hz

Figure 8.13: Error measurement of the test model along both connected boundaries, forced in y -direction

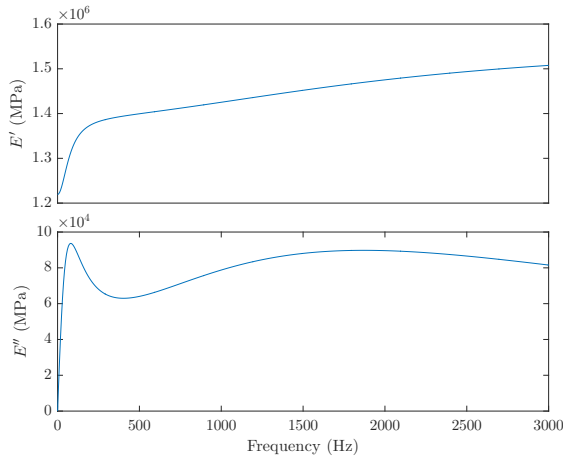
8.4 Proportionally damped, viscoelastically connected plates

To enable a wider range of connecting material models, the previous case is extended to host arbitrary frequency dependent properties. As long as mass can be neglected, the variational properties can be projected on a linear spring model, such that the flexible coupling approach in section 2.5.1 is still suitable. If additional mass is to be taken into account, another substructure is to be created which is processed as a rigidly connected viscoelastic substructure of which case is analysed in the next section. The aim of this section is to analyse the effects of viscoelastic connections only, which are thus assumed to be massless.

EPDM rubber

A material with pronounced viscoelastic behaviour which is widely used in building connections such as dilation joints, is EPDM rubber. Its characteristic relaxation behaviour under room temperature can be modelled using a Generalized Maxwell model [40]. Its model properties are found in 8.2.

Due to the large difference in range between dominant frequencies of the in-plane steel plate modes (< 3000 Hz) and variations of EPDM properties (< 10 Hz), the EPDM frequency scale has been fictively stretched with a factor 300 resulting in a dynamic modulus as plotted in figure 8.14. Though this is an artificial and unrealistic measure, it stimulates the impact of variational properties, which also relate to a more practical aspect: interaction between EPDM and bending vibrations in building structures which also appear in a low frequency range.



EPDM properties

E_0	1.2192 MPa
E_1	0.1662 MPa
E_2	0.1747 MPa
ξ_1	0.0039 MPa s
ξ_2	0.1116 MPa s

Figure 8.14: Dynamic modulus of the modified EPDM Table 8.2: Original EPDM properties

The test case presented, extends the case of section 8.3 by replacing all Kelvin-Voigt elements by Generalized Maxwell elements with the modified EPDM properties and a base stiffness of $E(0) = 1000$ N/m, resembling a layer of almost 1 mm. Figure 8.15 displays the resulting model. The amount of Generalized Maxwell elements shown is again limited for graphical reasons.

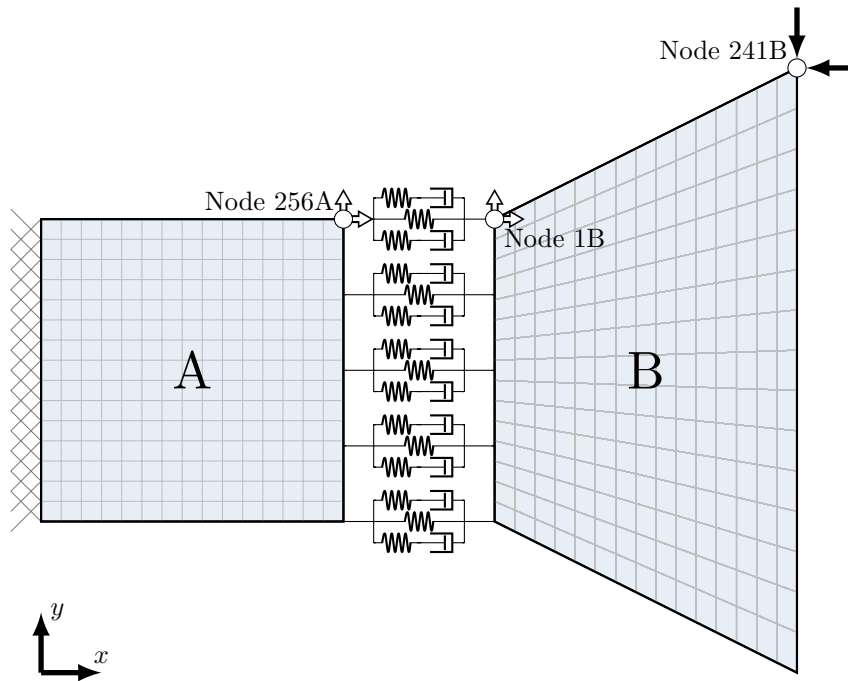


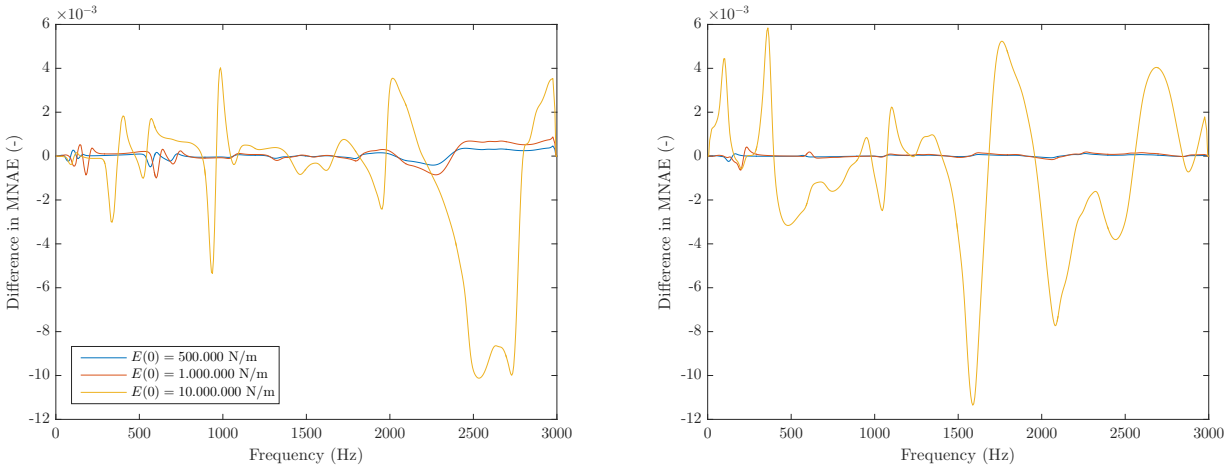
Figure 8.15: Two steel plate substructures, A and B, connected by Generalized Maxwell elements resembling modified EPDM

As stiffness and damping are fully determined by the model itself, errors are to be expected following the same principle as in section 8.3, where the boundary displacement fields are shaped through free interface modes and their mutual dependence. As discussed previously, the amount of damping active on the interface can be considered small and is not expected to significantly impact the shape of the displacement fields. The connecting stiffness, on the other hand, does govern the dependence of the displacement field. According to

the same principles, the more flexible substructure is expected to show smaller errors for increasing connecting stiffness, while the error for the stiffer substructure should increase, both due to compromising motion.

8.4.1 Results

The frequency dependent properties turn out to have minimal effect on the analysis performance. Though FRF are influenced by stiffness/damping variations, differences in errors are negligible. For this reason, some additional error comparison is done with scaled connecting stiffness in a more sensitive range. Figure 8.16 shows the difference in MNAE values for the depicted cases, where a positive value means that the error is larger for the viscoelastic case. Though the error clearly depends on the base stiffness of the connections, the range of the error increase remains significant. Thus the earlier presumptions cannot be excluded, but their relevance can. As of the peaks, the error differences appear more to be a result of slightly different resonance frequencies than of a general tendency due to stiffness increase.



(a) MNAE difference, substructure A

(b) MNAE difference, substructure B

Figure 8.16: Error difference between the flexibly (constant) and the viscoelastically connected case

Concluding, subtle frequency dependent properties do not demand additional error control. In order to define wide acceptable limits beyond 'subtle', further investigation is required. Though, in any doubtful case, error control can be based on extreme values within stiffness and damping.

8.5 Proportionally viscoelastic, rigidly connected plates

Though Kuether presents solid theory for Modified Craig Bampton reduction, an important aspect in its performance is not covered. Currently, comparison is made between full order FEM and MCB with either whole complex fixed interface modes, or only their real parts. In order to determine the relevance of the method, comparison should be made based on a fixed number of DoF retained, with classical CB reduction as a reference.

There is no reason to presume inaccurate results with CB reduction for viscoelastic substructures. To prove this, an ideal, nevertheless applicable example is examined where a substructure exists of one viscoelastic material as a whole. Given this, frequency dependent property variations will remain proportional to the static stiffness of the substructure. Similar as for Rayleigh damping, this fact solely alters the eigenfrequencies of the modes, without affecting the mode shapes implying any operations towards complex mode computation to be redundant.

Realistically, it may often be impractical to let substructure bounds be governed by material choices. Thus

any increase in disproportional variations cause alteration in the damped mode shapes with respect to the undamped ones, such that MCB is still of interest. The question remains whether considering complex eigenmodes is worth covering a narrower frequency range as for an equally sized classical CB reduction basis, or an MCB basis consisting of only real parts of the complex eigenmodes.

Both a case with proportional and disproportional viscoelasticity are investigated to validate relevance of MCB reduction. No interface reduction is performed. The case presented in section 8.2 has been adjusted slightly to fit the purpose: The modified EPDM model is projected onto the steel properties of substructure B . Substructure A remains Rayleigh damped using the same parameters. Figure 8.17 illustrates the case, where yellow depicts viscoelastic material.

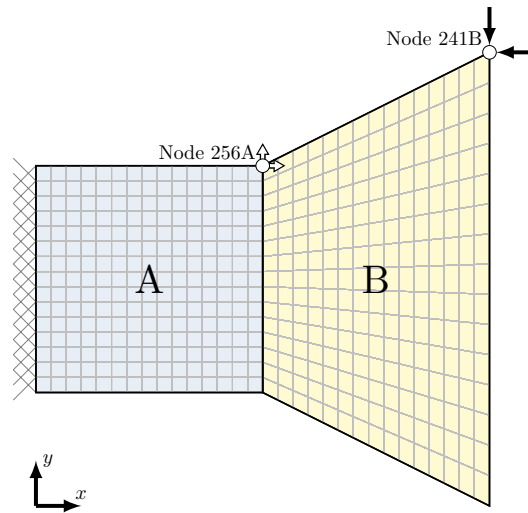


Figure 8.17: A Rayleigh damped (A), and a viscoelastic substructure (B), rigidly connected

8.5.1 Results

Computing both undamped as complex eigenmodes for substructure B , the same shapes are obtained (containing no imaginary contribution). This confirms the relevance of classical CB reduction in viscoelastic substructures, firmly when considering proportional property variation, and potentially for disproportional as well. The latter is further investigated in the next subsection.

8.6 Disproportional viscoelastic, rigidly connected plates

In order to introduce significantly disproportional property variations in substructure B , the rigidly connected base case is expanded by connecting its lower boundary to a base, using a series of Generalized Maxwell elements. Again, the modified EPDM model is projected onto the base stiffness of the elements, which is chosen to be $E_0 = 100.000 \text{ N/m}$, such that they have a significant impact on the dynamics of the structure. One element is connected to each node along the boundary, active in y -direction. The plane stress elements are still characterized by steel properties with a Rayleigh damped model. The case is visualised in figure 8.18, again the amount of Generalized Maxwell elements shown is limited for graphical reasons.

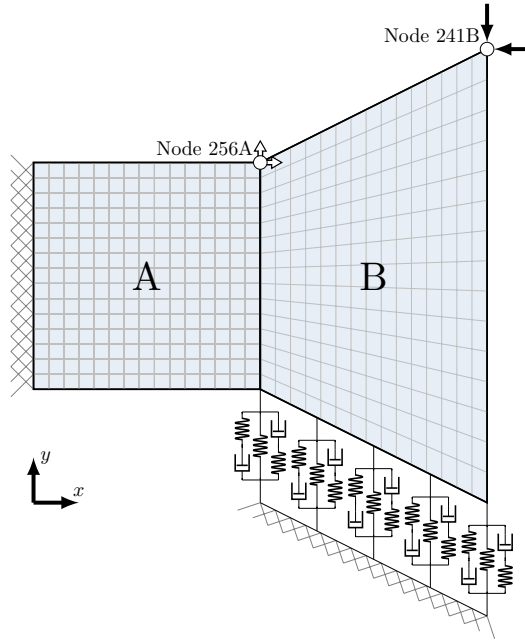


Figure 8.18: Substructure B being disproportionally viscoelastic due to addition of Generalized Maxwell elements

8.6.1 Results

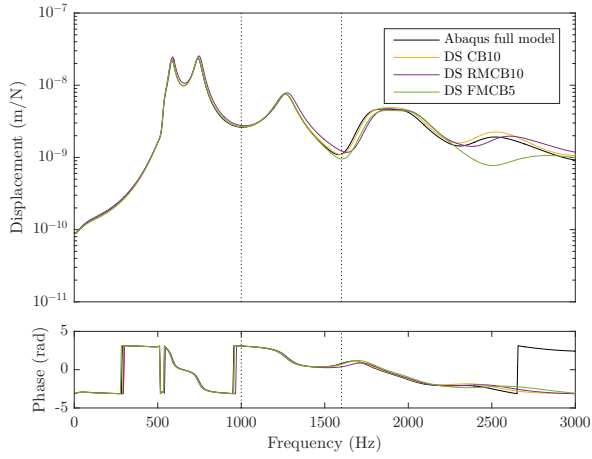
Comparison is made between reduction bases of equal sizes. A full MCB basis thus contains half the amount of vibration mode shapes as a classical CB or a real valued MCB basis of comparable computational demand. Due to the difference in modal frequencies spanned, accurate results are expected within a narrower range for full MCB. Using the rule of thumb of including eigenfrequencies up to double the upper frequency of interest (which is also advised by Kuether for MCB [15]), three frequency ranges can be distinguished. The lowest range is where full MCB is expected to perform well, thus a range where fair comparison is made between full MCB and the other reduction bases. The middle range is where classical CB is expected to perform well without consideration of frequency dependent material properties. The remaining, highest frequencies is where large errors are accepted, proper to the fixed interface modes included. The ranges are separated by dotted lines in the coming plots. Figure 8.19 displays an FRF for various reduction bases. Qualitatively, all reduction bases display acceptable (no significant misestimates of (anti-) resonance peaks) results within the expected ranges.

Fair comparison thus requires error quantification as displayed in figure 8.20. Though the damping included is sufficiently small according to [31], in order to justly expect an accurate basis of complex modes, the approximative modes do under-perform with respect to undamped modes. Explanation can be sought in reflection of Woodhouse theory (see section 5.3.2).

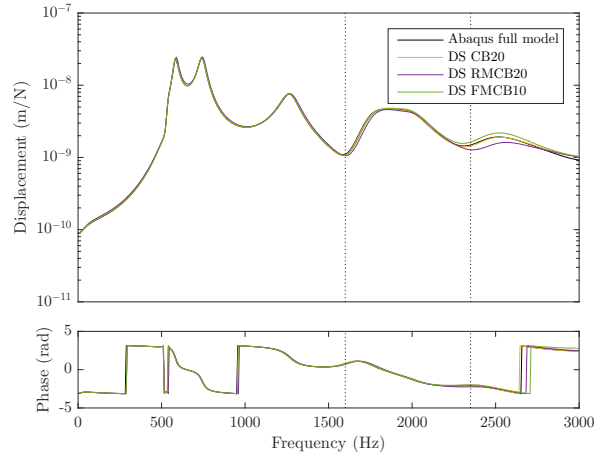
The errors induced by assumptions are investigated. The first approximation is made by computation of the eigenvalues in equation 5.33, which assumes that $\omega_n^2 \gg C'_{nn}$. Including also the second order terms truncated, the error within the approximated complex eigenfrequency e_{ω_n} is found to be:

$$e_{\omega_n} = \pm \frac{\sqrt{4\omega_n^2 + \sum_{j=1} C'_{nj} \alpha_n}}{2} \quad (8.1)$$

Though e_{ω_n} does not affect the mode shapes in the method presented, it is mentioned for later reference. The error within the n^{th} complex mode are induced, also by truncating second order contributions, as well as assuming the complex frequencies to be very close to the undamped frequencies, resulting in n error e_{ϕ_n} :

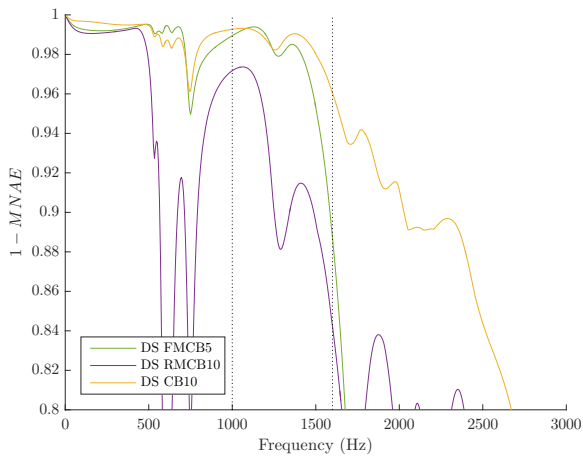


(a) FRF node 241B(y) to node 256A(y)

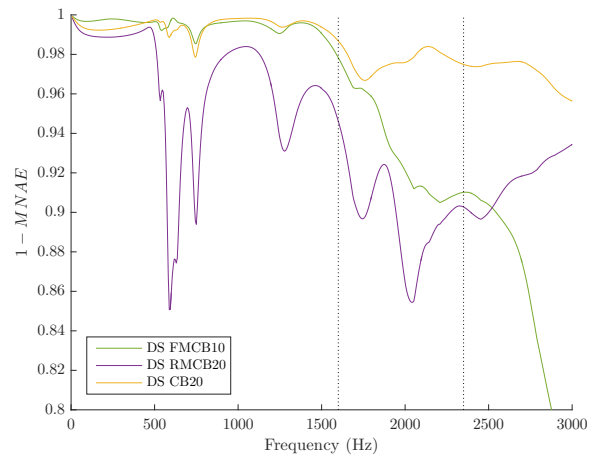


(b) FRF node 241B(y) to node 1B(y)

Figure 8.19: FRF to both corresponding coupled nodes



(a) 1 - Mean Normalized Absolute Error (substr. A)



(b) 1 - Mean Normalized Absolute Error (substr. B)

Figure 8.20: Error measurement of the test model along both connected boundaries

$$e_{\phi_n} = i \sum_{k \neq n} \left(\frac{\bar{\omega}_n C'_{kn}}{\omega_k^2 - \bar{\omega}_n^2 + i \bar{\omega}_n \sum_{j=1} C'_{nj} \alpha_j} - \frac{\omega_n C'_{kn}}{\omega_n^2 - \omega_k^2} \right) \phi_k \quad (8.2)$$

Notice from equation 8.2, the error increase hyperbolically with the difference between undamped and complex frequencies. Also, the error is proportional to the off-diagonal terms of dissipation matrix \mathbf{C}' . Both issues are indeed both controlled by limiting the amount of damping, but considering any kernel function $\mathbf{G}(\omega)$ instead of a damping matrix \mathbf{C} , it now becomes clear that large variation of stiffness over frequency induce an error of the same order. Since the EPDM properties used indeed possess large variation of stiffness with respect to the small damping norm, the errors observed in figure 8.20 do make sense, but call for revised usability limits of Rayleighs/Woodhouses approximative method.

On the accuracy of the vibration modes...

A small study is performed to gain an indication of effectiveness of different approximative bases with respect to the exact complex modes. The plate model of substructure A of the priorly presented cases is attached to a series of Generalized Maxwell elements, with the properties as presented in figure 8.14. The resulting model is shown in figure 8.21.

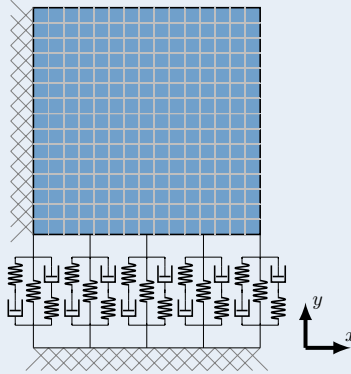


Figure 8.21: A plane stress plate structure with Generalized Maxwell elements attached

The first 40 vibration modes are computed and compared using their mean MAC values (see equation 6.1). As feasibility of computing exact complex modes is usually limited to polynomial description, the viscoelastic properties of the Generalized Maxwell elements are projected as such for various orders of stiffness and damping functions. Also the effects of different orders of magnitude of the base stiffness of the Generalized Maxwell elements are investigated.

Due to the apparent under-performance of the Woodhouse complex modes in the case presented earlier in this section (see figure 8.18), an enhancement has been made to the Woodhouse method, as presented by Adhikhari [41]. This adjustment rejects the assumption of undamped frequency being sufficiently close to the exact complex frequency and uses the approximative complex frequency as described in equation 5.33, with an error described in equation 8.1.

Also the influence of a proposed inclusion rate of $p = 0.9$, within the context of the truncation theory described in section 5.3.3, is tested.

The results are displayed in table 8.3. As mentioned that Woodhouse theory should be define a limit in variation of stiffness besides damping, the results are in accordance. Linear and quadratic stiffness affect the modes significantly compared to the linear damping, which is considered small.

Though quadratic properties should not significantly increase the maximum stiffness/damping, errors are increased tremendously with respect to linear properties. It is seen that it causes the complex modes to be altered even more with respect to the undamped modes, implying increased contribution from neighbouring modes, of which the coefficients induce errors. Woodhouse approximation should thus require another restriction based on this aspect.

Generally, Woodhouse modes only improve the undamped modes slightly, questions their usability, especially considering the fact that occupy double the amount of DoF. The improvement of Adhikari results in a major increase of MAC values within the reasonable limitations mentioned before. Therefore they offer a considerable compromise between accuracy, with respect to undamped modes, and computational efficiency, with respect to exact complex modes.

The truncation within the approximative approach results in minimal decrease of MAC values, suggesting the proposed inclusion rate of $p = 0.9$ to be acceptable or even conservative.

Mean MAC of the first 40 vibration modes

$E_0 = 100$ N/m	Und. modes	Woodhouse	Adhikari	Trunc. Adh.
Linear stiffness, no damping	0.9890	0.9990	0.9988	0.9988
Constant stiffness, linear damping	0.9995	0.9998	0.9999	0.9999
Linear stiffness and damping	0.9889	0.9989	0.9980	0.9980
Quadratic stiffness and damping	0.9506	0.9542	0.9929	0.9928
$E_0 = 1000$ N/m				
Linear stiffness, no damping	0.9774	0.9896	0.9981	0.9980
Constant stiffness, linear damping	0.9983	0.9996	0.9998	0.9998
Linear stiffness and damping	0.9772	0.9890	0.9985	0.9984
Quadratic stiffness and damping	0.6167	0.6556	0.6663	0.6697
$E_0 = 10000$ N/m				
Linear stiffness, no damping	0.8807	0.8955	0.9486	0.9482
Constant stiffness, linear damping	0.9958	0.9953	0.9995	0.9994
Linear stiffness and damping	0.8793	0.8940	0.9468	0.9468
Quadratic stiffness and damping	0.4234	0.3604	0.2830	0.2928

Table 8.3: Mean MAC values of undamped modes and several approximations of complex modes with respect to the analytical complex modes

Chapter 9

Building case and results

As the conceptual value of several reduction techniques has been investigated in part II, the next step is to verify their performance in a more practical context. To do so, a case has been developed which is typical for the engineering challenge introduced in chapter 1: minimization of nuisance due to low frequency vibrations in light weight buildings. An assembly of building components is used for representing such a case.

The testing procedure essentially follows the one presented in chapter 7, though evaluation is also covered from a more practical point of view compared to the plane stress plate case. Performance is measured not only at the interfaces, but also separately at clear points of interest such as wall or floor panel centres.

9.1 Model design

A common type of timber frame building is modelled with beam and shell elements. The structure exists of interconnected portal units, existing of rectangular 150 mm × 70 mm studs, which support the 300 mm × 70 mm spanning joists. Walls are created by attaching a 12 mm laminated plywood plate to each side of the stud rows. Floors exist of 24 mm plywood plates with a 60 mm layer of screed poured on top of it. These composite floors are attached to the joists. For lateral stability, each portal unit also contains a panelled frame in the spanning direction. The span, depth and height of a portal respectively are 5 m, 6 m and 3 m. The depth of the back wall is also 3 m. All timber elements are made out of spruce wood. Proportional damping of approximately 1-1.5 % on each mode is assumed. The portal unit is illustrated in figure 9.1.

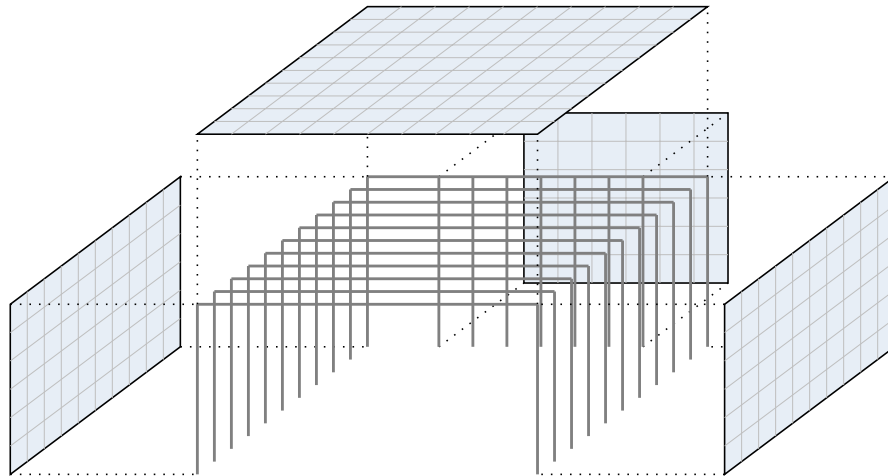


Figure 9.1: Exploded view of a portal unit

Model assumptions

For studs and joists, 2-node beam elements are used with 6 DoF at each node. Wall and floor panels exist of 4-node flat shell elements, also containing 6 DoF per node. Element dimensions (thickness excluded) are 0.6 m in direction of the portal height and depth, and 0.5 m in the direction of the span, resulting in a fully orthogonal mesh. All connections between studs and joists are modelled as fixed in all translational and rotational directions, while panel-to-joist or panel-to-stud connections are fixed solely in translational direction. Studs are constrained to be clamped at ground level.

Some additional modelling simplifications have been allowed as they hardly compromise the approximate behaviour of the structure. Timber parts are assumed to be isotropic, their stiffness governed by bending properties parallel to the grains. The double plywood wall panels have been integrated into a single panels with double the thickness. Since no element offsets are used, this measure results into a higher bending stiffness, which compensates for their collaboration through the studs. Also the screed-plywood composite floor properties have been combined into a single element layer with weighed material properties based on partial mechanical collaboration due to bonding. Element and material properties are summarized in table 9.1.

Element properties				
Parts	Studs	Joists	Wall panels	Floor panels
Element type	2-noded beam	2-noded beam	4-noded flat shell	4-noded flat shell
Integration points	5×5	5×5	1×5	1×5
Mass matrix	Lumped	Lumped	Lumped	Lumped
Material & cross-sectional properties				
Parts	Studs	Joists	Wall panels	Floor panels
Material	Sawn spruce	Sawn spruce	Spruce plywood	Spruce plywood / screed
Young's modulus	9.0 GPa	9.0 GPa	8.2 GPa	5.5 GPa
Density	500 kg/m ³	500 kg/m ³	460 kg/m ³	1560 kg/m ³
Poisson ratio	0.2	0.2	0.2	0.2
Section dimensions	150 mm \times 70 mm	300 mm \times 70 mm	24 mm	84 mm

Table 9.1: Element and material properties of the timber frame construction model

Substructure division

Next, two components are shaped using the properties of the introduced portal structure. Both components are designed such that they can easily be repeated within an assembly. To prevent walls from overlapping, one component contains wall parts on the sides, while the other component has cantilever floors on the sides. The components and their configuration are illustrated in figures 9.2 and 9.3 respectively.

An assembly is constructed by connecting 6 substructures, resulting in 4 storeys, each spanning 7 floors. This results in a sizeable FEM model containing 51780 participating DoF, of which red 1218 are located at a substructure interface. Evidently, such a model would be benefited by an accurate order reduction.

The reduction bases

Chapter 8 has proven the conceptual value of used techniques and their relative performance under various complications. This test model serves to place the occurrences of expected errors into a reference frame, such that practical feasibility is ascertained.

Once again, an Abaqus analysis solution is used to verify the correctness of Matlab procedures. Though for error measurements, a reduced order model is used as reference. This reference model uses unreduced interfaces

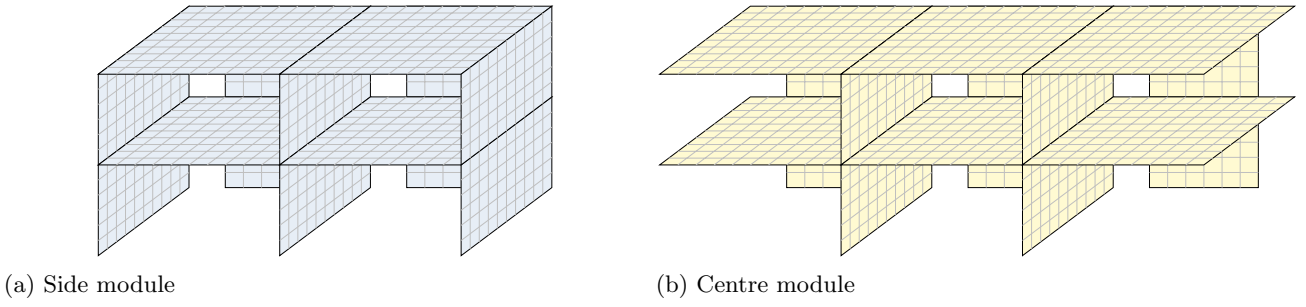


Figure 9.2: Geometry and mesh of the modules

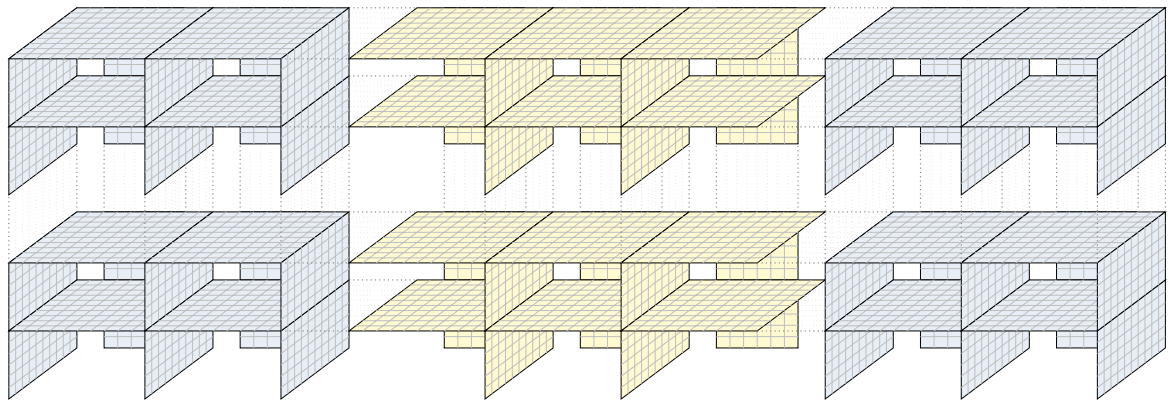


Figure 9.3: Substructure configuration

and contains 100 vibration modes for each substructure, covering a range up to 60 Hz, which is far higher than the generally accepted lower limit for the frequency range considered.

The solutions to be examined all involve a Craig-Bampton reduction, retaining 30 vibration modes, covering a range up to 30 Hz, which is the norm for accepted interior reduction in this case. A full interface solution is presented to quantify the error due to this further interior reduction. Thereafter, solutions with various orders of Legendre OPS reduction are considered.

Next, performance at the interfaces is discussed and related to phenomena encountered in chapter 8. Consecutively, the influence on the DoF of interest is considered. Ultimately, the analysis is extended by taking a prescribed signal into account, and computing its time domain response, such that it can be related to applied comfort norms [42, 43].

Assembly

Figure 9.4 displays the assembled structure with coordinates of reference. A vertical load is applied on the centre node of Floor A. Responses are measured at all interfaces and floor/wall centres (out-of-plane). Floors B and C, interfaces I and II are marked for further reference.

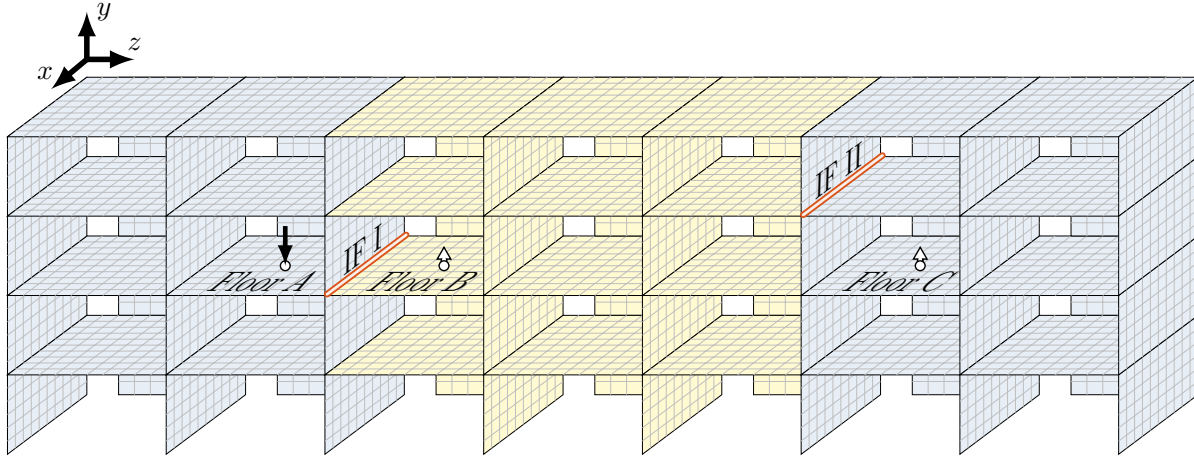


Figure 9.4: Assembly with marked coordinates

9.2 Results

As priorly suggested, analysis results are examined at different levels, in order to separate OPS reduction performance locally and their effects at locations which are most relevant for final comfort assessment. Discussion of results is therefore divided as following:

- Load to interfaces (frequency reponse)
- Load to points of interest (frequency reponse)
- Load to points of interest (time history reponse)

As to fairly analyse error trends over frequency, the frequency response results are again presented using unit loads. Though to obtain a realistic perspective on comfort assessment in practice, a characteristic load is defined before obtaining a time history reponse.

As a global performance indicator, the residual part of the original physical load is computed using the reference solution as in figure 9.5. This residual force cannot add energy to the system in the reduced domain and is thus the neglected part of the original force in the physical domain. In order to associate results with number of DoF retained, a corresponding overview is found in table 9.2.

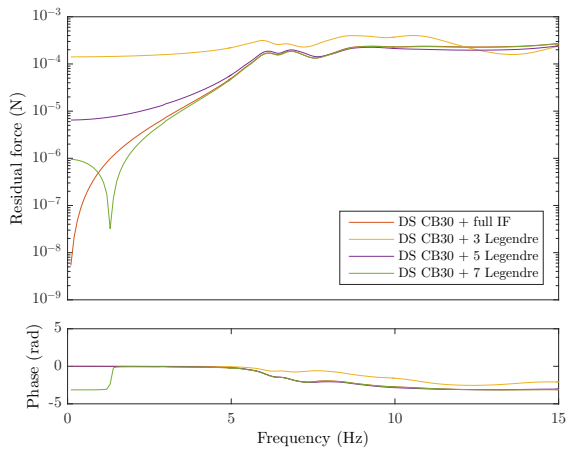


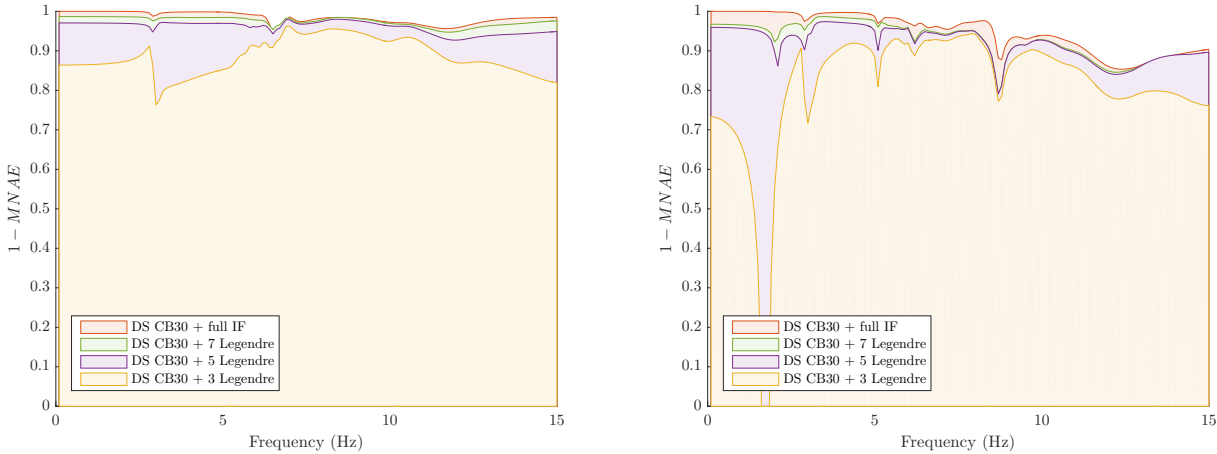
Figure 9.5: Residual of original unit load at floor A

Number of DoF	
Model	Amount
Abaqus	53952
CB100 + full IF	1818
CB30 + full IF	1398
CB30 + 7 Legendre	1146
CB30 + 5 Legendre	936
CB30 + 3 Legendre	684

Table 9.2: Retained number of DoF per model

9.2.1 Load to interfaces, frequency response

Comparison is made between interfaces I and II (see figure 9.4). The errors plots in figure 9.6 display familiar trends as seen in chapter 8. Errors show a sensible downtrend, with peaks around antiresonance frequencies and similar to the case presented in section 8.3, the quasi-static range shows relatively large errors compared to the middle range (5-10 Hz).



(a) Interface I

(b) Interface II

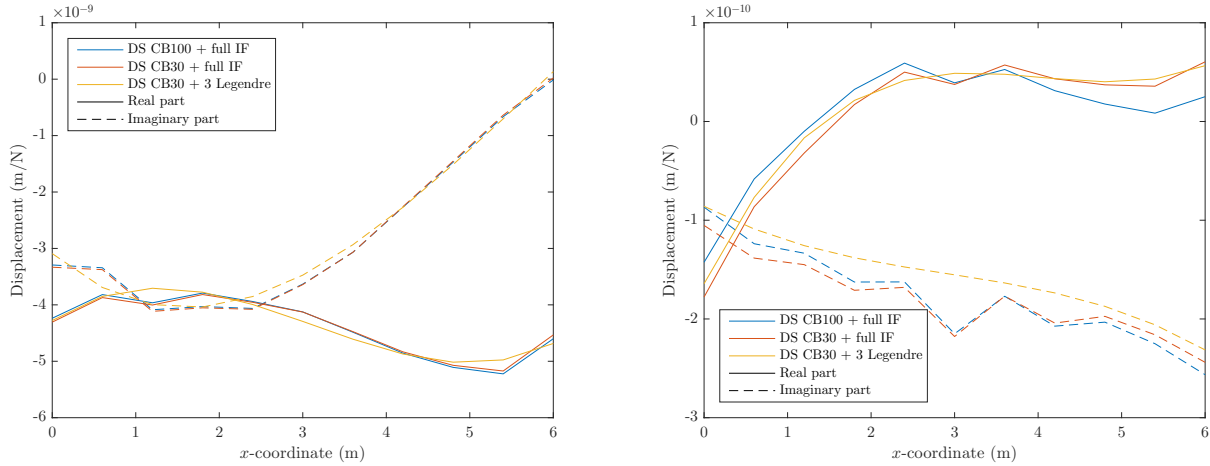
Figure 9.6: Error measurement at the marked interfaces, all directions

Transfer path

Now that multiple interfaces are used, it cannot remain unnoticed that the interface close to the load (I) performs better than an interface far from it (II). This can be explained by general phenomenon, but also a system specific one, both relate to the transfer path. Seen from the FRF, the path transferring the load to interface II tends to be more receptive to higher frequencies, filtering a lower range. Consequently, higher modes play a larger role in the motion of the interface. Truncation of high frequency vibration modes and OPS at the interface, sensibly results in larger errors at this interface.

A more general contribution to the difference in performance is due to error amplification. As the load has to travel longer path, errors compile in the signal as it travels along the nodes. Considering this, the displacement field found at the interface is not only determined by the solution space, but also by the affected signal arriving there. It can be seen quite obviously in the more extreme tendencies in the antiresonance error peaks, but also in the higher range (10-15 Hz) in the decreased performance due to Craig-Bampton reduction. Though the interface reduction does not appear to be significantly affected at higher frequencies, it is more of a coincidence, which is illustrated by frequencies where lower order reduction show smaller errors than the wider reduction bases (12-15 Hz).

Figure 9.7 confirms the above. Though interface II indeed shows tendencies of higher frequencies, it is also very visible that the displacement field does react badly to the solution space that is provided locally. This is especially clear from the the 3th order Legendre solution, where the imaginary part consistently underestimates the magnitude of its part comparing to the full interface solutions.



(a) Interface I

(b) Interface II

Figure 9.7: Interface displacement fields in y -direction at 9.5 Hz

Saint-Venant's principle

The pronounced errors in the quasi-static area can be explained with the help of Saint-Venant's principle [44], which implies that stress distributions at distance of applied loads tend to smoothen. These uniform stress distributions in so called 'Bernoulli zones' (zones at distance of applied loads) lead to simple deformation shapes over the section. Considering interface displacement fields, this principle applies, meaning that interfaces close to applied loads tend to employ in more specific shapes than elsewhere in the structure. Errors due to this kind consist of two contributions.

The first contribution, similarly as for displacement fields at high frequencies, arises from a lack of comprising shapes in the interface reduction basis. If the loading locations considered are known priorly, one may choose to resolve the issue by using larger reduction bases at interfaces near the loads.

A second contribution may come forth due to lacking correspondence with used vibration modes. Commonly, this is not an issue for loads transferred from one interface to another, as the displacement field of the whole substructure is covered by static constraint modes. These static modes do not represent shapes for loadings at interior DoF however. Again, if load points are limited and known priorly, it is considerable to add a second type of constraint modes to the reduction basis. These can be similarly as in equation 3.9, but forced DoF are now treated as interface DoF, though never at the same time. For every separated forced DoF \mathbf{u}_f , the additional interior static displacement field $\mathbf{u}_{i,add}$ is described as:

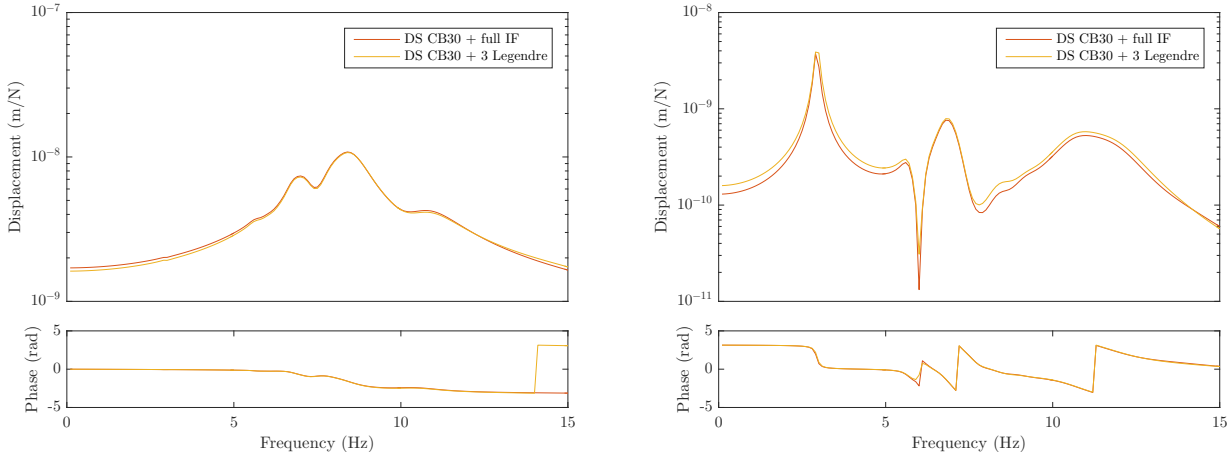
$$\mathbf{u}_{i,add} = -\mathbf{K}_{ii}^{-1} \mathbf{K}_{if} \mathbf{u}_f \quad (9.1)$$

where \mathbf{K}_{if} is a temporary partition of \mathbf{K} , resulting in a vector being column f , and keeping only rows corresponding with interior DoF.

Directions of interface degrees of freedom

A final remark has to be made that not all directions of interface DoF contribute proportionally. Directions that are less admitting to the loading contain large errors compared to actively participating DoF. Though the cause does in fact lay in the difference of admittance, no universal conclusions can be drawn. Figure 9.8 shows that the less admitting DoF (figure 9.8b) are mostly active at higher frequencies. Some modes in the lower frequency range are partially filtered and the more inaccurate higher mode shapes thus also have a larger contribution at a

lower frequency range, inducing errors. As the filtering of frequencies at interfaces has system specific effects, no general assumption can be done regarding this symptom. Though if one adequately covers the frequency range of interest with a corresponding reduction basis, this will not be of significant harm.



(a) Translational y -direction

(b) Translational z -direction

Figure 9.8: FRF at the middle node of interface I

9.2.2 Load to points of interest, frequency response

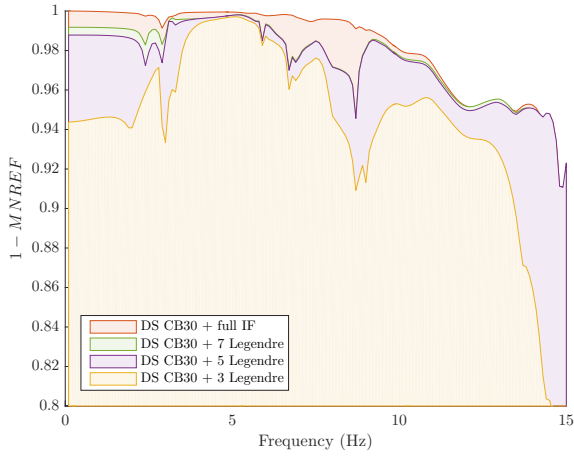
The next question that arises: to what extent are results at points of interest affected by erroneous phenomena observed at interfaces? Generally any errors along relevant paths of transmission should be expected to be of impact, with the exception of very stiff paths (such as in-plane), provided that a proper static representation is contained. In the latter case, transmission is hardly influenced by vibration modes, thus their contribution to errors is at a minimal. Figure 9.9 shows the errors at floor and wall centres. Given that only single points are measured at different locations, and errors can therefore not be normalized to a single value, the MNRE is measured rather than the MNAE. Comparing the two, MNRE may sketch a more conservative image. Keeping this in mind and comparing to the results found at interfaces I and II (figure 9.6), displacements at the points of interest appear less susceptible to errors.

Error amplification

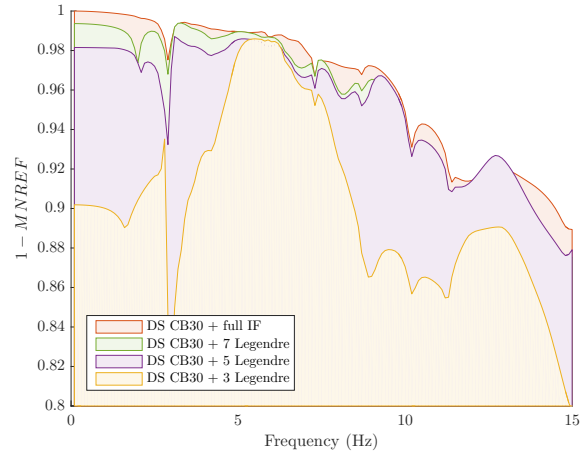
Again, differences exist between location close or far from the load due to error amplification. Though typical to the aim of the analysis is that the points of interest are the ones that are highly admitting to the loading, thus hardly filtering lower and middle frequencies (0-10 Hz), of which the modes are represented the best, minimizing errors. This is confirmed by the corresponding FRF in figure 9.10.

Walls and floors

Due to the same principle it can be seen that errors are larger in walls compared to floors. As floors and walls differ in frequency content of the admittance, the content initially transferred through floor A is prone to a higher extent of filtering when transmitted to the out-of-plane DoF in walls, compared to another floor. Similar as differences seen between translational motion at interface I (figure 9.8), what remains of the signal when arriving at a wall centre has a relatively high influence of highly frequent modes, inducing larger errors.

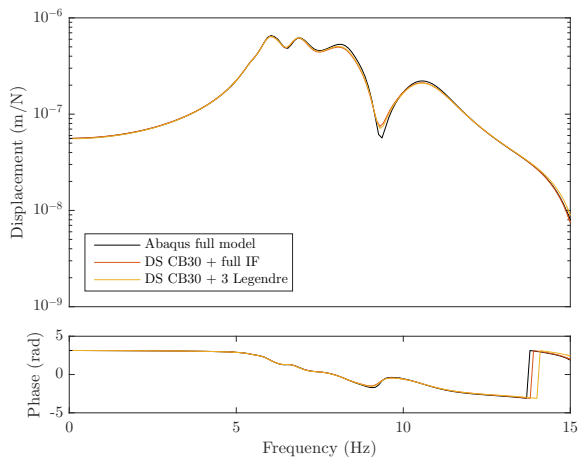


(a) Floors, y -direction

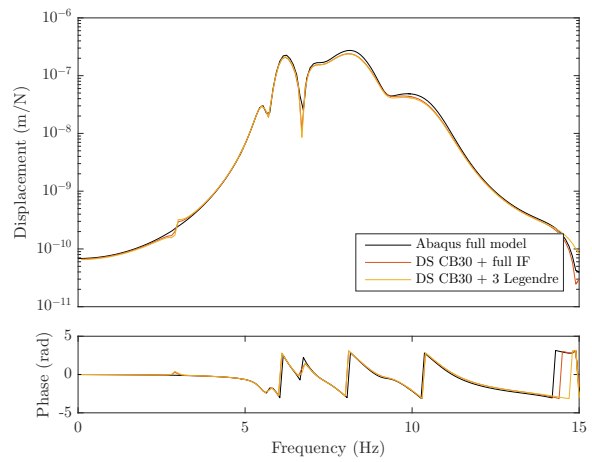


(b) Walls, z -direction

Figure 9.9: Error measurement at all floor and wall centers



(a) Floor B



(b) Floor C

Figure 9.10: FRF at the middle node floors B and C

Frequency filtering

With perspective on the goal of conceptual studies within this context, eliminating highly admitting transfer paths, resulting motion in points of interest will increasingly come from filtered paths. This will not only change amplitudes of motions, but also distribution of frequencies within the displacement spectrum. Especially when no overly stiff paths remain, loads can then only be transferred through more error prone paths and will thus negatively effect the accuracy of the results. The only way to prevent such errors from amplifying to an unacceptable extent is too keep errors small in the first place, thus by retaining sufficiently many mode shapes in the reduction basis.

9.2.3 Load to points of interest, time history response

Considering the errors observed, the final question remains to what extent verification of comfort norms is influenced. Since the criterion to be met is expressed in terms of velocity, responses to a representative load are retrieved to the time domain. A characteristic force signal due to an 80 kg person walking at a somewhat high pace (2 Hz), is established in the time domain and frequency domain (by FFT) and displayed in figure 9.11.

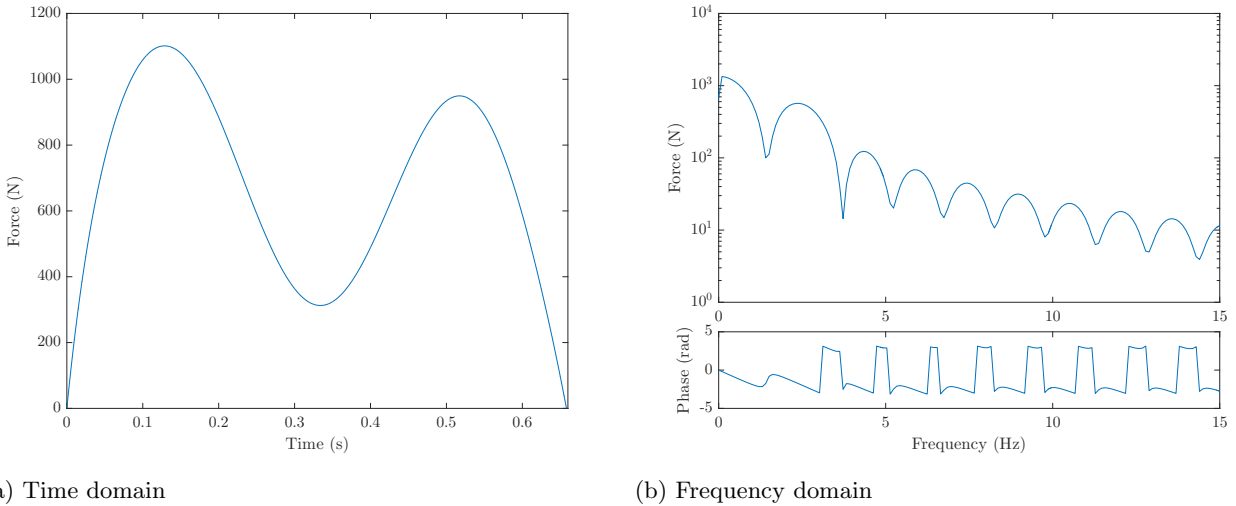


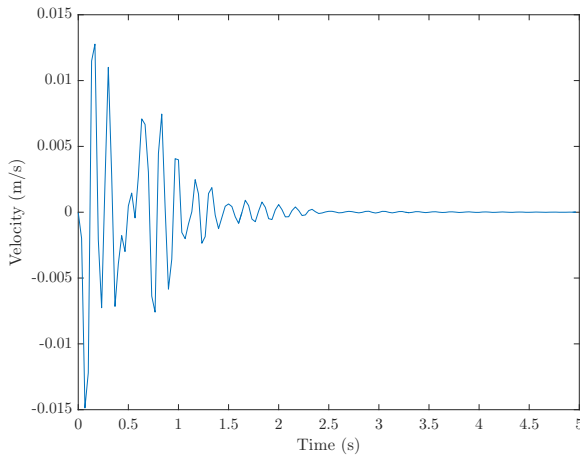
Figure 9.11: Characteristic load for an 80 kg person landing footsteps

The responses are acquired and returned to the time domain. Figure 9.12 shows sensible motion, with clear dominant impact on 0.1 s and 0.5 s. In floor C reflected signal can be observed after 1.5 s. Since the time domain solutions obtained from reduced order models are almost indistinguishable from the Abaqus solution, only the Abaqus solution is displayed.

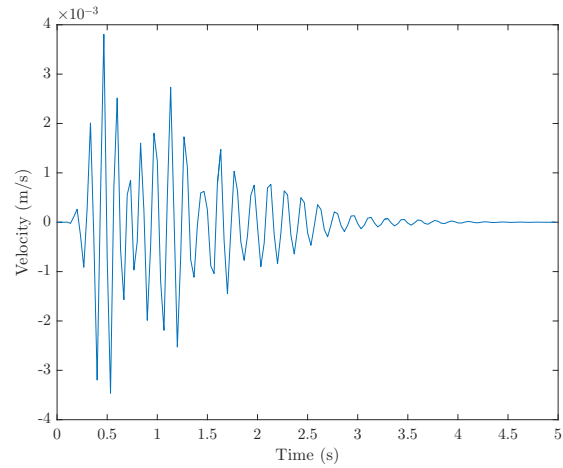
The latter fact being promising for conclusions, a final confirmation is given by table 9.3 where very small deviations in maximum velocity are measured.

Maximum velocity (mm/s)						
Model	Abaqus	CB100 + full IF	CB30 + full IF	CB30 + 7 Leg.	CB30 + 5 Leg.	CB30 + 3 Leg.
Floor B	14.87	14.97	15.00	15.00	15.00	14.91
Floor C	3.806	3.550	3.549	3.533	3.531	3.487

Table 9.3: Maximum velocity measured for models of various orders of reduction



(a) Floor B



(b) Floor C

Figure 9.12: Time domain velocity due to a footstep landing

On comfort assessment guidelines...

As to relate the presented analysis to applied comfort assessment with FEM, the background of used Dutch guidelines is elaborated. Due to the amplifying effect of multiple footsteps landing rapidly after one another, a force signal containing a minimum of 15 footsteps should be used. The force signal by concatenating single step force signals over time, for which the single signal, $f(t)$, is described using a polynomial:

$$f(t) = (K_1t + K_2t^2 + K_3t^3 + K_4t^4 + K_5t^5 + K_6t^6 + K_7t^7 + K_8t^8)G \quad (9.2)$$

All coefficients $K_1 \dots K_8$ depend on the walking pace of the considered person, which has a body weight of G . Coefficient values are found in [42]. The signal is bound to non-negative force values, resulting in a signal shape as in figure 9.11a. After concatenation of the force signals, the time domain is transformed to the frequency domain by FFT. It is then multiplied by the FRF in consideration, and by a weighing function $H(\omega)$, as to account for human perception of varying frequencies. This weighing function, characterized by a reference velocity $v_0 = 1.0$ mm/s and reference frequency $\omega_0 = 11.2\pi$ rad/s, is given as:

$$H(\omega) = \frac{1}{v_0} \frac{1}{\sqrt{\omega_0/\omega}} \quad (9.3)$$

After returning to the result to the time domain by IFFT, a dimensionless response signal is obtained for the OS-RMS (One Step-Root Mean Square) is calculated as a measurement of comfort. As the name suggest, this involves the Root Mean Square of all response samples of a single step, which is bound by the maximum velocity of the total response and the maximum velocity to either adjacent footsteps (in time), as in figure 9.13.

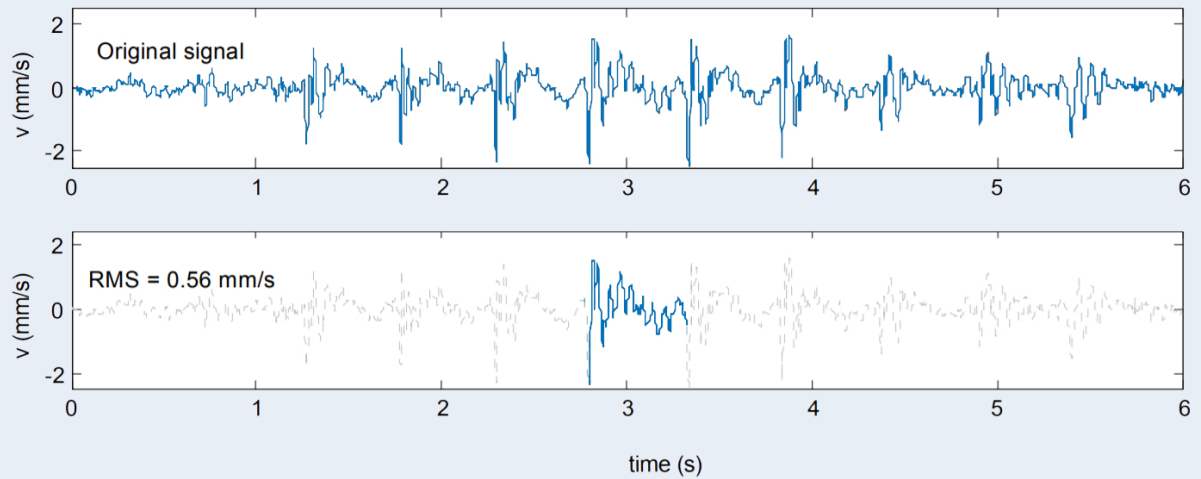


Figure 9.13: Isolating the single step response [43]

As a final design check, all OS-RMS values for combinations of walk frequency (1.6 - 3 Hz, with steps of 0.04 Hz) and body mass (30 - 125 kg, with steps of 5 kg), are computed. Weighing all values with the probability density of both variables, the 90% limit value, OS-RMS₉₀ is considered a satisfactory representation for induced hindrance. For light weight residential buildings the OS-RMS₉₀ is advised not to exceed 0.8 for response within the home hosting the activity and 0.2 for neighbouring homes.

Chapter 10

Conclusions and recommendations

This chapter reflects upon the research goals described in section 1.2 and utilizes results and observations in chapters 8 and 9 to reach conclusions. The main focuses of this research are briefly repeated as follows:

- 1 Development of a reliable interface reduction method
- 2 Assessment of the potential effects of viscoelasticity in CMS and the ability to cope with them
- 3 Creation and evaluation of practical value of CMS for buildings

Aforementioned aspects are discussed distinctly in the next section. Afterwards, recommendations are made, concerning improvements with respect to the goals of this research, but also from an extending point of view.

10.1 Conclusions

Reliable interface reduction

An essential goal within this research is to develop a reliable a priori interface method. The suggestion in [24] is followed to make use of Orthogonal Polynomial Series as a solution space for interface motion. Both Legendre as Fourier series are tested as an interface reduction basis in chapter 8.

It is found that OPS interface reduced results do converge towards a full interface solution. Even reduction sets limited to 4 DoF per direction of motion, has lead to resembling FRF compared to full order solutions, i.e. (anti-)resonance frequencies are estimated accurately and no major differences are observed in relevant magnitudes of FRF, confirmed by high FRAC values.

As accuracy tends to decrease over frequency, due to increasingly frequent mode shapes at interfaces (spatially), the effectiveness of OPS interface reduction is very dependent on the system properties and considered load cases, together confining the frequency range of interest. Also given the context of system properties in FEM, refinement of a mesh can drastically increase the number of DoF, which are, in case of superfluosness, effectively reduced due to set motion shapes and the corresponding amount of OPS shapes to accurately represent them. Also a disadvantageous mention is required towards similarity of natural boundary motion of substructures te be coupled. Generally, a flexible substructure tends to adapt to the modes of a stiffer substructure when coupled, which usually leads to simpler mode shapes. Substructures of similar stiffness on the other hand tend to interfere with each others mode shapes, leading to more complicated shapes to approximate. Concluding, with dependency of analysis context considered, efficiency of OPS reduction both from a qualitative as well as a quantitative perspective cannot be universally guaranteed. But provided the results from the test cases in both chapters 8 and 9, its potential on this matter is confirmed.

A number of error trends have been observed and explained. Starting with the most pronounced tendency in the error plots, error peaks arise near anti-resonance frequencies in a relative sense. This appearance originates from the fact that anti-resonance frequencies are very prone to miscoverage of modes and tend to shift significantly in these cases. Provided their small absolute value, and thus participation to the global motion, this error trend can be deemed irrelevant.

In some cases, relative errors in the quasi-static frequency range are high with respect to the tendencies of the higher frequency range. This phenomenon is related to Saint-Venant's principle, meaning that interfaces close to loads do not dispose of sufficient space to redistribute stresses, leading to disfigured displacement fields at the interfaces. Hence a larger set of OPS is required for their covering an adequate solution space. Corresponding errors induced can be significant and may require control with the use of expanding a reduction set.

When dealing with transfer paths involving multiple interfaces, errors are amplified along the paths. Though interface reduction bases may provide adequate solution space for true responses, the arriving loads already include errors due to inaccuracies in system properties elsewhere. To sustain sufficient accuracy, one may choose to selectively expand interface reduction bases which are particularly relevant for the transfer paths considered.

Effects of viscoelasticity

Substructures can be coupled with the use of viscoelastic elements. The orders of magnitude of connecting stiffness and damping do impact the interaction between substructures and thus alter mode shapes at connected boundaries. These alterations do affect results, but not to unacceptable extents. Frequency dependence of connecting stiffness and damping do not influence results due to the fact that FRF, and thus the stiffness- and damping matrices, are evaluated per frequency sample, remaining indifferent to any material properties at other frequencies.

It is shown that viscoelastic properties within a substructure do not necessarily require customized reduction techniques involving complex vibration modes. Given a sufficiently lightly varying dynamic modulus of viscoelastic materials, the undamped vibration modes (conform static stiffness) can provide an adequate solution space. Considering the fact that complex vibrations modes come in conjugate pairs, spanning a frequency range with a modal basis will require double the amount of DoF as for undamped modes, inclusion of complex modes is undesirable in terms of reducing the computational load. Also resemblance of complex modes to undamped modes of a component can be influenced with strategic substructure definition, up to isolating viscoelastic parts into one substructure, achieving proportional properties for which undamped modes remain a valid choice. The potential of using complex modes beyond aforementioned conditions is not yet clear, due to their results being affected by approximation errors of the complex modes used in the test case.

This has led to additional reviewing on the approximative method in [31], resulting in supplementing conditions for its validity besides limiting damping. Though the original method does barely provide a better modal basis, its enhancement in [41] yet offers worthwhile improvement, making it a considerable option for some viscoelastic models, especially the efficiency of the developed truncation algorithm in section 5.3.3.

Practical value of CMS

The test case presented in chapter 9 proves CMS to be a feasible option given the use of OPS interface reduction, featuring a decrease of DoF up to over 98% of the full model. Results with respect to interfaces are comparable to results found in chapter 8, delivering qualitative and quantitative coverage of dynamic behaviour. At points of interest results are even more accurate due to a dominating role of lower frequency content along the filtering of the transfer paths, which is relatively accurately described by OPS. It should be noted though, that elimination of transfer paths by design can lead to higher frequency content gaining a larger contribution to the responses of interest, inducing larger errors as well.

A front-to-end analysis has been performed, using a characteristic load case, computing a time domain response at points of interest. The error contained in the relevant values (here being maximum velocity) is of such an insignificant magnitude that regarding the amount of DoF reduced (over 50.000 to less than 700), CMS can now be considered a valuable technique for efficient vibrational studies in buildings.

10.2 Recommendations

With the conclusions of this research, a step has been made towards wider application of CMS. Though CMS has already been proven to be an attractive option for vibrational analysis in buildings, further improvements may still be rewarding. Also, extending the scope of this research will create valuable opportunities for wider application. The following recommendations are made:

- 1 At the moment, the required polynomial order to be included in an OPS reduction basis to achieve a desired accuracy is not determined a priori. An estimator should be developed to accomplish practical comfort. These estimations can be based on coverage of solution space for the interface displacement modes (see section 4.2) or the local behaviour in free vibrations modes (see section 3.1.1) of a substructure, up to an appropriate frequency range. Depending on the substructures to be coupled, the interface reduction set can be further truncated due to adaption (flexible structures submitting to stiffer structures).
- 2 It has already been observed that Fourier series do not converge towards the full solution as fast as Legendre series do, based on the straight interface. Given the continuous nature of Fourier series, it is presumed that Fourier series may be a more viable option for unbound interfaces, e.g. circular hollow sections or wind turbine blades. It is suggested to perform tests on this.
- 3 With respect to curvilinear interface shapes in particular building designs or other applications, it might be convenient to project OPS functions onto the interfaces, rather than using the interface shape as a function axis. The most suitable option, or perhaps an hybrid method should be investigated.
- 4 As mentioned before, OPS interface reduction can also be used to describe planar interfaces. As suggested function series are described one-dimensional, combinations need to be made over the two axes involved as demonstrated in [26]. Due to the sharply increasing number of possible combinations with the use of higher order polynomials, reduction will tend to lose efficiency. A priori elimination of less relevant combinations could prevent this.
- 5 Though this research emphasizes that the use of complex vibration modes in an interior reduction basis will be inefficient under certain (realistic) circumstances, further tests should be performed beyond these conditions in order to determine the true relevance of its use. This can be done using viscoelastic properties that enable exact computation of complex modes, but also by seeking approximative methods that enable arbitrary viscoelastic models to be analysed accurately. The latter may be sought in a state-space approach.
- 6 Expanding modelling possibilities for structural joints within the reduced domain, it might be necessary to take into account non-linear damping such as dry friction in bolted and plated structural joints. A suitable non-linear CMS technique does yet exist [45, 46], and its efficiency in the context of structural joints in buildings should be explored.

Although this research is performed in the practical context of building design, the development of OPS interface reduction does offer opportunities for other applications as well. This may involve similar analyses such as coupling of space- or aircraft, or other vehicle parts. But also other advantages may be exploited, such as isolating non-linear structural parts, which may prove to be lucrative in e.g. non-linear time history analysis used for Groninger seismic safety assessment.

Bibliography

- [1] M. Hermens, M. Visscher, and J. Kraus, “Ultra Light Weight Solutions for Sustainable Urban Densification,” in *Proceedings of the CTBUH*, 2014, pp. 542–549.
- [2] R. V. M. Cobelens, “Building light and comfortable,” Master thesis, Delft University of Technology, 2018.
- [3] D. de Klerk, D. J. Rixen, and S. N. Voormeeren, “General Framework for Dynamic Substructuring: History, Review and Classification of Techniques,” *AIAA Journal*, vol. 46, no. 5, pp. 1169–1181, 2008. [Online]. Available: <http://arc.aiaa.org/doi/10.2514/1.33274>
- [4] S. N. Voormeeren, “Dynamic Substructuring Methodologies for Integrated Dynamic Analysis of Wind Turbines door,” Doctoral thesis, 2012.
- [5] P. van der Valk, “Model Reduction & Interface Modeling in Dynamic Substructuring -Application to a multi-megawatt wind turbine-,” MSc thesis, 2010.
- [6] M. V. van der Seijs, “Experimental Dynamic Substructuring,” Doctoral thesis, 2016.
- [7] A. Maressa, D. Mundo, S. Donders, and W. Desmet, “A wave-based substructuring approach for concept modeling of vehicle joints,” *Computers and Structures*, vol. 89, pp. 2369–2376, 2011. [Online]. Available: <http://dx.doi.org/10.1016/j.compstruc.2011.06.011>
- [8] S. Donders, R. Hadjit, K. Cuppens, and M. Brughmans, “A Wave-Based Substructuring Approach for Faster Vehicle Assembly Predictions,” in *International Conference on Noise and Vibration Engineering, Leuven, September 18-20, 2006 : ISMA 2006*, 2006.
- [9] S. Donders, R. Hadjit, M. Brughmans, L. Hermans, and W. Desmet, “A wave-based sub-structuring approach for fast vehicle body optimisation,” *International Journal of Vehicle Design*, vol. 43, p. 100, 2007.
- [10] W. C. Hurty, “Component Modes,” *AIAA Journal*, vol. 3, no. 4, pp. 678–685, 1965.
- [11] R. Craig and M. Bampton, “Coupling of Substructures for Dynamic Analyses,” *AIAA Journal*, vol. 6, no. 7, pp. 1313–1319, 1968.
- [12] D. J. Rixen, “A dual Craig-Bampton method for dynamic substructuring,” *Journal of Computational and Applied Mathematics*, vol. 168, pp. 383–391, 2004.
- [13] D. M. Tran, “Component mode synthesis methods using partial interface modes: Application to tuned and mistuned structures with cyclic symmetry,” *Computers and Structures*, vol. 87, no. 17-18, pp. 1141–1153, 2009.
- [14] P. Koutsovasilis and M. Beitelschmidt, “Model order reduction of finite element models: Improved component mode synthesis,” *Mathematical and Computer Modelling of Dynamical Systems*, vol. 16, no. 1, pp. 57–73, 2010.

- [15] R. J. Kuether and K. L. Troyer, “Substructuring of Viscoelastic Subcomponents with Interface Reduction,” in *Dynamics of Coupled Structures - Proceedings of the 35th IMAC, A Conference and Exposition on Structural Dynamics 2017*, M. S. Allen, R. L. Mayes, and D. J. Rixen, Eds., vol. 4. Springer, 2017, pp. 17–27. [Online]. Available: <http://link.springer.com/10.1007/978-3-319-54930-9>
- [16] Z. Ding, L. Li, and Y. Hu, “A free interface component mode synthesis method for viscoelastically damped systems,” *Journal of Sound and Vibration*, vol. 365, pp. 199–215, 2016.
- [17] J. A. Morgan, C. Pierre, and G. M. Hulbert, “Baseband methods of component mode synthesis for non-proportionally damped systems,” *Mechanical Systems and Signal Processing*, vol. 17, no. 3, pp. 589–598, 2003.
- [18] P. Apiwattanalungarn, S. W. Shaw, and C. Pierre, “Component mode synthesis using nonlinear normal modes,” in *Nonlinear Dynamics - Proceedings of DETC’03 ASME 2003 Design Engineering Technical Conferences and Computers and Information in Engineering Conference*. Chicago: Springer, 2003, pp. 17–46.
- [19] L. Wu and P. Tiso, “Nonlinear model order reduction for flexible multibody dynamics: a modal derivatives approach,” *Multibody System Dynamics*, vol. 36, no. 4, pp. 405–425, 2015. [Online]. Available: <http://dx.doi.org/10.1007/s11044-015-9476-5>
- [20] O. Flodén, “Vibrations in Lightweight Structures; Efficiency and Reduction of Numerical Models,” Licentiate Dissertation, Lund University, 2014.
- [21] M. Breitfuss and H. J. Holl, “Shock & Vibration, Aircraft/Aerospace, Energy Harvesting, Acoustics & Optics, Volume 9,” in *Shock & Vibration, Aircraft/Aerospace and Energy Harvesting - 35th IMAC, A Conference and Exposition on Structural Dynamics*, J. M. Harvie and J. Baqersad, Eds., vol. 9, 2017, pp. 167–178. [Online]. Available: <http://link.springer.com/10.1007/978-3-319-54735-0>
- [22] S. Donders, B. Pluymers, P. Ragnarsson, R. Hadjit, and W. Desmet, “The wave-based substructuring approach for the efficient description of interface dynamics in substructuring,” *Journal of Sound and Vibration*, vol. 329, no. 8, pp. 1062–1080, 2010. [Online]. Available: <http://dx.doi.org/10.1016/j.jsv.2009.10.022>
- [23] W. Witteveen and K. Sherif, “POD based computation of Joint Interface Modes,” in *Linking Models and Experiments - Conference Proceedings of the Society for Experimental Mechanics Series 5*, T. Proulx, Ed., vol. 2. Springer, 2011, pp. 19–29. [Online]. Available: <http://link.springer.com/10.1007/978-1-4419-9305-2>
- [24] P. Holzwarth and P. Eberhard, “Interface reduction for CMS methods and alternative model order reduction,” *IFAC-PapersOnLine*, vol. 28, no. 1, pp. 254–259, 2015. [Online]. Available: <http://dx.doi.org/10.1016/j.ifacol.2015.05.005>
- [25] D. Krattiger, L. Wu, M. Zacharczuk, M. Buck, R. J. Kuether, M. S. Allen, P. Tiso, and M. R. W. Brake, “Interface reduction for Hurty / Craig-Bampton substructured models : Review and improvements,” *Mechanical Systems and Signal Processing*, vol. 114, pp. 579–603, 2019. [Online]. Available: <https://doi.org/10.1016/j.ymsp.2018.05.031>
- [26] L. Carassale and M. Maurici, “Interface Reduction in Craig Bampton Component Mode Synthesis by Orthogonal Polynomial Series,” *Journal of Engineering for Gas Turbines and Power*, vol. 140, no. 5, pp. 052 504–1 – 052 504–8, 2018. [Online]. Available: <http://gasturbinespower.asmedigitalcollection.asme.org/article.aspx?doi=10.1115/1.4038154>
- [27] S. S. Gómez and A. Metrikine, “Evaluation of the applicability of an energy method to calculate the damping in a lab-scale structure,” *Procedia Engineering*, vol. 199, pp. 459–464, 2017. [Online]. Available: <http://dx.doi.org/10.1016/j.proeng.2017.09.018>

- [28] S. Adhikari and B. Pascual, “Iterative Methods for Eigenvalues of Viscoelastic Systems,” *Journal of Vibration and Acoustics*, vol. 133, no. 2, pp. 021 002–1 – 021 002–7, 2011. [Online]. Available: <http://vibrationacoustics.asmedigitalcollection.asme.org/article.aspx?articleid=1471545>
- [29] S. Adhikari and N. Wagner, “Analysis of Asymmetric Nonviscously Damped Linear Dynamic Systems,” *Journal of Applied Mechanics*, vol. 70, no. 6, pp. 885–893, 2003. [Online]. Available: <http://appliedmechanics.asmedigitalcollection.asme.org/article.aspx?articleid=1415021>
- [30] R. Kuether, K. Troyer, and M. Brake, “Time Domain Model Reduction Reduction of Linear Viscoelastic Finite Element Models,” 2016. [Online]. Available: <http://linkinghub.elsevier.com/retrieve/pii/S0022460X98918727>
- [31] J. Woodhouse, “Linear damping models for structural vibration,” *Journal of Sound and Vibration*, vol. 215, no. 3, pp. 547–569, 1998.
- [32] D. J. Rixen, “Substructuring and Dual Methods in Structural Analysis,” Doctoral thesis, 1997.
- [33] M. van der Seijs, D. van den Bosch, D. Rixen, and D. de Klerk, “an Improved Methodology for the Virtual Point Transformation of Measured Frequency Response Functions in Dynamic Substructuring,” *Proceedings of the 4th International Conference on Computational Methods in Structural Dynamics and Earthquake Engineering (COMPDYN 2013)*, pp. 4334–4347, 2014. [Online]. Available: <http://www.eccomasproceedia.org/conferences/thematic-conferences/compdyn-2013/4816>
- [34] E. A. Pasma, M. V. van der Seijs, S. W. B. Klaassen, and M. W. van der Kooij, “Frequency Based Substructuring with the Virtual Point Transformation , Flexible Interface Modes and a Transmission Simulator,” *Dynamics of Coupled Structures*, vol. 4, pp. 205–213, 2018.
- [35] J. W. S. Rayleigh, *The theory of sound*. Macmillan, 1896, vol. 1/2.
- [36] M. Lázaro, “Nonviscous modes of nonproportionally damped viscoelastic systems,” *Journal of Applied Mechanics*, vol. 82, p. 121011, 2015.
- [37] T. E. Booth, “Power Iteration Method for Several Largest Eigenvalues and Eigenfunctions,” 2004.
- [38] S. Adhikari, “Damping models for structural vibration,” *Engineering Department*, 2000. [Online]. Available: <http://engweb.swan.ac.uk/~adhikaris/fulltext/other/ftphd.pdf>
- [39] R. J. Allemang, “The modal assurance criterion - Twenty years of use and abuse,” *Sound and Vibration*, vol. 37, no. 8, pp. 14–21, 2003. [Online]. Available: <http://www.scopus.com/inward/record.url?eid=2-s2.0-0141958862&partnerID=tZOTx3y1>
- [40] R. Askarbekov, D. Herak, and C. Mizera, “Mechanical behavior of rubber samples under relaxation,” *Engineering for Rural Development*, pp. 745–749, 2016.
- [41] S. Adhikari, “Calculation of derivative of complex modes using classical normal modes,” *Computers and Structures*, vol. 77, pp. 625–633, 2000.
- [42] P. H. Waarts, “SBR 539.05 Trillingen van vloeren door lopen; Richtlijn voor het voorspellen, meten en beoordelen,” 2005.
- [43] F. Galanti, “Achtergronddocument voor vloertrillingen,” Delft, 2008.
- [44] R. A. Toupin, “Saint Venant’s Principle,” *Archive for Rational Mechanics and Analysis*, vol. 18, no. 2, pp. 83–96, 1965.
- [45] C. Joannin, B. Chouvion, F. Thouverez, J.-P. Ousty, and M. Mbaye, “A nonlinear component mode synthesis method for the computation of steady-state vibrations in non-conservative systems: Application to mistuned cyclic structures with dry friction nonlinearities,” *Mechanical Systems and Signal Processing*, vol. 83, pp. 75–92, 2016.

- [46] C. Joannin, F. Thouverez, and B. Chouvion, “Reduced-order modelling using nonlinear modes and triple nonlinear modal synthesis,” *Computers and Structures*, vol. 203, pp. 18–33, 2018.